POLITECNICO DI TORINO

Facoltà di Ingegneria

Corso di Dottorato in
Ingegneria Elettronica e delle Comunicazioni

Tesi di Dottorato

Worst-Case Analysis of Electrical and Electronic Equipment via Affine Arithmetic

L'Aritmetica Affine nell'Analisi del Caso Peggiore di
Sistemi Elettrici ed Elettronici

Tongyu Ding

Coordinatore
Prof. I. Montrosset

Tutore
Prof. F. Canavero
Prof. I. Stievano

XXVII ciclo

Acknowledgments

I would like to thank several people who have contributed in different ways towards the work accomplished in this thesis.

First and foremost, I would like to express my utmost gratitude to my supervisor, Prof. Flavio Canavero, for his encouragement, guidance, and support. His wide knowledge and insightful comments have made my candidature a truly enriching experience.

I would also like to express my sincerest appreciation to my co-supervisor, Prof. Igor Stievano. His patience, motivation, and guidance have benefitted me immensely. This thesis work would not have been possible without his insightful thoughts.

I would thank Dr. Paolo Manfredi and Riccardo Trinchero, for their time and efforts devoted in my research work, for the valuable suggestions and critical questions during this thesis.

I also acknowledge my colleagues, Marchisio, Petrini, Fontana, Figura, Ubolli and Elisabetta, for their help and accompany in the last three years. Thanks to Dr. Sun Wen and Dr. Jiang Yanchao, for their generous help and encouragement.

Finally, thanks to my best friends, Tiegang, Cunfa and Yuekun who have always been so supportive. And many thanks to my family, to my parents for their constant support in my life. To them I dedicate this thesis.

Contents

Abstract

In the design and fabrication process of electronic equipment, there are many unkown parameters which significantly affect the product performance. Some uncertainties are due to manufacturing process fluctuations, while others due to the environment such as operating temperature, voltage, and various ambient aging stressors. It is desirable to consider these uncertainties to ensure product performance, improve yield, and reduce design cost. Since direct electromagnetic compatibility measurements impact on both cost and time-to-market, there has been a growing demand for the availability of tools enabling the simulation of electrical and electronic equipment with the inclusion of the effects of system uncertainties.

In this framework, the assessment of device response is no longer regarded as deterministic but as a random process. It is traditionally analyzed using the Monte Carlo or other sampling-based methods. The drawback of the above methods is large number of required samples to converge, which are time-consuming for practical applications. As an alternative, the inherent worst-case approaches such as interval analysis directly provide an estimation of the true bounds of the responses. However, such approaches might provide unnecessarily strict margins, which are very unlikely to occur. A recent technique, affine arithmetic, advances the interval based methods by means of handling correlated intervals. However, it still leads to over-conservatism due to the inability of considering probability information.

The objective of this thesis is to improve the accuracy of the affine arithmetic and broaden its application in frequency-domain analysis. We first extend the existing literature results to the efficient time-domain analysis of lumped circuits considering the uncertainties. Then we provide an extension of the basic affine arithmetic to the frequency-domain simulation of circuits. Classical tools for circuit analysis are used within a modified affine framework accounting for complex algebra and uncertainty interval partitioning for the accurate and efficient computation of the worst case bounds of the responses of both lumped and distributed circuits. The performance of the proposed approach is investigated through extensive simulations in several case studies. The simulation results are compared with the Monte Carlo method in terms of both simulation time and accuracy.

List of Acronyms

AA   affine arithmetic

EMC   electromagnetic compatibility

EMI   electromagnetic interference

IA   interval arithmetic

LTI   linear time-invariant

MC   Monte Carlo

MNA   modified nodal analysis

MTL   multiconductor transmission line

PC   polynomial chaos

PCB   printed circuit board

p.u.l.   per-unit-length

TEM   transverse electromagnetic

UIP   uncertainty interval partitioning

Chapter 1

Introduction

Nowadays, there has been a growing demand for the availability of tools enabling the simulation of electrical and electronic equipment with the inclusion of the effects of system uncertainties. Circuit and device parameters suffer from various kinds of temporal and structural variations, including temperature, process conditions and aging, thus unavoidably leading to a spread of the system behavior that needs to be fully characterized [1]–[3].

1.1 Motivation

With the fast development of information and telecommunication technologies, there has been a growing demand for large-scale integration, miniaturization and stringent design specifications, all of which making the impact of variability inside circuits and their interconnections increasingly relevant and hard to control [4]–[6]. Designers have to take into account all the uncertainties within complex electronic circuits, to set realistic design margins and correctly assess behavior of system responses [7]–[10].

Different sources of variability are usually present. The major cause of randomness is the tolerance that unavoidably characterizes the fabrication process. This means that different produced devices, which are designed to be nominally the same, differ from one to another as a result of the manufacturing process. Other sources include the unpredictability of the operating conditions (e.g., chip temperature or loading), inherent variations, and external uncertainties, such as electromagnetic radiation, and various long-term aging stressors.

Process variation

Process variation has always been a key concern for manufacturability, process control, and circuit design. There are generally three kinds of process variations [11]–[13]:

- *device variations*, which mainly regard the parameters of the metal-oxide-semiconductor (MOS) transistors inside drivers and receivers and are due to patterning, deposition and etching in the fabrication process. The main MOS parameters affected by variability are the effective gate length, the threshold voltage, the oxide thickness and the parasitic resistance of the drain/source;

- *interconnect variations* , which are due to the photo litographic, etching and dielectric deposition processes and affect the metal thickness (t), inter-layer dielectric thickness (h), and linewidth (w), respectively, as shown in Fig. 1.1. Variation in the interconnect would directly result in a change in its electrical properties, including the resistance (R), capacitance (C), and inductance (L), which finally affect the performance of the circuit;

- *dynamic variations*, which include fluctuations of the supply voltage (due to the loading condition of the power supply grid) and temperature (related to the location of the blocks with the highest activity).
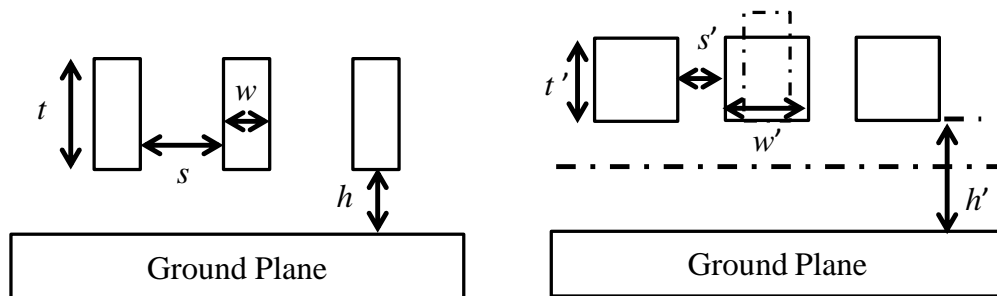

Figure 1.1.   Cross-section of parallel interconnect lines above a ground plane. Left panel: the ideal case. Right panel: different types of variation that can exist in the interconnect [12].

It is of great significance to well understand process variations, in order to avoid unnecessarily large design margins. A key issue is to understand how much variation exists in a given design and what its impact is on circuit performance. There have been extensive works on this kind of research, such as, the analysis of parameter variation in scaled technologies beyond 90 nm and their impact on circuit and microarchitecture [14], and investigation of the impact of process variations on future interconnect solutions based on carbon nanotube bundles [15]–[17].

Aging Effects

Besides the aforementioned process and inherent variations, electronic equipment and systems as well as cables, joints and interconnects suffer from deterioration and degradation due to a considerable body of external aging stressors, such as thermal aging (temperature ranges, heat dissipation), mechanical aging (pressure, abrasion, and bend due to inspection and maintenance), chemical aging (humidity level due to moisture, pollution etc.), and electrical aging (high voltage, EMI etc.) [18], [19]. Sometimes, aging effects result in irreversible deleterious change to the serviceability of electronic systems and thus potential dangers, as were reported the accidents in aircrafts due to aging-caused failure of wiring systems [20]–[23]. More commonly, long-term aging impact on the electrical properties of devices and their interconnects, thus leading to variation of system behavior.

Take cables and wiring insulation aging as an example. Since the early *20*-th century, polymers have been gaining more and more attention as cable insulations due to their excellent properties such as low electrical conductivities, high dielectric strength, and flexibility in shapes and

sizes [24]. The large quantity of research work is exponentially growing on polymer aging and degradation analysis, such as impact on polyimide under constant thermal stresses [25]; degradation of poly(ethene-co-tetrafluoroethene) [26] and polyolefin in high-voltage cables [27].

Lebey and Diaham, et al. studied thermal effects on polyimide dielectric properties [28], [29], and they found the evolution of loss factor and conductivity of the insulation during 200 hours' aging. As we know, even a small aging variation of local parameters may lead to disastrous invertible effects on the system. Li et al. [30] explored the effect of thermal degradation at extreme temperatures (up to 475°C in air) on dielectric permittivity of polyimide. This extreme-temperature test lasts only five hours, and relative permittivity variation is obvious: increased from 3.2 to 4.2.

Another key issue of property variation is chemical aging due to water or solution [31], [32]. Eoin et al. used resonator method to calculate the relative permittivity of polyimide flexible printed circuit board (PCB) materials before and after 48 hours aging in 85% relative humidity (RH) level [33]. Radu et al. [34] studied influence of water treeing on cross-linked polyethylene (XLPE) samples applied in high-voltage systems: they measured the capacitance and water tree lengths in the material, and then deduced a law for the evolution of time-dependent permittivity inside the tree degraded areas. Fig. 1.2 exhibits the relative permittivity variation of XLPE after 200 hours aging in Radu's experiment [34].
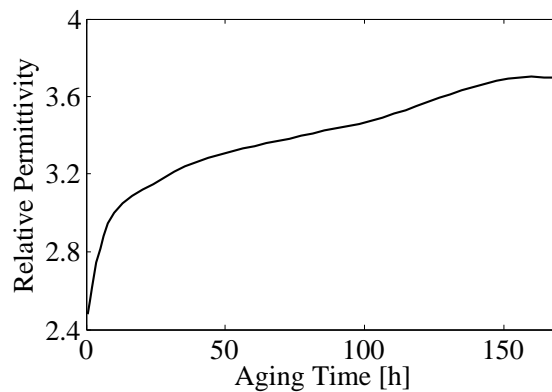
Figure 1.2.   Aging effects on electric parameters of wire insulation.

1.2 Goal of the Thesis

In this chapter, we have provided an overview of variability in electronic circuits and systems, which can adversely impact circuit performance, causing functional and parametric yield loss. Although variation has a detrimental impact, a lack of understanding about its resulting effects can be even worse. In [35]–[37], analytical probabilistic models were developed for evaluation of coupling between transmission lines with inclusion of parametric variations, but are limited to low-frequency approximations as well as basic and simplified structures.

In this regard, worst-case tolerance analysis has been playing an important role. Given tolerance ranges of circuit elements, the goal of worst-case tolerance analysis is to compute the

practical response ranges [38]. The idea has been widely used for estimation of circuit performance bounds [39]–[44]. The basic approach to performing a worst-case analysis on a schematic for an electronic board is to breakdown the circuit into simple functional blocks and perform a worst-case analysis on each block. It is imperative to develop the worst-case variations of all critical parameters for all parts utilized in the circuit, in order to arrive at a worst-case MAX and a worst-case MIN for each part parameters [45].

Since direct measurements impact on both cost and time-to-market, the EMC community has recently faced a growing demand for numerical simulation tools enabling efficient, uncertainty-aware, worst-case analysis of electronic systems [46]. These tools are generally based on three mathematical techniques, i.e., the extreme value analysis, root-sum-square and Monte Carlo analysis [45].

In [47], the authors used full-band Monte Carlo simulations to analyze the worst-case conditions for high voltage transistors, while in [48], a method based on polynomial chaos theory was proposed to estimate the possible worst case of a measurement, due to the propagation of parametric uncertainty of a low-pass filter and a loop impedance. The extreme-value-analysis methods are also well studied, such as, the application of the genetic algorithms [49]–[51], interval analysis [52]–[54], and affine arithmetic [50] for worst-case circuit analysis. However, these approaches faced different drawbacks, e.g., the MC method usually produces underestimated results, while the extreme-value-based approaches do not benefit from the advantage of having a statistical knowledge, as they might provide unnecessarily strict margins, which are very unlikely to occur.

This thesis focuses in particular on the worst case analysis of lumped and distributed electrical and electronic circuits with the inclusion of effects of parameter uncertainties. The objective of the thesis is to develop a new simulation framework based on the affine arithmetic, which is able to provide inherent worst-case estimation of response ranges in a broad application fields.

1.3   State of the Art

This section briefly summarizes the key features of the state-of-the-art techniques for the computation of the worst-case system response. For the sake of illustration, Fig. 1.3 shows the upper bound response of an electronic equipment affected by parametric uncertainties (solid black line) and the approximation achieved using Monte Carlo, polynomial chaos, interval analysis and affine arithmetic (dashed lines). This figure provides a visualization of the intrinsic differences among the methods and highlights the separation of the above techniques into the class of worst case (as IA and AA) and probabilistic techniques (MC and PC in this comparison). The former methods always provide conservative bounds and approximate the reference worst case response from the top. Also, the AA method is in general more precise and less conservative than IA and it is therefore a good candidate to be effectively used in real application examples. On the contrary, the later probabilistic methods approximate the worst case from the bottom, with an increasing accuracy that is a function of the number of samples. As the number of simulations increases, the evaluated bound can get infinitely close to the true value. Thus the probabilistic techniques achieve high precision with the sacrifice of efficiency.
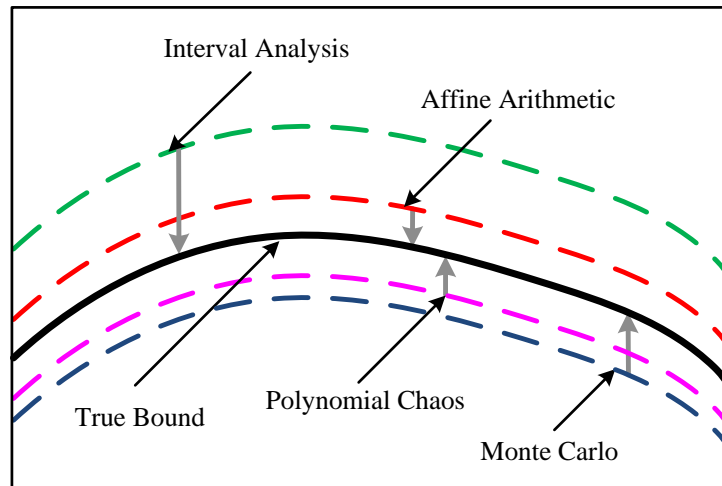
Figure 1.3. Approximations of the true worst-case by means of a number of different state-of-the-art techniques: solid black line is assumed as true value of the upper bound of a generic circuit or system response, while the dashed lines are worst-case approximations obtained with MC, PC, IA and AA (see text for details).

Monte Carlo

Monte Carlo has been used as a faithful technique which carries out repeated deterministic simulations to span the domain of parameters variation and to collect useful statistical information. The knowledge of MC is of paramount importance for designers, as it allows for an uncertainty-aware analysis, like the estimation and the possible improvement of the production yield (i.e., the percentage of devices that will meet design specifications) [55]–[57].

A MC-based statistical modeling of signal propagation on transmission lines has been addressed in [58]–[61]. In [13], the authors presented the effects of process variations on the multi-level signaling system for on-chip interconnects. A standard scheme is chosen and implemented into HSPICE, a common and well-known software for circuit simulation. Monte Carlo simulations are then performed by sampling several random system parameters, which are subject to process variations, according to their distribution (typically, Gaussian).

Extended applications of Monte Carlo include the design optimization in the presence of random variations (see, e.g., [58]). In this case, given some random parameters and design constraints, an additional optimization phase seeks to find the nominal design values to be used in order to obtain the highest possible yield. This allows to develop process-tolerant, right-the-first-time designs, which are extremely important in the commercial production workflow, as they imply money and time savings.

On the other hand, for large and complex systems, a single simulation is time-consuming (e.g., hours or days). Since MC approach requires a large number of samples to get accurate results, it may become unfeasible. Research works have been carried out to seek for alternative methods for a fast evaluation of statistical information even for large and complex systems. Therefore, in this case, MC simulations are used as a baseline to validate the proposed approach [62]–[65].

Polynomial chaos

Recently, a set of alternative techniques aimed at overcoming the above limitation and that are based on both probabilistic and worst-case methods have been proposed. An effective example belonging to the former class is based on the so-called polynomial chaos theory, where random variables are expanded in terms of orthogonal polynomials (see Fig. 1.4).
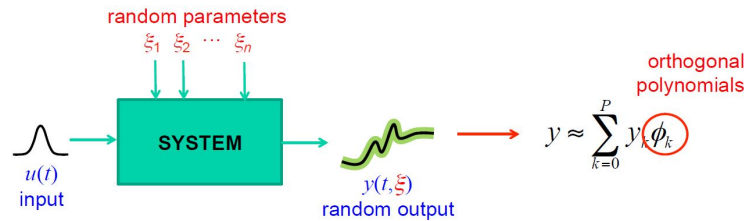

Figure 1.4.   Concept of polynoimal chaos theory.

The polynomial chaos approach [66]–[68], that has been proved to be far more efficient than MC, was successfully applied to the statistical simulation of circuits and systems in many domains of physics and engineering, such as mechanics [69]–[71], control theory [72], bioelectromagnetics [73], [74], and computational electromagnetics [75], [76], with the inclusion of the simulation of electrical networks and electronic circuits affected by random variability [77].

In [78], the authors addressed the stochastic simulation of a complex interconnect excited by a random external field by means of an expansion of the random electrical variables onto a basis of orthogonal polynomials. As a result, the stochastic problem is rewritten as a linear combination of deterministic solutions, analogous to Fourier decomposition. Briefly speaking, this technique has been based on the expansion of stochastic processes in terms of suitable orthogonal polynomials [79] and is therefore effective as long as the random parameters can be well approximated in terms of polynomial functions.

However, both MC and PC based techniques share the main drawback that the worst case bounds arising from bounded uncertainties can be computed via post-processing and a large number of simulations only.

Interval Analysis

As has been illustrated in Fig. 1.3, the probabilistic methods such as MC and PC approximate the worst case from the bottom, with an increasing accuracy that is a function of the number of samples. On the contrary, the inherent worst-case approaches directly provides an estimation of the true bounds of the responses (e.g., see. [41]–[43]).

In 1960s, Ramon E. Moore first proposed the interval analysis method [80] which defines the random interval value by a pair of real values, representing the lower bound and the upper bound, respectively, hence allowing to collect the worst combination of all the uncertain parameters. It has been used to solve many fundamental problems, such as linear equations [82], [83], non-linear equations [84], [85], global optimization [86], [87] and various practical problems such as switching level simulation [88] and RC timing analysis [89] in VLSI design.

Femia et al. used IA for time-domain circuit simulation in [52]. The partitioning of the parameter uncertainty ranges is used to increase the accuracy of IA-based computations. Although IA method is able to provide inherent worst-case analysis, it assumes all random parameters to be independent, without taking into account the correlation among them, thus in general leading to relatively large overestimation. Since MC-based techniques always provide an underestimation of the true range, whereas IA always yields to an overestimation, they can be regarded as complementary tools and are applied jointly [52].

Affine Arithmetic

In order to improve the results from IA, the affine arithmetic was proposed by Stolfi and Comba in the early 1990s [90], [91]. This technique accounts for the correlation among variables and yields much tighter and more reasonable upper and lower bounds. It has also been applied to global optimization [92], [93], computer graphics [94]–[96], computer vision [97], analog circuit sizing [98], and circuit tolerance analysis [46], [50].

Femia and Spagnuolo used AA to improve circuit tolerance analysis results obtained from IA [50]. Ma et al. used AA for interconnect and effective capacitance modeling [99], [100], and estimated the delay distribution for the variational circuit. Affine technique has also been used to efficiently perform range analysis for power flow problems [101], [102] and even thermal rating assessment of overhead lines [103]. However, so far, the application of AA in worst-case circuit analysis has been mainly concentrated in time-domain simulation of simplified lumped circuits only.

1.4   Organization of the Text

This text aims at providing a self-contained discussion about the application of the AA technique to the worst case analysis of lumped circuits and interconnect structures. The thesis is organized as follows. In Chapter 2, the mathematical background of interval and affine arithmetic are introduced, focusing on the extension of AA to complex algebra and matrix operations. Chapter 3 introduces the partitioning technique, which is effective in improving the accuracy of AA simulation results, along with some illustrative examples involving the time-domain simulation of lumped circuits. In Chapter 4, the proposed approach is applied to the solution of lumped circuits in frequency-domain. In Chapter 5, the simulation procedure for deterministic transmission lines is presented, and a tutorial description of application of AA to transmission line structures is provided. Finally, Chapter 6 provides more realistic application examples on both distributed interconnects and switching power converters.

Chapter 2

The Affine Arithmetic

This chapter starts from the definition of interval values, as well as the basic arithmetic of interval scalars and matrices, then continues to the fundamental theory of the so-called affine arithmetic, representing also the basic rules for affine computations of both real and complex scalars and matrices.

2.1 Interval Arithmetic

2.1.1 Basics of Interval Arithmetic

Interval arithmetic, or interval analysis (IA) is a range-based model for numerical computation. In this model, an interval value $\bar{x}$ is defined by a pair of real values a and b, which represent the lower bound and the upper bound of the value, respectively:

$$\bar{x} = [a, b] \tag{2.1}$$

meaning that the true value of x should satisfy $a \leq x \leq b$, namely, $[a, b] = \{x \mid a \leq x \leq b\}$.

For convenience, we define a few interval terms as follows. Provided an interval value $\bar{x}$ is given as in (2.1), then the width of the interval $\bar{x}$ is defined and denoted by:

$$w(\bar{x}) = b - a \tag{2.2}$$

The absolute value of $\bar{x}$, denoted $|\bar{x}|$, is the maximum of the absolute values of its endpoints:

$$|\bar{x}| = max(|a|, |b|) \tag{2.3}$$

Note that $|x| \leq |\bar{x}|$ for every $x \in \bar{x}$.

The midpoint of $\bar{x}$ is defined as:

$$m(\bar{x}) = \frac{a + b}{2} \tag{2.4}$$

All these interval terms are illustrated by Fig. 2.1, and these definitions apply also to matrices. Provided $\bar{\mathbf{X}}$ is an interval matrix with each element being a real interval value: $\bar{x}_{ij} = [a_{ij}, b_{ij}]$.

9

$$\bar{\mathbf{X}} = \begin{bmatrix} \bar{x}_{11} & \bar{x}_{12} \\ \bar{x}_{21} & \bar{x}_{22} \end{bmatrix} \tag{2.5}$$

The midpoint of the interval matrix $\bar{\mathbf{X}}$ is:

$$m(\bar{\mathbf{X}}) = \begin{bmatrix} m(\bar{x}_{11}) & m(\bar{x}_{12}) \\ m(\bar{x}_{21}) & m(\bar{x}_{22}) \end{bmatrix} \tag{2.6}$$
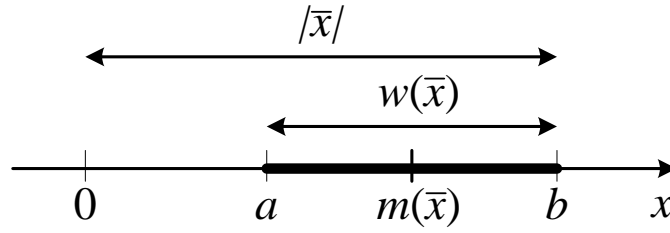

Figure 2.1. Illustration of interval arithmetic terms defined for a real interval value.

2.1.2 Interval Operations

Basic Operations for Real Scalars

It is obvious from the interval definition of (2.1) that a real interval is in fact a closed connected set of reals, and computing with intervals is actually computing with sets. For instance, when we add two intervals, the resulting interval is a set consisting of the sums of all pairs of numbers, one from each of the two initial sets [80].

Let $\bar{x} = [a, b]$ and $\bar{y} = [c, d]$ be real compact intervals, the corresponding arithmetic operations for intervals $\bar{x}$ and $\bar{y}$ are:

$$\begin{aligned} [a, b] + [c, d] &= [a + c, b + d] \\ [a, b] - [c, d] &= [a - d, b - c] \\ [a, b] \times [c, d] &= [min(ac, ad, bc, bd), max(ac, ad, bc, bd)] \end{aligned} \tag{2.7}$$

Note that for division, the interval arithmetic is valid only when $[c, d]$ does not contain zero.

$$[a, b]^n = \begin{cases} [1, 1] & if \ n = 0 \\ [0, max(a^n, b^n)] & if \ n = even, 0 \in [a, b] \\ [min(a^n, b^n), max(a^n, b^n)] & otherwise \end{cases} \tag{2.8}$$

In this model, even some elementary algebra has to be modified, for example, the distributive law should be replaced by the so-called subdistributivity [81]:

$$[a, b] \times ([c, d] \pm [e, f]) \subset [a, b] \times [c, d] \pm [a, b] \times [e, f] \tag{2.9}$$

Intersection and Union

Intersection plays an important role in IA. Provided two intervals containing a result of interest, the intersection would be narrower and also contain the result. Given $\bar{x} = [a, b]$ and $\bar{y} = [c, d]$, the intersection of $\bar{x}$ and $\bar{y}$ is empty if $b < c$ or $d < a$. Otherwise:

$$\bar{x} \cap \bar{y} = \{\bar{z} | z \in \bar{x} \ and \ z \in \bar{y}\}$$
$$= [max(a, c), min(b, d)] \tag{2.10}$$

Similarly, the union of $\bar{x}$ and $\bar{y}$ is also an interval:

$$\bar{x} \cup \bar{y} = \{\bar{z} | z \in \bar{x} \ or \ z \in \bar{y}\}$$
$$= [min(a, c), max(b, d)] \tag{2.11}$$

This law would be useful in the next chapters for computing the union of several sub-intervals, when the proposed method is combined with the so-called partitioning technique.

Operations for Interval Matrices

An interval matrix means that the elements of the matrix are interval numbers, as has been explained in (2.5), and the midpoint of an interval matrix is obtained from (2.6). The width and norm of the interval matrix $\bar{\mathbf{X}}$ is defined as follows:

Matrix norm:

$$\|\bar{\mathbf{X}}\| = \max_{i} \sum_{j} |\bar{x}_{ij}| \tag{2.12}$$

Matrix width:

$$w(\bar{\mathbf{X}}) = \max_{i,j} w(\bar{x}_{ij}) \tag{2.13}$$

The arithmetic for interval matrices is based on the arithmetic for interval numbers, for instance, $\bar{\mathbf{X}}$ and $\bar{\mathbf{Y}}$ are two interval matrices with all entries being interval numbers. The addition and subtraction of the two matrices are addition and subtraction of each element:

$$\bar{\mathbf{X}} \pm \bar{\mathbf{Y}} = \left[\begin{array}{cc} \bar{x}_{11} \pm \bar{y}_{11} & \bar{x}_{12} \pm \bar{y}_{12} \\ \bar{x}_{21} \pm \bar{y}_{21} & \bar{x}_{22} \pm \bar{y}_{22} \end{array} \right] \tag{2.14}$$

While the product of two interval matrices is:

$$\bar{\mathbf{Z}} = \bar{\mathbf{X}} \cdot \bar{\mathbf{Y}} \tag{2.15}$$

where each element $\bar{z}_{ij}$ is obtained by means of the interval arithmetic on elements of $\bar{\mathbf{X}}$ and $\bar{\mathbf{Y}}$:

$$\bar{z}_{ij} = \sum_{k} \bar{x}_{ik} \cdot \bar{y}_{kj}$$

The recommended simulation tool for interval matrices operations is INTLAB, which is based on numerical linear algebra, and proves to make support for matrices operations [80].

In summary, interval analysis is a powerful technique of bounding solutions under uncertainty, it finds solution set which rigorously contains the true solution. However, success of IA is very dependent on the width of the intervals.

2.1.3 Limitations

The main weakness of IA is over-conservatism, or over-estimation: when evaluating expressions in IA, the resulting interval may be disappointingly large.

The main cause of the wide interval is that interval arithmetic does not take into account the correlations among input variables, namely, all inputs are forced to be independent, not related with each other. However, this is impossible, in case that there exist any mathematical constraints among the quantities, the result interval imputed by IA may be much wider than the true range.

For example, given two interval values $\bar{x}$ and $\bar{y}$ both lying between $[-1, 1]$, compute $(\bar{x}+\bar{y})$, we can only obtain $[-2, 2]$. However, if the two values have some relationship, for instance $x = -y$, it is obvious that $(\bar{x} + \bar{y})$ should be 0. In this case, the bounds $[-2, 2]$ is apparently too large. This probelm affects all interval operations, and in a long IA computation, it may lead to error explosion.

Error explosion occurs when there is a long complicated computation chain. The overall relative accuracy of the chain tends to be the product of the relative accuracies of each single step [90]. Therefore, as the computation continues along the chain, the overall error would increase step by step, until at last reach an exponentially explosion. Various techniques have been used to suppress the error explosion, one method is to reduce the number of correlated variables, thus reducing the scale of the systems. Femia et al. resorted to partitioning of tolerance intervals (PTI) to reduce the meaningless error [52]. However, if the number of uncertains continuously grow, the power of these remedies can be so limited, and at the same time becomes inefficient in terms of the computation time. For large-scale systems, error explosion is a major hindercap for the application of interval arithemtic.

2.2 Affine Arithmetic

2.2.1 Basics of Affine Arithmetic

An Alternative Expression of Interval Values

It has been well stated in Section 2.1 that an interval value is defined by a pair of real values, which represent the lower and upper endpoint of this value, respectively. Denote this type of representation in (2.1) as the "interval form", which contains only information of the lower and upper bounds. Then we defined a few more interval terms such as the width, midpoint and absolute of an interval value, as is illustrated in Fig. 2.1. With these definitions, an interval value can be expressed in an alternative way: the "midpoint and radius" representation. Assume $\bar{x} = [a, b]$ is a real interval number bounded by a and b, then $m(\bar{x})$ and $w(\bar{x})$ represent the midpoint and width of this value, and can be obtained from (2.2) and (2.4) , respectively.

An interval value can be expressed as:

$$\bar{x} = m(\bar{x}) + \left[-\frac{1}{2}w(\bar{x}), \frac{1}{2}w(\bar{x}) \right]$$

$$= m(\bar{x}) + \frac{1}{2}w(\bar{x})\,[-1, 1] \tag{2.16}$$

Denote $x_0 = m(\bar{x})$ as the central value, $x_1 = \frac{1}{2}w(\bar{x})$ as the radius, then:

$$\bar{x} = x_0 + x_1[-1, 1]$$

Obviously, $x_0 + x_1 = b$ is the initial upper bound of the interval, and $x_0 - x_1 = a$ gives the initial lower bound.

Affine Arithmetic

It has been stated that interval arithmetic can successfully bound the solutions under uncertainty, but it may provide a much too wide bounds because of its conservative nature: the arithmetic of only two endpoints is too conservative that it may include some area that the true value will never reach.

In order to overcome the over-conservatism (or over-estimation) problem highlighted above, a different interpretation of intervals has been proposed by Stolfi et al. in the 1990s – affine arithmetic [90]. The new method is based on the second interval form of (2.16), and aims at reducing the over-estimation in conventional IA method, so it assigns a new symbol to each quantity, in this case, if two or more quantities share the same uncertainty, they are automatically correlated with each other by the same symbol.

That is, to replace the interval $[-1, 1]$ in the IA expression of (2.16) with a new symbol ϵ_1 whose value lies in the interval $[-1, 1]$. Denote the new expression as "affine form", and denote the new interval number as $\tilde{x}$:

$$\tilde{x} = x_0 + x_1\epsilon_1 \tag{2.17}$$

where x_0 is the nominal or central value of the affine form value, and the coefficient x_1 represents the radius of the interval. They have the same physical meaning with those of IA terms. ϵ_1 is symbolic real variable (called noise symbol) whose value is unknown but assumed to lie in the interval $[-1, 1]$. It stands for an independent component of the total uncertainty. Moreover, the correlation among quantities is established by assigning them with the same noise symbol. Consider the previous example in IA model. x and y are two interval values both lying between $[-1, 1]$, and have the relationship that $x = -y$. With IA method, we have calculated $(\bar{x} + \bar{y}) = [-2, 2]$. This result does not take into account the correlation between x and y, thus caused severe over-estimation.

However, with the proposed AA method, the interval number x can be represented in the affine form of (2.17): $\tilde{x} = 0 + \epsilon_1$, which is still bounded by -1 and 1, and since $y = -x$, it is assigned with the same symbol ϵ_1: $\tilde{y} = 0 - \epsilon_1$. Then we are able to obtain: $\tilde{x} + \tilde{y} = (0 + \epsilon_1) + (0 - \epsilon_1) = 0$.

This is exactly the true value. It is stimulating that over-estimation is eliminated with the effort of affine improvement.

In real circumstances such as noise simulation, there may exist a large number of variations affecting the original parameter simultaneously. The general affine form of a quantity with the inclusion of various uncertainties is expressed as the first-degree polynomial:

$$\tilde{x} = x_0 + x_1\epsilon_1 + x_2\epsilon_2 + \cdots + x_n\epsilon_n$$
$$= x_0 + \sum_{i=1}^{n} x_i\epsilon_i \tag{2.18}$$

where x_0 is still the central value, and each ϵ_i stands for an independent component of uncertainty, with x_i the magnitude of that component. So we can easily get the upper and lower bounds of $\tilde{x}$ from (2.18) that: upper bound is $x_0 + \sum_i |x_i|$ and lower bound is $x_0 - \sum_i |x_i|$. It is worth noticing that in both IA and AA models, the upper and lower bound of any interval result are always symmetric to the central value, this would be useful in the latter discussion of accuracy.

Affine Operations

Same as IA, the affine form operations also generate outputs that rigorously contain the true solution. Suppose the input forms are:

$$\tilde{x} = x_0 + x_1\epsilon_1 + x_2\epsilon_2 + \cdots + x_n\epsilon_n$$
$$\tilde{y} = y_0 + y_1\epsilon_1 + y_2\epsilon_2 + \cdots + y_n\epsilon_n$$

The operations between $\tilde{x}$ and $\tilde{y}$ can be classified into two categories: the affine operations and Non-affine operations. The first class is direct symbolic operations on the input affine forms, leading also to affine form results (first-degree polynomials). For instance, the affine operations of $\tilde{x} \pm \tilde{y}$, $\alpha\tilde{x}$, and $\tilde{x} \pm \delta$ for any $\alpha, \delta \in \mathbb{R}$ are expressed as:

$$\tilde{x} \pm \tilde{y} = (x_0 \pm y_0) + (x_1 \pm y_1)\epsilon_1 + \cdots + (x_n \pm y_n)\epsilon_n$$
$$\alpha\tilde{x} = (\alpha x_0) + (\alpha x_1)\epsilon_1 + \cdots + (\alpha x_n)\epsilon_n$$
$$\tilde{x} \pm \delta = (x_0 \pm \delta) + x_1\epsilon_1 + \cdots + x_n\epsilon_n \tag{2.19}$$

In the next part, we will introduce the second category of "non-affine" operations, which is not straightforward affine operations and would generate quadratic terms.

2.2.2 Non-Affine Operations

Non-affine operations, such as reciprocal, multiplication, division, square root and so on, would produce nonlinear terms into the result, which "damages" the affine form of first-degree polynomials. What we need to do is to convert the new equation into the linear affine form, for example, in the operation of affine multiplication, one method is to replace the quadratic term by adding a new noise symbol.

Multiplication

Consier the same input quantities $\tilde{x} = x_0 + \sum_{i=1}^{n} x_i \epsilon_i$ and $\tilde{y} = y_0 + \sum_{i=1}^{n} y_i \epsilon_i$, both affected by n terms of noise symbols $\epsilon_{1,2,...,n}$. The product of $\tilde{x}$ and $\tilde{y}$ gives:

$$\tilde{z} = \tilde{x} \cdot \tilde{y} \tag{2.20}$$

$$= \left(x_0 + \sum_{i=1}^{n} x_i \epsilon_i \right) \cdot \left(y_0 + \sum_{i=1}^{n} y_i \epsilon_i \right)$$

$$= x_0 y_0 + \sum_{i=1}^{n} (x_0 y_i + y_0 x_i) \epsilon_i + \left(\sum_{i=1}^{n} x_i \epsilon_i \right) \left(\sum_{i=1}^{n} y_i \epsilon_i \right)$$

Apparently, a number of quadratic terms are generated in this process, the solution is to add a new noise symbol ζ to replace all the quadratic terms, and this ζ is completely independent with all the existing ones. Let:

$$\left(\sum_{i=1}^{n} x_i \epsilon_i \right) \left(\sum_{i=1}^{n} y_i \epsilon_i \right) \approx \left(\sum_{i=1}^{n} |x_i| \sum_{i=1}^{n} |y_i| \right) \zeta = R(\tilde{x}\tilde{y})\zeta \tag{2.21}$$

It is clear that, all quadratic terms are substituted with one new noise symbol, and the coefficient of this new symbol $R(\tilde{x}\tilde{y})$ is sum of absolute of all quadratic coefficients. This approximation can successfully capture the bounds of the initial value, but it would also introduce inaccuracy from two aspects: firstly, the independency of this new symbol skips over its correlation with the others, thus resulting in the same over-estimation effect as in IA method. Moreover, the computation of the new coefficient $R(\tilde{x}\tilde{y})$ always gives the maximum absolute magnitude of ζ, which is also over-conservative.

Reform the expression in (2.21), the resulting interval value $\tilde{z}$ can be expressed as:

$$\tilde{z} = z_0 + \sum_{i=1}^{n} z_i \epsilon_i + R(\tilde{x}\tilde{y})\zeta \tag{2.22}$$

where $z_0 = x_0 y_0$ is the resulting nominal value, $z_i = x_0 y_i + y_0 x_i$ represents coefficients of existing noise symbols $\epsilon_{1,2,...,n}$, and $R(\tilde{x}\tilde{y})\zeta$ is the new symbol term.

We have stated in the above section that in affine models, the upper and lower bound of any interval are always symmetric to the central value, and this also applies to any interval result such as $\tilde{z}$, which is product of two affine form interval numbers. However, the obtained nominal z_0 does not ensure to be the midpoint of the result interval $\tilde{z}$. If it is closer to the true upper bound, than the distance from z_0 to the lower endpoint is taken as the radius (or magnitude), thus leading to over-estimation at the former one, as is illustrated in the first case of Fig. 2.2, and vice versa.

Another problem of affine multiplication is that a new symbol is introduced in this process. In case that we need to do a large number of multiplications, the number of noise symbols would grow continuously. This would inevitably results in cumbersome computations in a complicated system and leads to inefficientcy in terms of computation time.
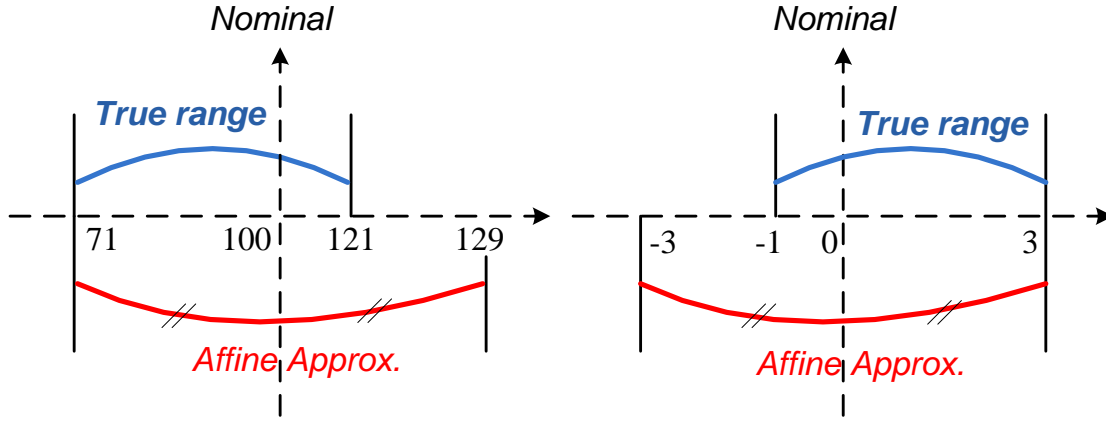
Figure 2.2.   Overestimation of affine form multiplication.

Take an example of affine form multiplication.

Example 1

Suppose $\tilde{x} = 10 + 2\epsilon_1 + 1\epsilon_2$ and $\tilde{y} = 10 - 2\epsilon_1 + 1\epsilon_3$ are two interval values both affected by two uncertainties, and they are related with each other by the shared symbol ϵ_1. Evalute the expression:

$$\begin{aligned}
\tilde{z} &= \tilde{x}\tilde{y} \\
&= (10 + 2\epsilon_1 + 1\epsilon_2)(10 - 2\epsilon_1 + 1\epsilon_3) \\
&= 100 + 10\epsilon_2 + 10\epsilon_3 + (2\epsilon_1 + \epsilon_2)(-2\epsilon_1 + \epsilon_3)
\end{aligned} \tag{2.23}$$

According to (2.21), the quadratic term is replaced by adding a new symbol ϵ_4, and the resulting interval becomes $\tilde{z} = 100 + 10\epsilon_2 + 10\epsilon_3 + 9\epsilon_4$. Notice that the nomial value of $\tilde{z}$ is 100 and the corresponding upper and lower bounds are $\bar{z} = [100 - 29, 100 + 29] = [71, 129]$.

However, a more precise analysis reveals that the true range of the quadratic term is actually $[-9, 1]$ [90], thus the true bound of $\bar{z}$ should be $[71, 121]$. Therefore, the relative accuracy of the affine approximation is:

$$(121 - 71)/(129 - 71) = 0.86$$

This corresponds to the first over-estimation case in Fig. 2.2, where the obtained nominal is closer to the true upper bound, and therefore introduces error on this side.

Nevertheless, Stolfi et al. [90] proved that AA approximation ensures a much better estimation of the results than conventional IA approaches, especially when carrying out a long chain of computations.

Example 2

Consider the joint range of affine form intervals $\tilde{x} = 10 + 2\epsilon_1 + \epsilon_2 - \epsilon_4$ and $\tilde{y} = 20 - 3\epsilon_1 + \epsilon_3 + 4\epsilon_4$. Obviously, x lies in the interval $\bar{x} = [6, 14]$, and y lies in the interval $\bar{y} = [12, 28]$. Then the joint range of $\bar{x} \times \bar{y}$ obtained by means of IA is shown as the gray rectangular area in Fig. 2.3,

which assumes the two input intervals as completely independent. On the other hand, the affine operations takes into account the presence of common noise symbols ϵ_1 and ϵ_4 in the two inputs, and therefore provides a much tighter joint range of the polygon shape in Fig. 2.3.
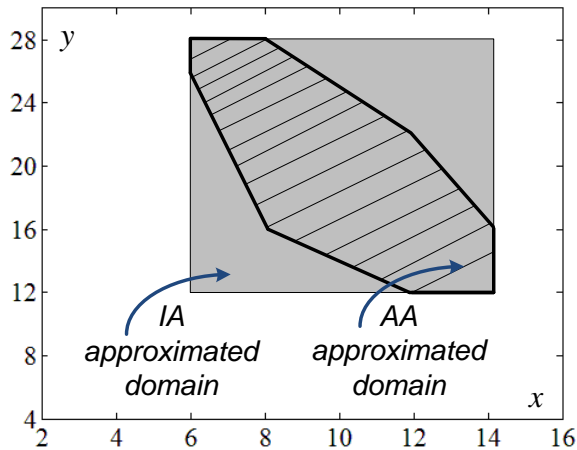

Figure 2.3.   Comparison of IA and AA approximated ranges.

Division

Division of two affine forms $\tilde{x}$ and $\tilde{y}$ is a bit more difficult than product of them. It can be reformed as product of one interval with the reciprocal of the other:

$$\tilde{z} = \frac{\tilde{x}}{\tilde{y}} = \tilde{x} \cdot \left(\frac{1}{\tilde{y}}\right) \tag{2.24}$$

This work contains actually two steps: first compute reciprocal of $\tilde{y}$, then compute the multiplication with the same routines above.

To invert an affine form which is in fact non-affine operation, we must select a good affine approximation for the function $1/\tilde{y}$:

$$\frac{1}{\tilde{y}} = \frac{1}{y_0 + y_1\epsilon_1 + \cdots + y_n\epsilon_n}$$

In order to convert the above equation into the standard affine form, we resort to the "minimax affine approximation" theory in [90].

Theorem 1 *Let f be a bounded and twice differentiable function defined on some interval $I = [a, b]$, whose second derivative f'' does not change sign inside I. Let $f^a(x) = \alpha x + \zeta \pm \delta$ be its minimax affine approximation in I. Then:*

- *The coefficient α is simply $(f(b) - f(a))/(b - a)$, the slope of the line $r(x)$ that interpolates the points $(a, f(a))$ and $(b, f(b))$.*

- *The maximum absolute error occur twice at the endpoints a and b of the range, and once at every interior point u of I where $f'(u) = \alpha$.*

- *The independent term ζ is such that $\alpha u + \zeta = (f(u) + r(u))/2$, and the maximum absolute error is $\delta = |f(u) - r(u)|/2$.*

According to Theorem 1, the function can be approximated as first-degree polynomials, and the problem reduces to finding the fitting coefficients α, δ and ζ for the best approximation:

$$\frac{1}{\tilde{y}} \approx \alpha \left(y_0 + y_1 \epsilon_1 + \cdots + y_n \epsilon_n \right) + \zeta \pm \delta \tag{2.25}$$

Theorem 1 already gives an algorithm for finding the optimum coefficients α, δ and ζ, which is the so-called algorithm of "chebyshev approximation", another algorithm is the "min-range approximation", which is similar but is easier in coding for computing interval reciprocal. The "minrange" approximation is implemented as follows (see Fig. 2.4): suppose $\tilde{y}$ is bounded by the interval $[c, d]$. The tangent at the higher endpoint $(d, 1/d)$ and its parallel line which goes through the other endpoint $(c, 1/c)$ composed the joint range of $\tilde{y}$ and $1/\tilde{y} = \alpha \tilde{y} + \zeta \pm \delta$ (the gray area in Fig. 2.4). The dashed line represents the midpoint of $1/\tilde{y}$ as $\tilde{y}$ ranges in the interval.

Notice that the interval cannot include 0, assume it is entirely positive $(c > 0)$, then the slope of the lines is the derivative of $1/\tilde{y}$ at $y = d$, namely, $\alpha = -1/d^2$. The values of the dashed line at the endpoint c and d are expressed as:

$$\frac{1}{c} - \delta = -\frac{1}{d^2}c + \zeta$$
$$\frac{1}{d} + \delta = -\frac{1}{d} + \zeta$$

Thus:

$$\zeta = \frac{1}{c} + \frac{c + 2d}{d^2}$$
$$\delta = \frac{1}{c} + \frac{c - 2d}{d^2} \tag{2.26}$$

Assign a new noise symbol ϵ_{n+1} to the new magnitude parameter δ, the resulting function becomes:

$$\frac{1}{\tilde{y}} \approx \tilde{w} = w_0 + w_1 \epsilon_1 + \cdots + w_n \epsilon_n + w_{n+1} \epsilon_{n+1} \tag{2.27}$$

where $w_0 = \alpha y_0 + \zeta$ is the new nominal value, $w_i = \alpha y_i$ corresponds to the coefficients of initial noise symbols, and $w_{n+1} \epsilon_{n+1}$ is the new generated symbol term with $w_{n+1} = \delta$ being the new symbol coefficient computed from (2.26)
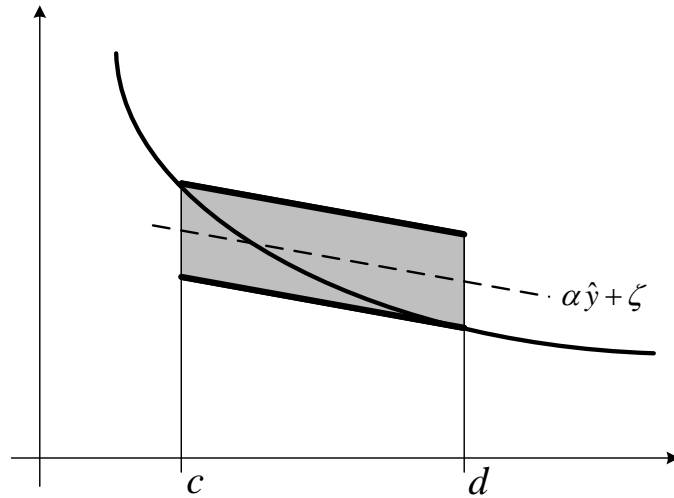
Figure 2.4.   Minrange approximation for reciprocal.

At last we obtain, $\tilde{z} = \tilde{x} \cdot \left(\dfrac{1}{\tilde{y}} \right) = \tilde{x} \cdot \tilde{w}$ which is the form of affine multiplication. Hence, division is composed by two steps of "non-affine" operations, reciprocal and product, each generating one more additional independent noise symbol. The total number of noise symbols is increased by two.

The case of negative argument range $(d < 0)$ is similar. Notice that the program for affine division must take into account both situations.

Exponential

Use the "chebyshev approximation theory" in Theorem 1 to compute the exponential of an interval $\tilde{y}$ bounded by the range $[c, d]$. That is, to approximate the function $\exp(\tilde{y})$ with linear affine combinations:

$$
\begin{aligned}
\exp\left(\tilde{y}\right) &= \exp\left(y_0 + y_1\epsilon_1 + \cdots + y_n\epsilon_n\right) \\
&\approx \alpha\left(y_0 + y_1\epsilon_1 + \cdots + y_n\epsilon_n\right) + \zeta \pm \delta
\end{aligned}
\tag{2.28}
$$

According to "Theorem 1", first find the line that interpolates the two endpoints (c, e^c) and (d, e^d), denoted as *line #1*, then there exists only one point u inside $[c, d]$, where the tangent at this point has the same slope with *line #1*. These two lines encircle the area of all possibilities of $\exp(\tilde{y})$, which is also the minimum approximation. See Fig. 2.5. The dashed line in the middle: $\alpha\tilde{y} + \zeta$ is parallel to *line #1*, thus the slope is:

$$
\alpha = \frac{e^d - e^c}{d - c}
$$

The dashed line is also the "best approximation line" of function $\exp(\tilde{y})$. The maximum error appears at the two endpoints and at the point u with opposite sign, and its magnitude is:

$$\delta = \frac{(e^c - \alpha c) - \alpha (1 - \ln \alpha)}{2}$$

Similarly, the magnitude of maximum error is assigned with a new noise symbol to include the "worst-case". The parameter ζ is:

$$\zeta = \frac{(e^c - \alpha c) + \alpha (1 - \ln \alpha)}{2}$$

At last, all parameters of the linear approximation are selected (all optimum), and the function is reformed as:

$$\exp(\tilde{y}) \approx \tilde{v} = v_0 + v_1 \epsilon_1 + \cdots + v_n \epsilon_n + v_{n+1} \epsilon_{n+1} \tag{2.29}$$

where $v_0 = \alpha y_0 + \zeta$ is the new nominal value, $v_i = \alpha y_i$ corresponds to the coefficients of initial noise symbols, and $v_{n+1} \epsilon_{n+1}$ is the new generated symbol term with $v_{n+1} = \delta$ representing the maximum error magnitude.

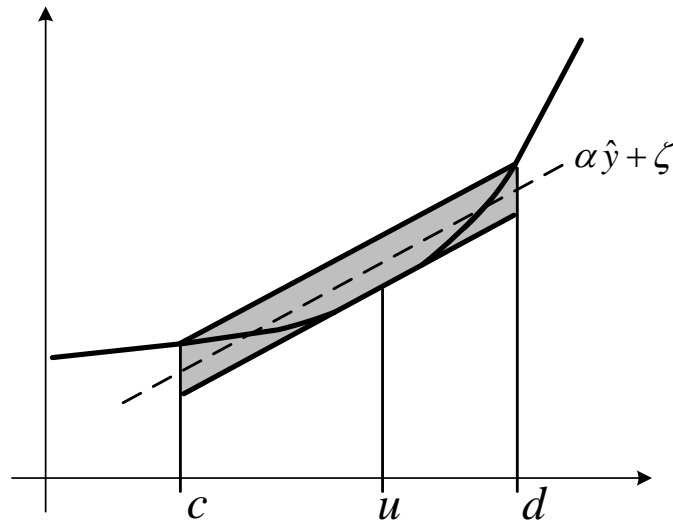Figure 2.5.   Chebyshev approximation for exponential.

Logarithm

Most of monotonic functions can be evaluated by means of the two approximation approaches above.

Use the "minrange" method to compute the logarithm of an interval $\tilde{y}$ bounded by the range $[c, d]$. Again, approximate the function as $\ln(\tilde{y}) \approx \alpha \tilde{y} + \zeta \pm \delta$, the approximation parameters are:

$$\alpha = \frac{1}{d} \qquad \delta = \frac{(\ln(d) - \alpha d) - (\ln(c) - \alpha c)}{2} \qquad \delta = \frac{(\ln(d) - \alpha d) + (\ln(c) - \alpha c)}{2}$$

It is notable that the affine arithmetic and approximation methods do not work on periodic functions such as sinusoidal. In certain situations, we need to combine IA and AA.

To summarize, affine operations such as addition, negation et al. directly produce the affine form, and introduce no extra error, while non-affine operations such as multiplication, division, exp. *et.al* generate nonlinear forms, and in order to convert it into the affine form, we approximate any nonlinear functions with linear combinations of inputs, which *(i)* is sure to include definitely the initial interval and gives the standard affine form, but *(ii)* generates new noise symbols, leading to system inefficiency, and *(iii)* skips over the correlation among the new symbols and the existing ones, leads to some over-estimation. On the other hand, both affine and non-affine operations make a great improvement in both accuracy and efficiency than IA method, and the defects of *(ii)* and *(iii)* can be hopefully reduced with combination of other numerical techniques.

2.2.3   Error-Spreading

It has been stated above that in non-affine arithmetic, additional noise symbols are generated in each single operation. In the condition that we need to do a large amount of multiplications, the number of random variables will grow continuously, which is inefficient in terms of computation time.

Rutenbar proposed in [99] to distribute the additional quadratic terms into the existing uncertainty variables. It states that:

$$\tilde{z} \approx z_0 + \sum_{i=1}^{n} z_i \left[1 + \frac{1}{\sum_{i=1}^{n} |z_i|} R(\tilde{x}\tilde{y}) \right] \epsilon_i \tag{2.30}$$

The new method proves to be a conservative approximation that always bounds the true range of $\tilde{z}$, while at the same time successfully avoids the generation of uncertainty symbols.

However, there is a lack of mathematical derivations from (2.22) to (2.30), thus cannot guarantee a best distribution.

In order to find a minimum-error way to distribute the quadratic terms into the existing uncertainty variables, Zou et al. proposed a method in [104], and found a best distribution factor to be $1/n$ (n being the number of symbols):

$$\tilde{z} \approx z_0 + \left(\sum_{i=1}^{n} z_i + \frac{1}{n} R(\tilde{x}\tilde{y}) \right) \epsilon_i \tag{2.31}$$

In this work, we use the method in (2.31) for most of the affine operations.

2.2.4   Extension to Complex Algebra

In this section, the arithmetic for affine model is extended to complex field. Since the application of this technique in frequency domain is relatively poorly documented compared with that in time

domain issues, it would be of great significance to develop corresponding algebra of the method in complex field [105] and apply it in frequency domain issues.

To extend the arithmetic to complex field, we resort to the basic rules of operations for real scalars above. Assume two complex form interval values:

$$
\begin{aligned}
\tilde{x} &= \tilde{x}_r + j\tilde{x}_i \\
\tilde{y} &= \tilde{y}_r + j\tilde{y}_i
\end{aligned}
\tag{2.32}
$$

where

$$
\begin{aligned}
\tilde{x}_r &= x_{r0} + \sum_{k=1}^{n} x_{rk}\epsilon_k \\
\tilde{x}_i &= x_{i0} + \sum_{k=1}^{n} x_{ik}\epsilon_k \\
\tilde{y}_r &= y_{r0} + \sum_{k=1}^{n} y_{rk}\epsilon_k \\
\tilde{y}_i &= y_{i0} + \sum_{k=1}^{n} y_{ik}\epsilon_k
\end{aligned}
$$

are real affine form interval values defined in (2.18). The sum and subtraction of $\tilde{x}$ and $\tilde{y}$ are straightforward and can be performed following the same routines of scalar real intervals as in (2.19):

$$
\tilde{x} \pm \tilde{y} = (\tilde{x}_r \pm \tilde{y}_r) + j(\tilde{x}_i \pm \tilde{y}_i).
\tag{2.33}
$$

The rules for multiplication and division are more complicated and can be represented as follows:

Complex form Multiplication

$$
\begin{aligned}
\tilde{z} &= \tilde{x} \cdot \tilde{y} \\
&= (\tilde{x}_r + j\tilde{x}_i) \cdot (\tilde{y}_r + j\tilde{y}_i) \\
&= (\tilde{x}_r\tilde{y}_r - \tilde{x}_i\tilde{y}_i) + j(\tilde{y}_r\tilde{x}_i + \tilde{y}_i\tilde{x}_r)
\end{aligned}
\tag{2.34}
$$

Complex Form Division

$$
\begin{aligned}
\tilde{z} &= \tilde{x}/\tilde{y} \\
&= \frac{\tilde{x}_r + j\tilde{x}_i}{\tilde{y}_r + j\tilde{y}_i} \cdot \frac{\tilde{y}_r - j\tilde{y}_i}{\tilde{y}_r - j\tilde{y}_i} \\
&= \frac{\tilde{x}_r\tilde{y}_r + \tilde{x}_i\tilde{y}_i}{\tilde{y}_r^2 + \tilde{y}_i^2} + j\frac{\tilde{x}_i\tilde{y}_r - \tilde{y}_i\tilde{x}_r}{\tilde{y}_r^2 + \tilde{y}_i^2}
\end{aligned}
\tag{2.35}
$$

The internal affine operations inside (2.34) and (2.35) follow the same routines of (2.22) or (2.31). The rules for addition, subtraction and multiplication above, also apply to matrix operations.

Compute the Bounds of Complex Interval

It has been previously stated that affine representation of interval numbers or matrices are based on the "midpoint and radius" expression in IA method, and it is transferrable between IA and AA forms. For instance, given a real interval number $\tilde{x}$ expressed in the affine form of (2.18), we have computed its upper and lower bounds by means of $x_0 \pm \sum_i |x_i| = [a, b]$.

For complex intervals, we also need from time to time to compute its absolute upper and lower bounds. For instance, compute the absolute bounds of the complex interval $\tilde{x} = \tilde{x}_r + j\tilde{x}_i$, where both real and imaginary parts of $\tilde{x}$ are real intervals of the standard form in (2.32), and can be represented as interval $\bar{x}_r = [a_r, b_r]$, $\bar{x}_i = [a_i, b_i]$.

According to the interval definition in (2.3), the absolute value of an interval is the maximum of the abosolute values of its endpoints, namely, $|\tilde{x}_r| = |\bar{x}_r| = max(|a_r|, |b_r|)$, and similarly, $|\tilde{x}_i| = |\bar{x}_i| = max(|a_i|, |b_i|)$. Thus, the maximum absolute value of $|\tilde{x}|$ is:

$$|\tilde{x}| = \sqrt{|\tilde{x}_r|^2 + |\tilde{x}_i|^2} \tag{2.36}$$

This is namely the upper bound of the complex interval.

Define $|\tilde{x}_r|_{min} = min(|a_r|, |b_r|)$, and $|\tilde{x}_i|_{min} = min(|a_i|, |b_i|)$ as the miminum of the absolute values of of endpoints of $\tilde{x}_r$ and $\tilde{x}_i$ respectively. Then we have:

$$|\tilde{x}|_{min} = \sqrt{|\tilde{x}_r|^2_{min} + |\tilde{x}_i|^2_{min}} \tag{2.37}$$

is the mininum aboslute value of $\tilde{x}$, namely, the absolute lower bound of the complex interval $\tilde{x}$.

However, in this case, we must exclude the situation of 0 being included. If 0 is inclued in the range of $\bar{x}_r$, then $|\tilde{x}|_{min} = |\tilde{x}_i|_{min}$, or 0 is included in the range of $\bar{x}_i$, then $|\tilde{x}|_{min} = |\tilde{x}_r|_{min}$, or if it is included in the range of both $\bar{x}_r$ and $\bar{x}_i$, then $|\tilde{x}|_{min} = 0$.

2.2.5   Affine Arithmetic for Matrices-Operations

In (2.5) and (2.6), we have introduced the definition of an interval matrix $\bar{\mathbf{X}}$ and its midpoint $m(\bar{\mathbf{X}})$. Let the width of $\bar{\mathbf{X}}$ be:

$$w(\bar{\mathbf{X}}) = \left[\begin{array}{cc} w(\bar{x}_{11}) & w(\bar{x}_{12}) \\ w(\bar{x}_{21}) & w(\bar{x}_{22}) \end{array} \right] \tag{2.38}$$

Then $\bar{\mathbf{X}}$ can be expressed by means of the "midpoint and radius" approach:

$$\begin{aligned} \bar{\mathbf{X}} &= m(\bar{\mathbf{X}}) + \left[-\frac{1}{2}w(\bar{\mathbf{X}}), \frac{1}{2}w(\bar{\mathbf{X}}) \right] \\ &= m(\bar{\mathbf{X}}) + \frac{1}{2}w(\bar{\mathbf{X}})\left[-1, 1\right] \\ &= \mathbf{X}_0 + \mathbf{X}_1\left[-1, 1\right] \end{aligned} \tag{2.39}$$

This is similar with the conversion between an interval number and its affine form. Assign a random symbol ϵ_1 to the variation, we can obtain the affine form of the interval matrix as:

$$\tilde{\mathbf{X}} = \mathbf{X}_0 + \mathbf{X}_1\epsilon_1 \tag{2.40}$$

Suppose $\tilde{\mathbf{X}}$ and $\tilde{\mathbf{Y}}$ are two affine form interval matrices:

$$\tilde{\mathbf{X}} = \mathbf{X}_0 + \mathbf{X}_1\epsilon_1 + \cdots + \mathbf{X}_n\epsilon_n$$
$$\tilde{\mathbf{Y}} = \mathbf{Y}_0 + \mathbf{Y}_1\epsilon_1 + \cdots + \mathbf{Y}_n\epsilon_n$$

Then the affine operations as well as multiplication between them are simple and similar with those for scalars in (2.19) and (2.22). For instance:

$$\tilde{\mathbf{X}} \pm \tilde{\mathbf{Y}} = (\mathbf{X}_0 \pm \mathbf{Y}_0) + (\mathbf{X}_1 \pm \mathbf{Y}_1)\epsilon_1 + \cdots + (\mathbf{X}_n \pm \mathbf{Y}_n)\epsilon_n$$
$$\tilde{\mathbf{X}} \times \tilde{\mathbf{Y}} = \mathbf{X}_0\mathbf{Y}_0 + \sum_{i=1}^{n}(\mathbf{X}_0\mathbf{Y}_i + \mathbf{Y}_0\mathbf{X}_i)\epsilon_i + \left(\sum_{i=1}^{n}|\mathbf{X}_i|\sum_{i=1}^{n}|\mathbf{Y}_i|\right)\epsilon_{n+1} \tag{2.41}$$

Unfortunately, it is impossible to apply the approaches of "chebyshev" and "minrange" approximations (that are used for computing reciprocal or exp. of affine form scalars) to the calculation of matrices. Since in lumped or distributed circuit analysis, it is always necessary to invert a matrix or to compute its exponential, we would combine the affine arithmetic with some numerical techniques in this section, to approximate the outer bounds of affine form matrix inversion and exponential.

Affine Form Matrix Inversion

Approximate outer bounds of inversion of matrix $\tilde{\mathbf{X}}$:

$$\tilde{\mathbf{X}}^{-1} = (\mathbf{X}_0 + \mathbf{X}_1\epsilon_1 + \cdots + \mathbf{X}_n\epsilon_n)^{-1} \tag{2.42}$$

This is nontrival because all variation matrices include a random symbol ϵ_i except the nominal $\mathbf{X}_0$, and we can certainly not compute $(\mathbf{X}_i\epsilon_i)^{-1}$ for $i = 1, 2, \ldots, n$, so this operation is something we must avoid.

Jack Sherman and Winifred J. Morrison proposed a mathematical formula to compute the inverse of the sum of two matrices, where one of them is invertible. The lemma states that

Sherman-Morrison formula *Suppose $\mathbf{A}$ is an invertible n times n square matrix and u, v are arbitrary vectors of dimension n. Suppose furthermore that $1 + v^T\mathbf{A}^{-1}u \neq 0$. Then:*

$$\left(\mathbf{A} + uv^T\right)^{-1} = \mathbf{A}^{-1} - \frac{\mathbf{A}^{-1}uv^T\mathbf{A}^{-1}}{1 + v^T\mathbf{A}^{-1}u}$$

Here, uv^T is the outer product of two vector u and v.

It is not difficult to find that the term $v^T \mathbf{A}^{-1} u$ corresponds to the trace of $\left(\mathbf{A}^{-1} u v^T \right)$. And the formula works only under the condition that $rank(uv^T) = 1$.

For simplicity, suppose the interval matrix $\tilde{\mathbf{X}}$ is affected by only one random symbol: $\tilde{\mathbf{X}} = \mathbf{X}_0 + \mathbf{X}_1 \epsilon_1$, and the noise coefficient matrix satisfies the condition that $rank(\mathbf{X}_1) = 1$, then we have:

$$(\mathbf{X}_0 + \mathbf{X}_1 \epsilon_1)^{-1} = \mathbf{X}_0^{-1} - \frac{1}{1+g} (\mathbf{X}_0^{-1} \mathbf{X}_1 \epsilon_1 \mathbf{X}_0^{-1})$$
$$= \mathbf{Y}_0 + \mathbf{Y}_1 \epsilon_1 \tag{2.43}$$

where $\mathbf{Y}_0 = \mathbf{X}_0^{-1}$ is the new nominal, $\mathbf{Y}_1 = -1/(1+g) \cdot (\mathbf{X}_0^{-1} \mathbf{X}_1 \mathbf{X}_0^{-1})$ is the new coefficient of ϵ_1, and $g = trace(\mathbf{X}_0^{-1} X_1)$, under the condition that $g \neq -1$.

Now let's consider the standard expression of $\tilde{\mathbf{X}}^{-1}$ in (2.42), where the m times m interval matrix $\tilde{\mathbf{X}}$ is affected by n random symbols simultaneously, and each coefficient matrix has rank over 1: $rank(\mathbf{X}_i) = m, (i = 1, 2, \ldots, n)$.

In order to satisfy the rank requirement in Sherman's forumla, first decompose each coefficient matrix $\mathbf{X}_i$ into m submatrices each having rank 1:

$$\tilde{\mathbf{X}}^{-1} = (\mathbf{X}_0 + \mathbf{X}_1 \epsilon_1 + \cdots + \mathbf{X}_n \epsilon_n)^{-1}$$
$$= \begin{bmatrix} \mathbf{X}_0 \\ + (\mathbf{X}_{11} + \mathbf{X}_{12} + \cdots + \mathbf{X}_{1m}) \epsilon_1 \\ + (\mathbf{X}_{21} + \mathbf{X}_{22} + \cdots + \mathbf{X}_{2m}) \epsilon_2 \\ + \cdots \\ + (\mathbf{X}_{n1} + \mathbf{X}_{n2} + \cdots + \mathbf{X}_{nm}) \epsilon_n \end{bmatrix}^{-1} \tag{2.44}$$

Then we can use (2.43) to solve (2.44) step by step. If:

$$(\mathbf{X}_0 + \mathbf{X}_{11} \epsilon_1)^{-1} = \mathbf{Y}_0 + \mathbf{Y}_{11} \epsilon_1 \tag{2.45}$$

Then:

$$(\mathbf{X}_0 + \mathbf{X}_{11} \epsilon_1 + \mathbf{X}_{12} \epsilon_1)^{-1}$$
$$= ((\mathbf{X}_0 + \mathbf{X}_{11} \epsilon_1) + \mathbf{X}_{12} \epsilon_1)^{-1}$$
$$= (\mathbf{X}_0 + \mathbf{X}_{11} \epsilon_1)^{-1} - \frac{1}{1+g} \left((\mathbf{X}_0 + \mathbf{X}_{11} \epsilon_1)^{-1} \mathbf{X}_{11} \epsilon_1 (\mathbf{X}_0 + \mathbf{X}_{11} \epsilon_1)^{-1} \right)$$
$$= (\mathbf{Y}_0 + \mathbf{Y}_{11} \epsilon_1) - \frac{1}{1+g} ((\mathbf{Y}_0 + \mathbf{Y}_{11} \epsilon_1) \mathbf{X}_{11} \epsilon_1 (\mathbf{Y}_0 + \mathbf{Y}_{11} \epsilon_1))$$
$$\approx \mathbf{Y}_0 + \mathbf{Y}_{12} \epsilon_1 \tag{2.46}$$

where $\mathbf{Y}_{12}$ is obtained with the "error spreading" method in (2.31):

$$\mathbf{Y}_{12} = \left(\mathbf{Y}_{11} - \frac{1}{1+g} \mathbf{Y}_0 \mathbf{X}_{11} \mathbf{Y}_0 \right) - \frac{1}{1+g} |\mathbf{Y}_{11}| \mathbf{X}_{11} |\mathbf{Y}_{11}|$$

The rest may be deduced by analogy. At the end of line ϵ_1 of (2.44), we have:

$$\left(\mathbf{X}_0 + \mathbf{X}_{11}\epsilon_1 + \cdots + \mathbf{X}_{1m}\epsilon_1 + \mathbf{X}_{21}\epsilon_2\right)^{-1}$$

$$= \left(\left(\mathbf{X}_0 + \mathbf{X}_{11}\epsilon_1 + \cdots + \mathbf{X}_{1m}\epsilon_1\right) + \mathbf{X}_{21}\epsilon_2\right)^{-1}$$

$$= \left(\mathbf{Y}_0 + \mathbf{Y}_{1m}\epsilon_1\right) - \frac{1}{1+g}\left(\left(\mathbf{Y}_0 + \mathbf{Y}_{1m}\epsilon_1\right)\mathbf{X}_{21}\epsilon_2\left(\mathbf{Y}_0 + \mathbf{Y}_{1m}\epsilon_1\right)\right)$$

$$\approx \mathbf{Y}_0 + \mathbf{Y}_1\epsilon_1 + \mathbf{Y}_{21}\epsilon_2 \tag{2.47}$$

where both coefficients $\mathbf{Y}_{1m}$ and $\mathbf{Y}_{21}$ are obtained by means of the method in (2.31):

$$\mathbf{Y}_1 = \mathbf{Y}_{1m} - \frac{1}{2(1+g)}|\mathbf{Y}_{1m}|\mathbf{X}_{21}|\mathbf{Y}_{1m}|$$

$$\mathbf{Y}_{21} = -\frac{1}{1+g}\left(\mathbf{Y}_0\mathbf{X}_{21}\mathbf{Y}_0 + \frac{1}{2}|\mathbf{Y}_{1m}|\mathbf{X}_{21}|\mathbf{Y}_{1m}|\right)$$

In this computation iteration, all inversion operations of variation matrices consisting of random symbol ϵ are avoided.

To summarize, suppose $\mathbf{X}_{jk}$ is the kth term in j^{th} line of the matrix in (2.44), and $\mathbf{Y}_{jk} = \mathbf{X}_{11}\epsilon_1 + \cdots + \mathbf{X}_{jk}\epsilon_j$ be sum of all the noise terms before $\mathbf{X}_{jk}$, then:

$$\mathbf{Y}_{j(k+1)}^{-1} = \mathbf{Y}_{jk}^{-1} - \frac{1}{1+g}\left(\mathbf{Y}_{jk}^{-1}\mathbf{X}_{jk}\mathbf{Y}_{jk}^{-1}\right) \tag{2.48}$$

At last, the inversion of $\tilde{\mathbf{X}}$ is numerically computed as:

$$\tilde{\mathbf{X}}^{-1} = \left(\mathbf{X}_0 + \mathbf{X}_1\epsilon_1 + \cdots + \mathbf{X}_n\epsilon_n\right)^{-1}$$

$$= \mathbf{Y}_0 + \mathbf{Y}_1\epsilon_1 + \cdots + \mathbf{Y}_n\epsilon_n \tag{2.49}$$

where $\mathbf{Y}_j = \mathbf{Y}_{jm}$ is obtained from (2.48)

An alternative method is to use the Talyor expansions, where inversion of sum of two matrices can be expressed as:

$$(\mathbf{A} + \mathbf{B})^{-1} \approx \mathbf{A}^{-1} - \mathbf{A}^{-1}\mathbf{B}\mathbf{A}^{-1} + \mathbf{A}^{-1}\mathbf{B}\mathbf{A}^{-1}\mathbf{B}\mathbf{A}^{-1} - \cdots \tag{2.50}$$

For the common case of $\tilde{\mathbf{X}}$ in (2.42), we have:

$$\left(\mathbf{X}_0 + \mathbf{X}_1\epsilon_1 + \cdots + \mathbf{X}_n\epsilon_n\right)^{-1}$$

$$\approx \mathbf{X}_0^{-1} - \mathbf{X}_0^{-1}\left(\mathbf{X}_1\epsilon_1 + \cdots + \mathbf{X}_n\epsilon_n\right)\mathbf{X}_0^{-1}$$

$$+ \mathbf{X}_0^{-1}\left(\mathbf{X}_1\epsilon_1 + \cdots + \mathbf{X}_n\epsilon_n\right)\mathbf{X}_0^{-1}\left(\mathbf{X}_1\epsilon_1 + \cdots + \mathbf{X}_n\epsilon_n\right)\mathbf{X}_0^{-1}$$

$$\approx \mathbf{X}_0^{-1} + \left(-\mathbf{X}_0^{-1}\mathbf{X}_1\mathbf{X}_0^{-1}\right)\epsilon_1 + \cdots + \left(-\mathbf{X}_0^{-1}\mathbf{X}_n\mathbf{X}_0^{-1}\right)\epsilon_n + \mathbf{X}_{n+1}\epsilon_{n+1} \tag{2.51}$$

The equation is expanded as only three terms of Taylor expansions, and all the high-order terms are approximated by one additional noise symbol ϵ_{n+1}, with coefficient:

$$\mathbf{X}_{n+1} = \mathbf{X}_0^{-1} \left(\sum_{i=1}^{n} |\mathbf{X}_i| \right) \mathbf{X}_0^{-1} \left(\sum_{i=1}^{n} |\mathbf{X}_i| \right) \mathbf{X}_0^{-1}$$

In summary, both the Sherman-Morrison iteration in (2.48) and the Taylor approximation in (2.51) provide accurate numerical solution to the inversion of affine-form interval matrix $\tilde{\mathbf{X}}$. The first approach works under the condition that the variation matrices have rank 1, if not, it is necessary to decompose them. However, this approach is accurate and more efficient for small-scale problems, thus has been used in the distributed interconnect models in Chapter 5, while the Taylor expansion method runs faster for large-scale problems, and therefore outperforms for the lumped-circuit analysis in Chapter 4 and Chapter 6.

Affine Form Matrix Exponential

To compute the exponential of an interval matrix, we can also resort to the Taylor expansion approximation, which sates that

Taylor series approximation:

$$\exp(\mathbf{A} + \mathbf{B}) \approx \mathbf{I}_n + (\mathbf{A} + \mathbf{B}) + \frac{1}{2}(\mathbf{A} + \mathbf{B})^2 + \sum_{i=3}^{\infty} \frac{1}{i!}(\mathbf{A} + \mathbf{B})^i \qquad (2.52)$$

where $\mathbf{I}_n$ is the identity matrix with the same dimension of $\mathbf{A}$ and $\mathbf{B}$.

This approach can successfully convert the $\exp$ of sum of matrices to easier operations of multiplication.

In our case of a standard affine-form interval matrix $\tilde{\mathbf{X}} = \mathbf{X}_0 + \mathbf{X}_1\epsilon_1 + \cdots + \mathbf{X}_n\epsilon_n$, the $\exp$ of $\tilde{\mathbf{X}}$ can be expressed as:

$$\exp(\tilde{\mathbf{X}}) = \exp\left(\mathbf{X}_0 + \mathbf{X}_1\epsilon_1 + \cdots + \mathbf{X}_n\epsilon_n\right) \approx \mathbf{I}_n + \left(\mathbf{X}_0 + \mathbf{X}_1\epsilon_1 + \cdots + \mathbf{X}_n\epsilon_n\right)$$
$$+ \frac{1}{2}\left(\mathbf{X}_0 + \mathbf{X}_1\epsilon_1 + \cdots + \mathbf{X}_n\epsilon_n\right)^2 + \frac{1}{6}\left(\mathbf{X}_0 + \mathbf{X}_1\epsilon_1 + \cdots + \mathbf{X}_n\epsilon_n\right)^3 + \cdots \qquad (2.53)$$

Use the "error spreading" method in (2.31) to the calculation of internal products inside (2.53). We first get:

$$\left(\mathbf{X}_0 + \mathbf{X}_1\epsilon_1 + \cdots + \mathbf{X}_n\epsilon_n\right)^i \approx \mathbf{X}_{i0} + \mathbf{X}_{i1}\epsilon_1 + \cdots + \mathbf{X}_{in}\epsilon_n \quad (i = 1, 2, \ldots) \qquad (2.54)$$

Then $\exp(\tilde{\mathbf{X}})$ can be approximated as the Affine form of:

$$\exp(\tilde{\mathbf{X}}) \approx \mathbf{Y}_0 + \mathbf{Y}_1\epsilon_1 + \mathbf{Y}_2\epsilon_2 + \cdots + \mathbf{Y}_n\epsilon_n \qquad (2.55)$$

where the nominal matrix:

$$\mathbf{Y}_0 = \mathbf{I}_n + \mathbf{X}_0 + \frac{1}{2}\mathbf{X}_0^2 + \sum_{i=3}^{\infty} \frac{1}{i!}\mathbf{X}_0^i$$

And the coefficient matrices:

$$\mathbf{Y}_j = \mathbf{X}_{1j} + \frac{1}{2}\mathbf{X}_{2j} + \sum_{i=3}^{\infty} \frac{1}{i!}\mathbf{X}_{ij} \quad (j = 1, 2, \ldots, n)$$

Shieh et al. presented a bilinear and inverse-bilinear approximation method for state-space model conversions of continuous-time and discrete-time structured uncertain linear systems [107]. When computing matrix exponential, it is approximated as

Bilinear Approximation:

$$\exp(\mathbf{X}) \approx \left(\mathbf{I}_n - \frac{1}{2}\mathbf{X}\right)^{-1}\left(\mathbf{I}_n + \frac{1}{2}\mathbf{X}\right) \tag{2.56}$$

Apply the above approximation to $\exp(\tilde{\mathbf{X}}) = \exp(\mathbf{X}_0 + \mathbf{X}_1\epsilon_1 + \cdots + \mathbf{X}_n\epsilon_n)$. For simplicity, denote $\Delta\mathbf{X} = \mathbf{X}_1\epsilon_1 + \cdots + \mathbf{X}_n\epsilon_n$, we have:

$$
\begin{aligned}
\tilde{\mathbf{Y}} &= \exp(\mathbf{X}_0 + \Delta\mathbf{X}) \\
&\approx \left[\mathbf{I}_n - \frac{1}{2}(\mathbf{X}_0 + \Delta\mathbf{X})\right]^{-1}\left[\mathbf{I}_n + \frac{1}{2}(\mathbf{X}_0 + \Delta\mathbf{X})\right] \\
&= \left[\mathbf{I}_n - \frac{1}{2}(\mathbf{X}_0 + \Delta\mathbf{X})\right]^{-1}\left[\left(\mathbf{I}_n + \frac{1}{2}\mathbf{X}_0\right) + \frac{1}{2}\Delta\mathbf{X}\right] \\
&\approx \left[\mathbf{I}_n - \frac{1}{2}(\mathbf{X}_0 + \Delta\mathbf{X})\right]^{-1}\left[\left(\mathbf{I}_n - \frac{1}{2}\mathbf{X}_0\right)e^{\mathbf{X}_0} + \frac{1}{2}\Delta\mathbf{X}\right] \\
&= \left[\mathbf{I}_n - \frac{1}{2}(\mathbf{X}_0 + \Delta\mathbf{X})\right]^{-1} \\
&\quad \cdot \left[\left(\mathbf{I}_n - \frac{1}{2}(\mathbf{X}_0 + \Delta\mathbf{X})\right)e^{\mathbf{X}_0} + \frac{1}{2}\Delta\mathbf{X}\left(e^{\mathbf{X}_0} + \mathbf{I}_n\right)\right] \\
&= e^{\mathbf{X}_0} + \frac{1}{2}\left[\mathbf{I}_n - \frac{1}{2}(\mathbf{X}_0 + \Delta\mathbf{X})\right]^{-1}\Delta\mathbf{X}(e^{\mathbf{X}_0} + \mathbf{I}_n) \\
&= \mathbf{Y}_0 + \Delta\mathbf{Y} \tag{2.57}
\end{aligned}
$$

where

$$\mathbf{Y}_0 = \exp(\mathbf{X}_0)$$

The variation matrices include operation of matrix inversion, which can be simplified with the above approaches:

$$
\begin{aligned}
\Delta\mathbf{Y} &= \frac{1}{2}\left[\mathbf{I}_n - \frac{1}{2}(\mathbf{X}_0 + \Delta\mathbf{X})\right]^{-1}\Delta\mathbf{X}(e^{\mathbf{X}_0} + \mathbf{I}_n) \\
&\approx \frac{1}{2}(\mathbf{Y}_0 - \mathbf{I}_n)\mathbf{X}_0^{-1}\Delta\mathbf{X}(\mathbf{Y}_0 + \mathbf{I}_n) \\
&= \frac{1}{2}(\mathbf{Y}_0 - \mathbf{I}_n)X_0^{-1}(\mathbf{X}_1\epsilon_1 + \cdots + \mathbf{X}_n\epsilon_n)(\mathbf{Y}_0 + I_n) \\
&= \mathbf{Y}_1\epsilon_1 + \mathbf{Y}_2\epsilon_2 + \cdots + \mathbf{Y}_n\epsilon_n
\end{aligned}
$$

where

$$\mathbf{Y}_j = \frac{1}{2}(\mathbf{Y}_0 - \mathbf{I}_n)\mathbf{X}_0^{-1}\mathbf{X}_j(\mathbf{Y}_0 + \mathbf{I}_n) \quad (j = 1, 2, \ldots, n)$$

A more accurate method is based on the so-called Pade approximation [108], [109], where the matrix $\exp$ is expanded as

Pade Approximation:

$$\exp(\mathbf{X}) \approx \left[\mathbf{I}_n - \frac{1}{2}\mathbf{X} + \frac{1}{12}\mathbf{X}^2\right]^{-1}\left(\mathbf{I}_n + \frac{1}{2}\mathbf{X} + \frac{1}{12}\mathbf{X}^2\right) \tag{2.58}$$

In summary, we provided three numerical techniques for computation of affine-form interval matrix exponential. The bilinear method and the similar Pade method are more accurate and efficient than the Taylor series approximation, however, they work under conditions such as the norm of the matrix must be smaller than some specific number, and therefore impact their availability.

2.2.6 Limitations

In this chapter, we introduced the concepts of interval arithmetic and affine arithmetic, which are correlated and can be converted with each other. We have detailed in interval and affine-form operations for both scalars and matrices, some numerical techniques such as the Taylor series approximation are combined with AA for matrix operations. In Section 2.3, an error spreading method is used to distribute the additional noise terms in non-affine operations to all the existing ones, thus avoid generating too many error terms.

However, the AA method is still faced with the problem of over-estimation, especially for a long chain of computations. Although it has made a great improvement compared with IA, which determines the interval bound by means of fixing all noise symbols at extreme values of ± 1, the AA method is still limited by the affine form of center-symmetric first-order polynomials. In the next chapter, we are going to illustrate in detail the effect of over-estimation and even error explosion in AA analysis for circuits, and adopt an "uncertainty interval partitioning" technique to improve it.

Chapter 3

Worst-Case Analysis for Lumped Circuits in Time-Domain

This chapter outlines the procedure for the application of AA to the worst-case analysis of lumped circuits in time-domain.

In the previous chapter, we have introduced the mathematical background of AA techniques, and its combinations with numerical techniques, such as Taylor approximations for matrix operations. In this chapter, we start from the AA based simulation of a simple resistive network with arbitrary rank, to prove the validity of AA based matrix-operation approaches discussed in Chapter 2, then apply the proposed method to the transient analysis of lumped circuits with parametric variations.

3.1   Resistive Network

In this section, we consider a resistive network as in Fig. 3.1, where all the resistors are represented by affine-form interval conductance with a $\pm 10\%$ relative variation: $\tilde{G}_S = G_{S0} + G_{S1}\epsilon_1$, and $\tilde{G}_P = G_{P0} + G_{P1}\epsilon_2$, with the nominal values being $G_{S0} = 1\,\text{S}$, and $G_{P0} = 2\,\text{S}$. The $\pm 10\%$ tolerance gives that: $G_{S1} = 0.1G_{S0}$, $G_{P1} = 0.1G_{P0}$. $E = 1\,\text{V}$.
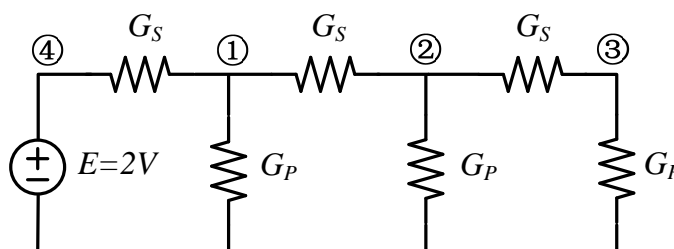

Figure 3.1.   Schematic of Resistive network.

The node voltages and source current I_e can be readily solved via the classical modified nodal analysis (MNA) tool:

$$
\begin{bmatrix}
2\tilde{G}_S + \tilde{G}_P & -\tilde{G}_S & 0 & -\tilde{G}_S & 0 \\
-\tilde{G}_S & \tilde{G}_S + \tilde{G}_P & -\tilde{G}_S & 0 & 0 \\
0 & -\tilde{G}_S & \tilde{G}_S + \tilde{G}_P & 0 & 0 \\
-\tilde{G}_S & 0 & 0 & \tilde{G}_S & 1 \\
0 & 0 & 0 & 1 & 0
\end{bmatrix}
\cdot
\begin{bmatrix}
V_1 \\ V_2 \\ V_3 \\ V_4 \\ I_e
\end{bmatrix}
=
\begin{bmatrix}
0 \\ 0 \\ 0 \\ 0 \\ E
\end{bmatrix}
\qquad (3.1)
$$

The voltages and current are obtained via the Sherman-Morrison formula for affine form matrix inversion (See Section 2.2.4). Table 3.1 shows the upper and lower limit values for voltages at the nodes computed via MC and AA, respectively. The results demonstrated that AA always provides a tight outer bounds, thus verifying the accuracy of AA in matrix operations. Moreover, the computation time is here 1.24 s for the 10,000 MC simulations and 0.024 s for the AA simulation.

Table 3.1.   Comparison of affine and Monte Carlo estimation of the node voltages.

	Upper bound			Lower bound		
	Monte Carlo	Affine std.	E-Spread	Monte Carlo	Affine std.	E-Spread
V_1	0.2292	0.2312	0.2310	0.1885	0.1864	0.1866
V_2	0.0531	0.0543	0.0540	0.0357	0.0336	0.0339
V_3	0.0148	0.0152	0.0151	0.0080	0.0067	0.0069
V_4	1.0000	1.0000	1.0000	1.0000	1.0000	1.0000
I_e	-0.719	-0.706	-0.717	-0.862	-0.876	-0.865

For this very example, we can expand it to any arbitrary large size with such basic blocks. For instance, Table 3.2 shows the upper and lower limit values of node voltages for a configuration with twice the size of that in Fig. 3.1.

In both cases, we have used Monte Carlo, the "standard" affine method (as is discussed in Section 2.2.2) which generates extra noise symbols, and the "error spreading" method (See Section 2.2.3) which avoids generating new terms. Denote them as MC, AA std. and E-Spread. From the values in the table we can tell that the error spreading routines provide even tighter upper and lower bounds than the standard routines. However, it is unknown whether this "improvement" would cause under-estimation. For computation time, "E-Spread" is twice faster than "AA std.".

3.2   Time-Domain Analysis of Lumped Circuits

Affine-based approximations have been applied in time-domain analysis of lumped circuits with the inclusion of circuit parameter variations [52]. In [50], Femia et al. have applied a genetic algorithms (GA) method and the standard AA method to the calculation of transient responses of linear RC circuit, for the approximation of affine-form matrix exponential, they adopted a geometric-series method.

In this section, we would fullfil the routines for affine form transient responses of the linear circuit in Fig. 3.2 via Matlab.

Table 3.2.   Comparison of affine and Monte Carlo estimation of the node voltages.

	Upper bound			Lower bound		
	Monte Carlo	Affine std.	E-Spread	Monte Carlo	Affine std.	E-Spread
V_1	0.2292	0.2310	0.2309	0.1886	0.1865	0.1866
V_2	0.0525	0.0534	0.0535	0.0356	0.0337	0.0338
V_3	0.0120	0.0124	0.0124	0.0067	0.0058	0.0059
V_4	0.0028	0.0029	0.0028	0.0013	0.0009	0.0009
V_5	6.32×10^{-4}	6.75×10^{-4}	6.74×10^{-4}	2.38×10^{-4}	1.17×10^{-4}	1.18×10^{-4}
V_6	1.45×10^{-4}	1.59×10^{-4}	1.58×10^{-4}	4.50×10^{-5}	6.62×10^{-6}	7.02×10^{-6}
V_7	3.36×10^{-5}	3.79×10^{-5}	3.77×10^{-5}	8.53×10^{-6}	2.93×10^{-6}	3.03×10^{-6}
V_8	9.36×10^{-6}	1.07×10^{-5}	1.07×10^{-5}	1.90×10^{-6}	-2.02×10^{-6}	-1.99×10^{-6}
V_9	1.0000	1.0000	1.0000	1.0000	1.0000	1.0000
I_e	-0.720	-0.707	-0.717	-0.863	-0.876	-0.865
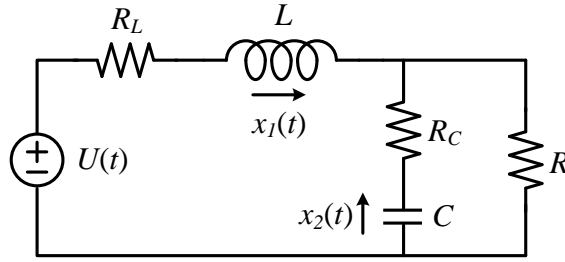
Figure 3.2.   Schematic of linear RC circuit.

The nominal values of the circuit parameters are as follows: $L = 1\,\mathrm{mH}$, $R_L = 0.5\,\Omega$, $C = 10\,\mu\mathrm{F}$, $R_C = 0.5\,\Omega$, $R = 20\,\Omega$, all affected by a $\pm 5\,\%$ tolerance. The step-wise input voltage $u(t) = 10 \cdot 1(t)$. The state-space model of the Fig. 3.2 circuit is $\dot{x}(t) = \tilde{\mathbf{A}}x(t) + \tilde{\mathbf{b}}u(t)$, where $x(t) = [i_L(t), v_C(t)]^T$ is the state vector, with $x(0) = [0, 0]^T$, and

$$\tilde{\mathbf{A}} = \begin{bmatrix} -\left(\tilde{R}_L + \tilde{R}//\tilde{R}_C\right)/\tilde{L} & -\tilde{R}//\tilde{R}_C/(\tilde{L}\tilde{R}_C) \\ \tilde{R}//\tilde{R}_C/(\tilde{C}\tilde{R}_C) & -\tilde{R}//\tilde{R}_C/(\tilde{C}\tilde{R}\tilde{R}_C) \end{bmatrix}$$

$$\tilde{\mathbf{b}} = \left[1/\tilde{L}, 0\right]^T \tag{3.2}$$

are interval valued matrices. $a//b$ stands for $a \cdot b/(a + b)$.

For the sake of simplicity, the continuous-time model is converted to the sample-data discrete model:

$$\tilde{\mathbf{X}}(k + 1) = \tilde{\mathbf{A}}_d\tilde{\mathbf{X}}(k) + \tilde{\mathbf{A}}_d u(k). \tag{3.3}$$

where

$$\tilde{\mathbf{A}}_d = \exp(\tilde{\mathbf{A}}\Delta t)$$
$$\tilde{\mathbf{B}}_d = \tilde{\mathbf{A}}^{-1}(\tilde{\mathbf{A}}_d - I)\tilde{\mathbf{b}} \tag{3.4}$$

Since there are totally five random parameters in this model (represented in the standard affine form), and they are involved in a number of operations in (3.2). The parameter matrix $\tilde{\mathbf{A}}$ can therefore be expanded as the affine form interval matrix consisting of a total number of 12 random variables (according to rules the non-affine operations in Section 2.2.2):

$$\tilde{\mathbf{A}}_d = \mathbf{A}_{d0} + \mathbf{A}_{d1}\epsilon_1 + \mathbf{A}_{d2}\epsilon_2 + \ldots \mathbf{A}_{d12}\epsilon_{12} \tag{3.5}$$

The solution of (3.3)– (3.4) requires a number of time-step iterations consisting in numerical approximations of affine form matrix exponential and inversion. Fig. 3.3 shows the result of the analysis obtained with $\Delta t = 5\,\mu s$, where we have adopted the Pade approximation for matrix exp. (see (2.58)) and the Sherman-Morrison formulas for matrix inversion (refer to (2.43)). The gray lines are provided by 10,000 MC runs, and the black lines are AA-based bounds. The closeness of the inner (MC) and the outer (AA) solutions ensures the "true worst-case" is tightly embedded.
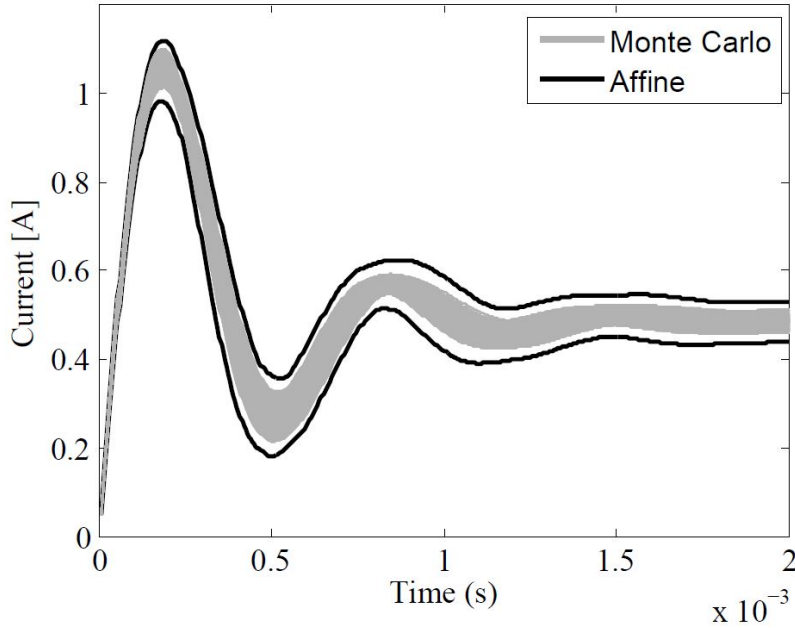

Figure 3.3.   Inductor current step transient response. Gray: MC simulations (10,000 runs), black: AA.

In [50], the authors have calculated the interval exponential matrix using a series expansion of the dynamic matrix which, for a fixed sampling rate, requires a reduced number of terms. However, in the mathematical background of Chapter 2, we have discussed three numerical approaches, all aimed at mimnimize the error explosion effect. Fig. 3.4 shows the result of inductor current and capacitor voltage step transient responses obtained from the three numerical techniques: Taylor

series, bilinear and Pade for the calculation of affine form matrix exponential. As can be seen from Fig. 3.4, the three approaches exhibit more or less the same effects and efficiency for the computation.
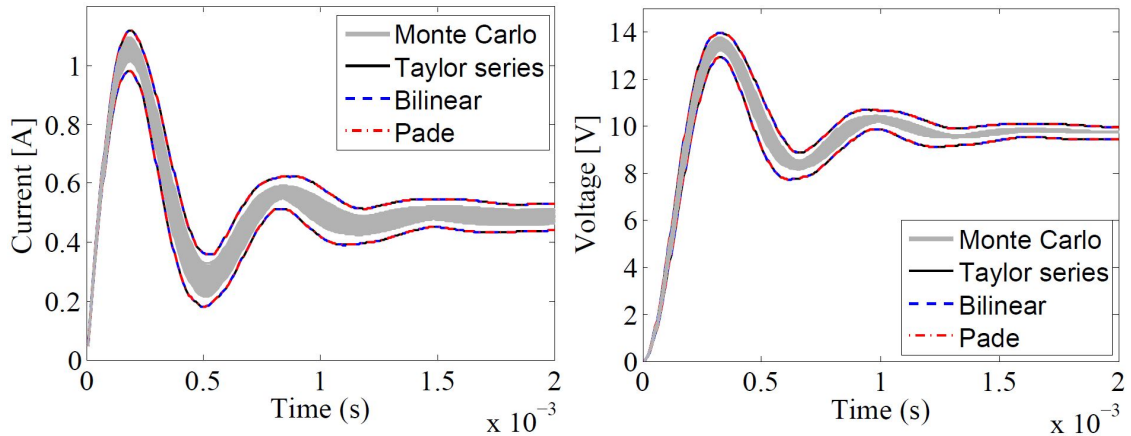

Figure 3.4. Inductor current and capacitor voltage step transient responses obtained from three numerical techniques for the affine form matrix exponential approximation. Gray: MC simulations (10,000 runs), black: AA with Taylor's expansions, dashed blue: AA with bilinear approximation, dot dashed red: AA with Pade approximation.
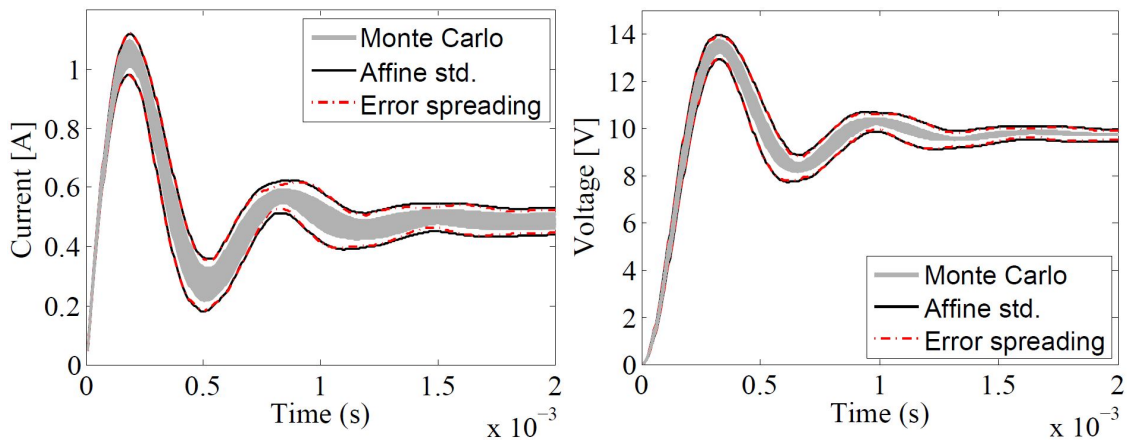
Figure 3.5. Inductor current and capacitor voltage step transient responses. Gray: MC simulations (10,000 runs), black: AA with standard operation routines, dot dashed red: AA with error spreading operation routines inside the iteration.

However, as we mentioned before, The affine operation (each time) generates at least one new variable. When solving the discrete-time model in this example, we need to calculate affine form multiplications in 400 time-steps, leading as last to a total number of 412 random variables. This can be rather cumbersome. In order to optimize this algorithm, we have modified the affine form multiplication in Section 2.2.3 according to the error spreading idea [99], and applied it to the

previous test example of resistive network (with fairly good improvement).

Figure 3.5 shows the inductor current and capacitor voltage step transient responses via MC, the standard affine method and the error-spreading-modified affine method (The error spreading operations are only used in the iterations and the number of random varibles is 12 in the end). The latter one (dot dashed red line) ensures a tighter embedded outer solutions than the standard affine operations, and the simulation time for the three methods are: MC vs. AA std. vs. E-Spread = 65.9 s vs. 0.83 s vs. 0.26 s.

In Fig. 3.6, the expansion of the paramter matrix $\tilde{\mathbf{A}}$ in (3.2) is also implemented with the error spreading method, and the result of inductor current and capacitor voltage achieved even better closeness. However, there may exist some under-estimation for the outer solutions, due to the the problem of inaccuracy of the distribution rules (see Section 2.2.3).
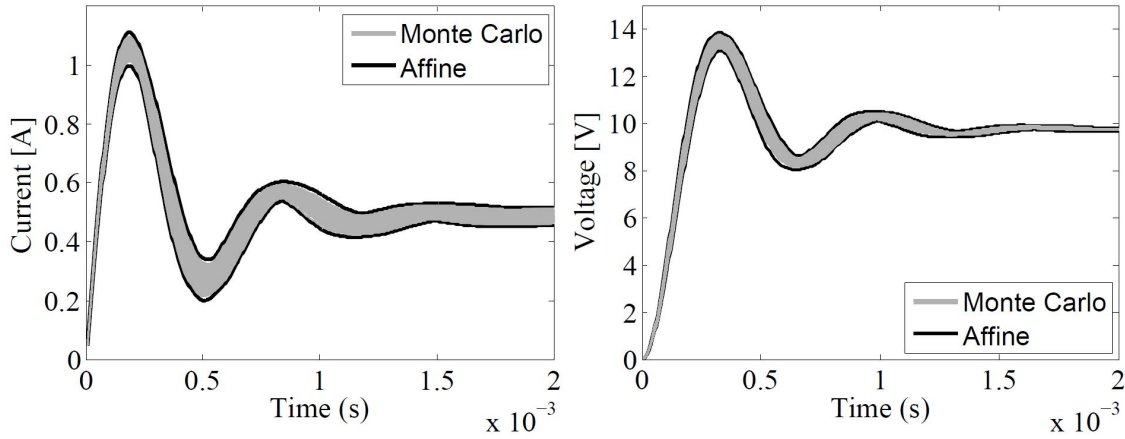

Figure 3.6.   Inductor current and capacitor voltage step transient responses. Gray: MC simulations (10,000 runs), black: AA with error spreading operation routines.

3.3   Accuracy Improvement

3.3.1   Over-Conservatism

In this section, we would fathom in the time-domain analysis of lumped circuits. Continue with the same structure illustrated in Fig. 3.2, and suppose all the circuit parameters are affected by a $\pm 10\,\%$ tolerance. The AA bounds (black lines) in Fig. 3.7 obviously provide a rough approximation.

In order to improve the accuracy of the system response behavior via AA, we adopted the so-called uncertainty interval partitioning (UIP) technique.

3.3.2   Uncertainty Interval Partitioning

Figure 3.8 helps visualizing the concept behind this UIP technique for the case of two generic variables x and y.
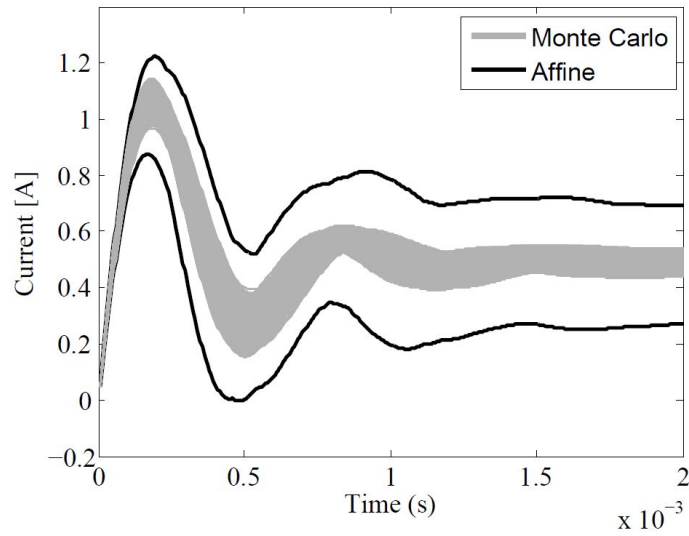
Figure 3.7.   Inductor current step transient responses exhibit over-conservatism. Gray: MC simulations (10,000 runs), black: AA with error spreading operation routines.
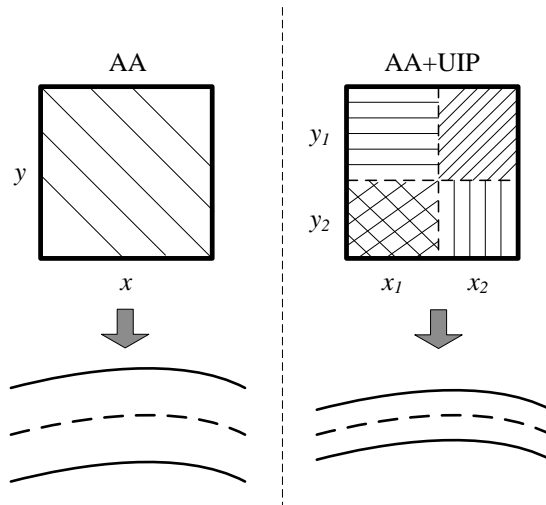

Figure 3.8.   Graphical illustration of the UIP technique based on two uncertainties (defining x and y intervals on the left) splitted into two subintervals (panel on the right).

Roughly speaking, the UIP technique aims at subdividing the uncertain interval of the parameters into smaller ones, and for each subinterval, computes the response range separately via the AA tool. Femia et. al. have used it to increase the accuracy of IA-based computations [52], [110]. Take an example of UIP optimization for IA evaluation. given a function:

$$f(x, y) = 10 - (x - 4)^2 - (y - 4)^2 \tag{3.6}$$

Both x and y range from three to six: $x \subset X = [3, 6]$, $y \subset Y = [3, 6]$. Compute the range of the function with the classical interval arithmetic, we can only obtain:

$$\begin{aligned} \bar{f} &= 10 - ([3, 6] - 4)^2 - ([3, 6] - 4)^2 \\ &\subset F = [2, 14] \end{aligned} \tag{3.7}$$

This corresponds to case (a) in Fig. 3.9. Apparently the interval is much larger than the true range. With the parititioning method, we divide the interval of x and y into two subintervals: $x_1 \subset [3, 4]$, $x_2 \subset [4, 6]$, and $y_1 \subset [3, 4]$, $y_2 \subset [4, 6]$. Each arbitrary combination of these subintervals would generate a sub-range for the function. The final interval calculated with UIP is exactly the true range of $\bar{f} \subset F_{UIP} = [2, 10]$ as is case (b) in Fig. 3.9.
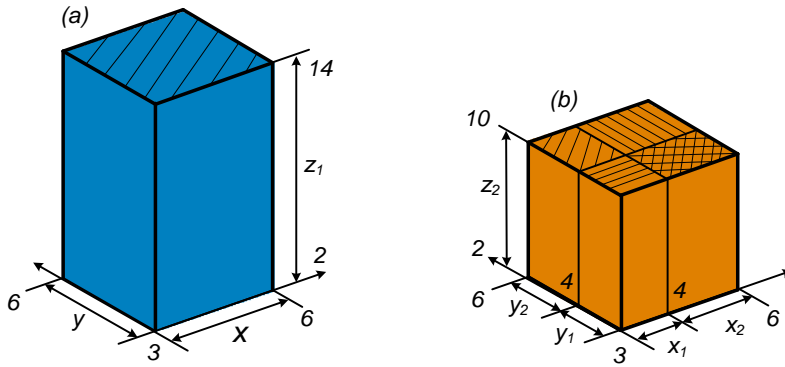

Figure 3.9.   Effect of UIP on interval computations.

Apparently, the selection of the breakpoint determines the effect of UIP, however, we are not usually so lucky to find the right breakpoint. In general, the more partitions it uses, the better accuracy it achieves, and in some extreme situations, a large quantity of partitions with geometric progression is required to provide an accurate approximation. Therefore the main drawback is that, this solution unavoidably impacts on the efficiency of the method. However, in most of the applications it is still more efficient than MC.

3.3.3   Numerical Results

For the configuration of Fig. 3.2 where all the circuit parameters are random variables with $\pm 10\,\%$ tolerance, divde the tolerance intervals of each parameter into two subintervlas, as in Table 3.3.

The next step is to compute the objective function over all the combinations of subintervals. For the paritioning of this example, we get a total number of $2^5 = 32$ combinations. For each combination, the range of objective function is plotted as colored line in Fig. 3.10.

At last, make the union of all the objective function ranges, and the updated AA+UIP bounds are shown in Fig. 3.11.

Table 3.3.   Uniform partitioning of parameters in Fig. 3.2 scheme.

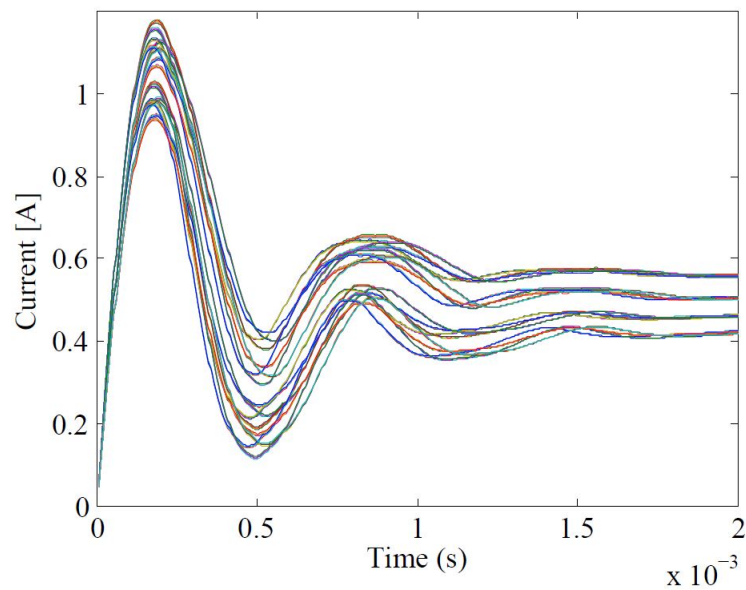| Parameter	Subinterval #1	Subinterval #2
$R = 20(1 \pm 0.1\epsilon_1)$	$[18, 20]$	$[20, 22]$
$R_C = 0.5(1 \pm 0.1\epsilon_2)$	$[0.45, 0.5]$	$[0.5, 0.55]$
$R_L = 0.5(1 \pm 0.1\epsilon_3)$	$[0.45, 0.5]$	$[0.5, 0.55]$
$L = 10^{-3}(1 \pm 0.1\epsilon_4)$	$[0.9 \times 10^{-3}, 1 \times 10^{-3}]$	$[1 \times 10^{-3}, 1.1 \times 10^{-3}]$
$C = 10^{-5}(1 \pm 0.1\epsilon_5)$	$[0.9 \times 10^{-5}, 1 \times 10^{-5}]$	$[1 \times 10^{-5}, 1.1 \times 10^{-5}]$

Figure 3.10.   Inductor current step transient responses. Gray: MC simulations (10,000 runs), colored lines: AA with 32 UIP.

3.4   Test Example with Large Uncertainties

In some extreme situations, a relatively large quantity of partitions with geometric progression is required to provide an accurate approximation.

For the Fig. 3.2 scheme, suppose the capacitor C is affected by a $\pm 50\%$ tolerance, then we are required to adopt a relatively large number of partitions (200–250) to satisfy the accuracy. The black lines in Fig. 3.12 give the upper and lower bounds obtained with AA + 250 UIP. The good accuracy is guaranteed, and even with such a large number of partitions, the AA+UIP method still achieves a speed up of $3\times$ than MC.
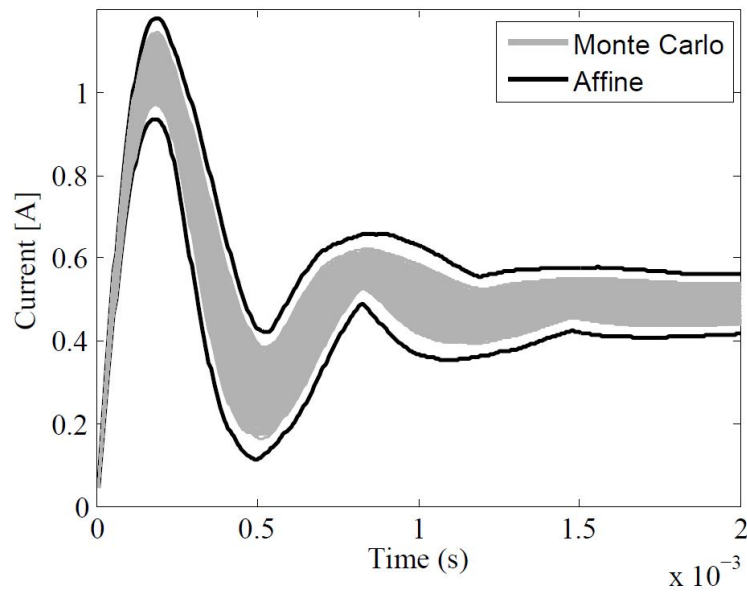
Figure 3.11.   Inductor current step transient responses. Gray: MC simulations (10,000 runs), black: the outer bounds of AA with UIP.
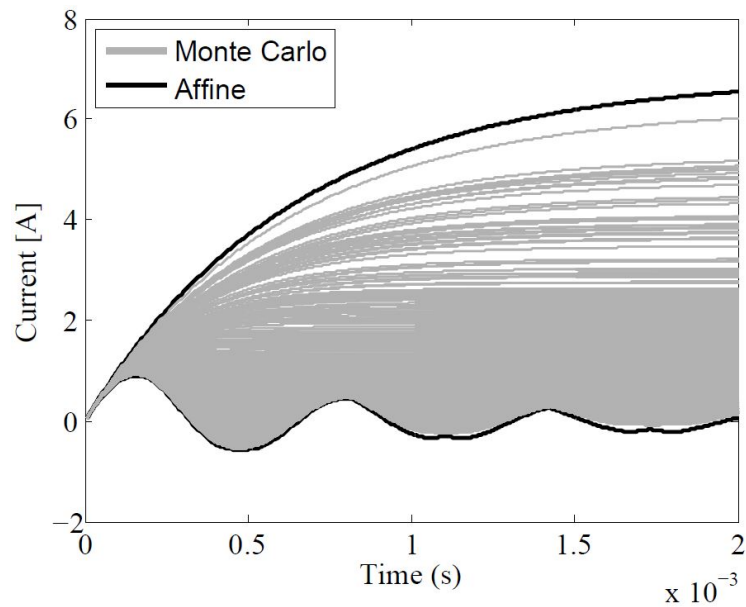

Figure 3.12.   Step transient of the inductor's current of the Fig. 3.2 scheme (The capacitance is assumed to vary within a ±50 % tolerance). Gray: MC simulations (10,000 runs), black: AA+UIP.

Chapter 4

Frequency-Domain Analysis of Lumped Circuits

In this chapter, the affine method is applied to some simple illustrative examples to highlight the main features of the proposed method for the frequency-domain analysis of dynamical circuits. In addition, the examples allow to furthur discuss the uncertainty interval partitioning based enhancements aimed at improving the accuracy of the worst-case predictions.

4.1 Test Example

We first consider the frequency-domain analysis of the RC circuit in Fig. 4.1, where the nominal values of the circuit parameters are: $G_1 = G_2 = 1\,\text{S}$, and $C_1 = 1\,\text{F}$, $C_2 = 10\,\text{F}$. The tolerance is supposed to be $\pm 10\,\%$. Magnitude of voltage source $E = 10\,\text{V}$.
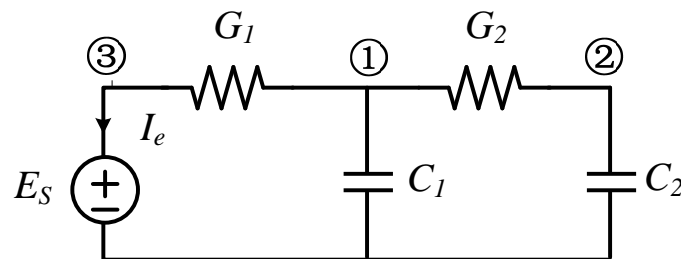

Figure 4.1.   Schematic of RC circuit.

Still, use the MNA tool for the solution of circuit nodal voltages within the frequency range of 10^{-2}–10^2 Hz. The parameter matrix here is complex vlaued interval matrix, represent it in the affine form, and we are referred to the same routines in Chapter 2 for interval matrix inversion. The frequency responses of nodal voltages V_1–V_3 and current I_e are computed via AA and MC simulations.
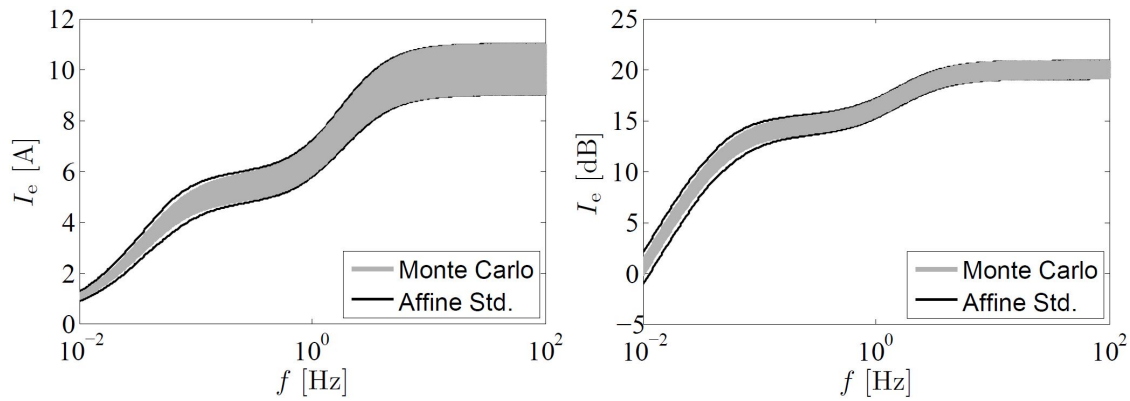
Figure 4.2. Magnitude of I_e of the scheme of Fig. 4.1, where only one random variable is considered. Gray: MC simulations (10,000 runs), black: AA with standard operations routines.
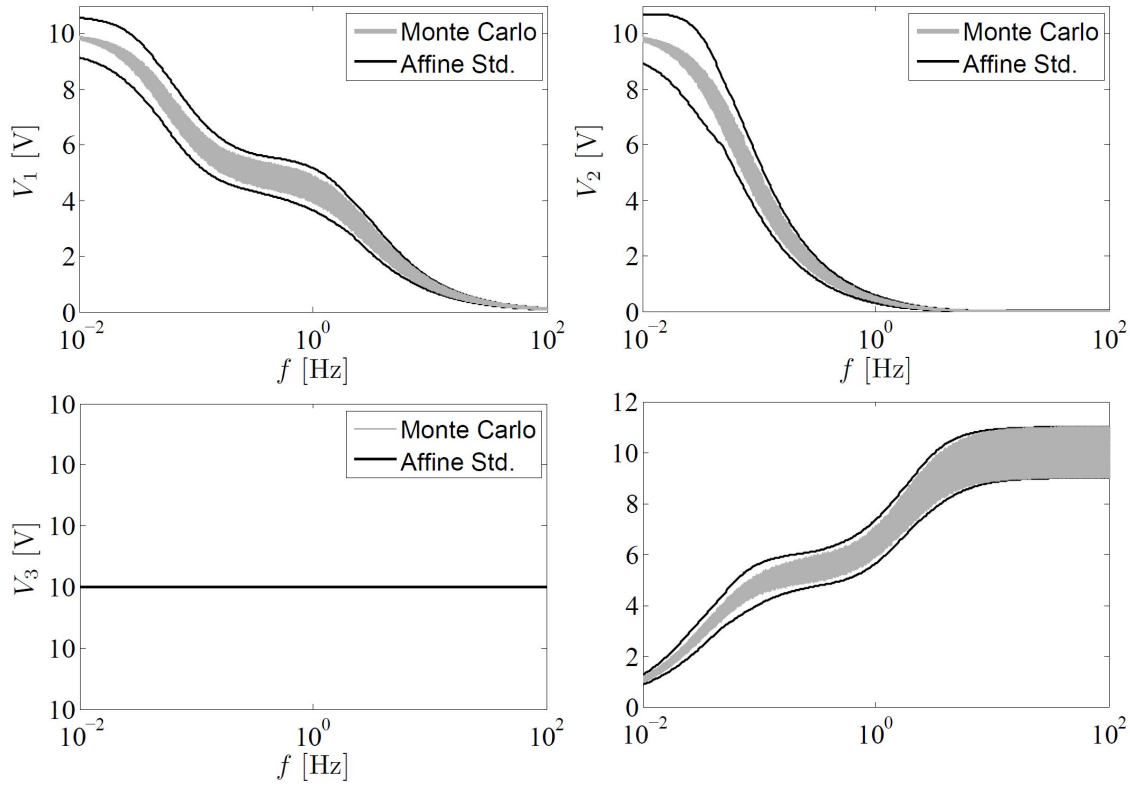

Figure 4.3. Magnitude of nodal voltages and I_e of the scheme of Fig. 4.1, where all parameters are assumed to be independent random values. Gray: MC simulations (10,000 runs), black: AA with standard routines.

For the first simulation setup, we have considered only one noise symbol representing the variabilities of all parameters, there are no fluctuations for the nodal voltages, and Fig. 4.2 illustrates

only the variation range of current I_e. In the second simulation setup, all the circuit parameters are assumed to be independent interval values, and the frequency-domain responses of voltages and current are shown in Fig. 4.3.

The closeness between AA and MC bounds verifies the capability of AA as an excellent approach in application to the frequency-domain analysis of lumped circuits. In the third simulation setup, the AA method is substituted by the error spreading approach, which again provides more accurate and efficient approxiamtions (See Fig. 4.4). The computation time of MC vs. AA std. vs. E-Spread = 41 s vs. 16 s vs. 12 s.
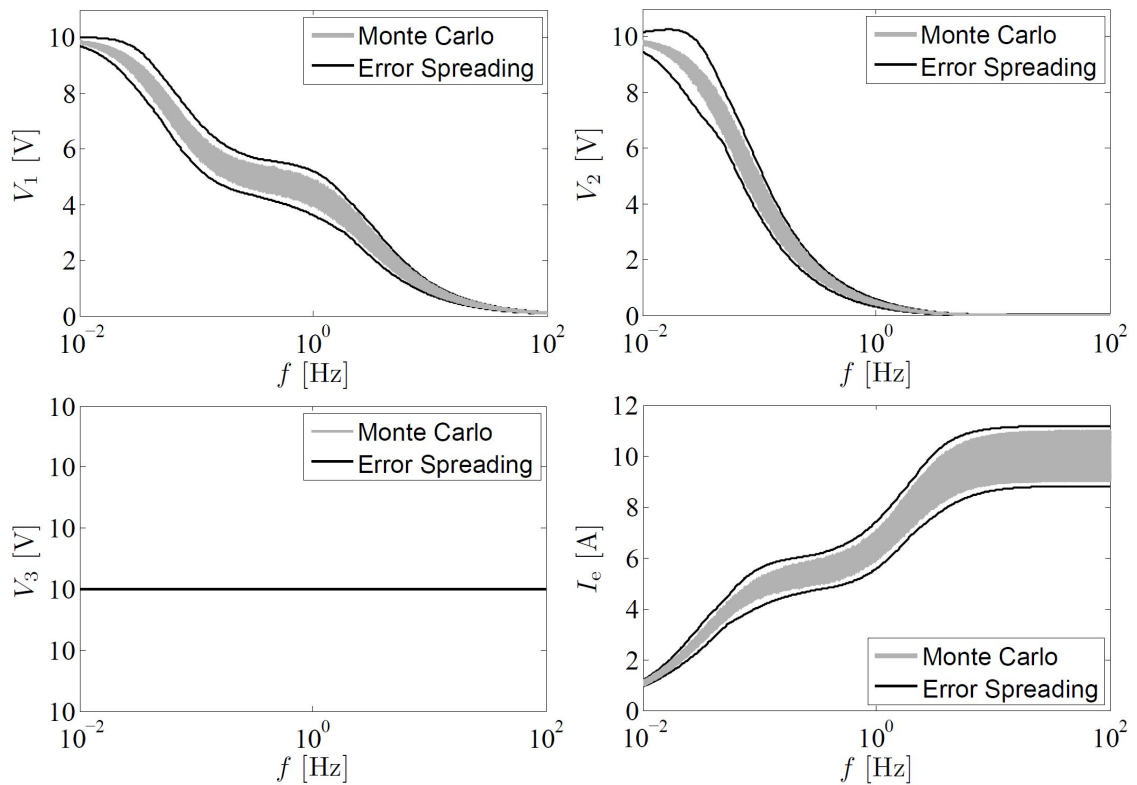

Figure 4.4.   Magnitude of nodal voltages and I_e of the scheme of Fig. 4.1, where all parameters are assumed to be independent random values. Gray: MC simulations (10,000 runs), black: AA with the error spreading routines.

4.2   Accuracy Improvement with Partitioning

We consider next a parallel and series lumped circuit block, respectively, the simulation of which benefit from the use of UIP introduced in Chapter 3.

4.2.1 RLC Circuit

Figure 4.5 shows a basic parallel block with random circuit parameters $G = 0.5(1 + 0.1\epsilon_1)\,\text{S}$, $C = 1(1 + 0.1\epsilon_2)\,\text{F}$, and $L = 1(1 + 0.1\epsilon_3)\,\text{H}$.
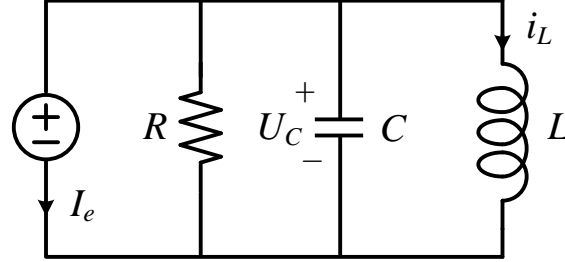

Figure 4.5.   Parallel RLC circuit.

Figure 4.6 and Fig. 4.7 show the bounds of inductor current i_L computed via AA+3 UIP and AA+6 UIP, respectively. In both situations, we have shown the objective range computed via each combination of subintervals (in the left panel) and the union of the subranges (in the right panel). The effect of UIP is not obvious in this simulation setup. However in the next example, we consider a cascaded series lumped circuit model, the use of UIP is indeed necessary, especially when the circuit exhibits strong resonant behavior.
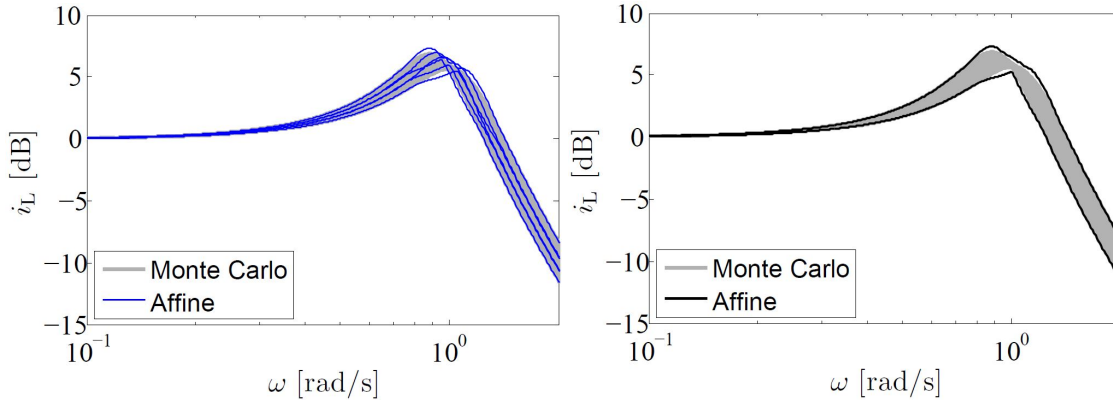

Figure 4.6.   Frequency-domain responses of inductor current i_L of the lumped circuit in Fig. 4.5. Gray: MC simulations (10,000 runs), blue lines: AA with 3 UIP, black: AA combined bounds.

4.2.2 Higher Order Circuit

The circuit parameters of the series model in Fig 4.8, are defined as: $C = C_0 + C_1\epsilon_1$, $L = L_0 + L_2\epsilon_2$ and $G = G_0 + G_3\epsilon_3$, being all the parameters assumed as independent variables affected by the same $\pm10\%$ variability ($C_0 = 1\,\text{F}$, $L_0 = 1\,\text{H}$, $G_0 = 1\,\text{S}$, $C_1 = \Delta C_0$, $L_2 = \Delta L_0$, $G_3 = \Delta G_0$ and $\Delta = 0.1$).
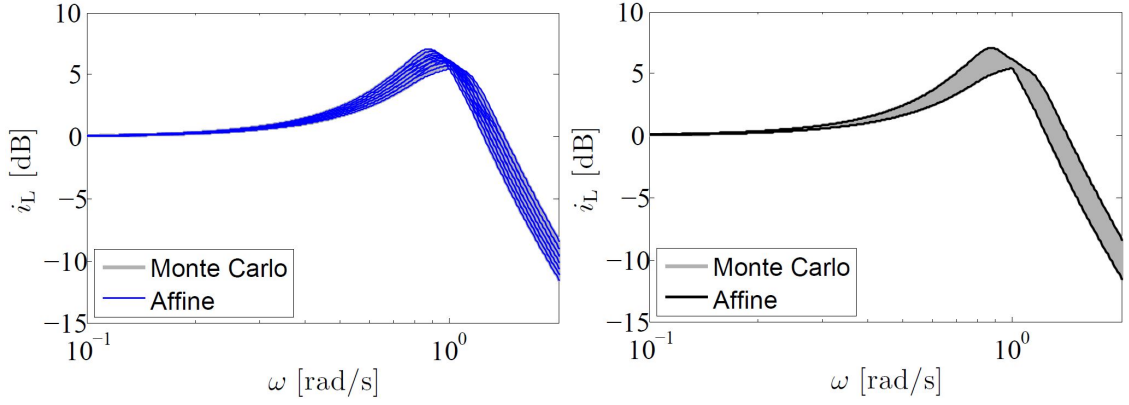
Figure 4.7. Frequency-domain responses of inductor current i_L of the lumped circuit in Fig. 4.5. Gray: MC simulations (10,000 runs), blue lines: AA with 6 UIP, black: AA combined bounds.
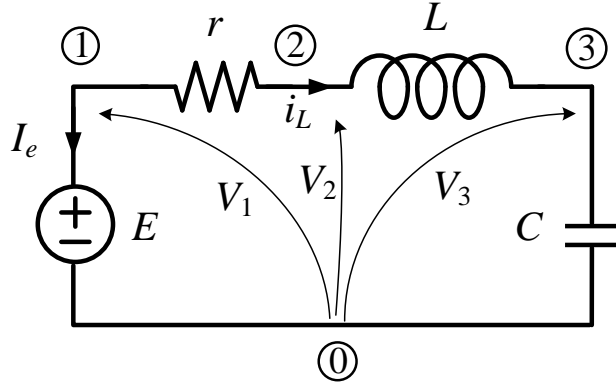

Figure 4.8. A basic RLC block of cascade structure.

The frequency-domain solution of the above circuit can be obtained via the classical modified nodal analysis (MNA) tool:

$$\tilde{\mathbf{M}}\tilde{\mathbf{W}} = \tilde{\mathbf{J}} \tag{4.1}$$

where $\tilde{\mathbf{W}} = [V_1(j\omega), V_2(j\omega), V_3(j\omega), I_L(j\omega), I_e(j\omega)]^T$ collects the phasors of the unknown variables, $\tilde{\mathbf{J}} = [0, 0, 0, 0, E(j\omega)]^T$ and

$$
\tilde{\mathbf{M}} =
\begin{bmatrix}
g_0 & -g_0 & 0 & 0 & 1 \\
-g_0 & g_0 & 0 & 1 & 0 \\
0 & 0 & j\omega C_0 & -1 & 0 \\
0 & 1 & -1 & -j\omega L_0 & 0 \\
1 & 0 & 0 & 0 & 0
\end{bmatrix}
+
\begin{bmatrix}
g_3\epsilon_3 & -g_3\epsilon_3 & 0 & 0 & 0 \\
-g_3\epsilon_3 & g_3\epsilon_3 & 0 & 0 & 0 \\
0 & 0 & j\omega C_1\epsilon_1 & 0 & 0 \\
0 & 0 & 0 & -j\omega L_2\epsilon_2 & 0 \\
0 & 0 & 0 & 0 & 0
\end{bmatrix}.
\tag{4.2}
$$

The above matrix is interpreted as the sum of matrices in the canonical AA form, i.e., $\tilde{\mathbf{M}} = \mathbf{M}_0 + \mathbf{M}_1\epsilon_1 + \mathbf{M}_2\epsilon_2 + \mathbf{M}_3\epsilon_3$, and the solution of the above problem is achieved via matrix inversion ($\tilde{\mathbf{W}} = \tilde{\mathbf{M}}^{-1}\tilde{\mathbf{J}}$), yielding to the response of the pertinent nodal voltages and currents defined as affine form complex values comprising information on the upper and lower bounds of system response.

As an example, Fig. 4.9 shows the bode-plot (magnitude) of the transfer function $H(j\omega) = V_3(j\omega)/E(j\omega)$ computed via AA and via 10,000 MC simulations, thus highlighting the closeness between the inner (via MC) and outer (via AA) bounds and providing a first validation of the accuracy of the proposed method. As far as the efficiency is concerned, the CPU time required to compute the bounds via AA is $4\,\text{s}$ only, compared with $9\,\text{min}$ for the MC case, that turns out to be unavoidably heavier. The simulations are carried out using Matlab on a Intel i5-2467M Quad-Core notebook operating at $1.6\,\text{GHz}$.
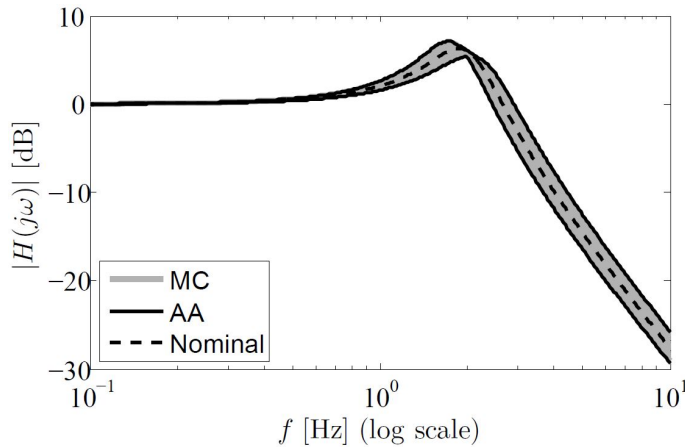

Figure 4.9. Bode plot (magnitude) of the transfer function $H(j\omega) = V_3(j\omega)/E(j\omega)$ of the example lumped circuit of Fig. 4.8. Dashed line: nominal response obtained with the deterministic values of components; solid black lines: upper and lower bounds obtained via AA; gray lines: MC samples.

The performance of the AA method highlighted in the previous example is confirmed for lumped circuits that do not exhibit strong resonant behavior and with a complexity defined by a number of circuit elements in the order 3–10. However, for more complex circuits and for a richer frequency-domain dynamical behavior, some improvements are in general needed and the method benefits from suitable adjustment. As an example, Fig. 4.10 shows the response of a lumped circuit consisting of the cascade connection of three RLC blocks like the one of Fig. 4.8. All the circuit parameters are defined by independent interval variables with $\pm 10\%$ relative variation. The curves in the figure correspond to the bode plot (magnitude) of the transfer function defined as the ratio between the far-end voltage response and the input voltage excitation. From this comparison, it is clear that plain AA method provides a rough approximation of the upper bound of the system response only and that AA combined with the so-called uncertainty interval partitioning (UIP) technique leads to a major improvement and to predictions with the same accuracy observed in the previous case.
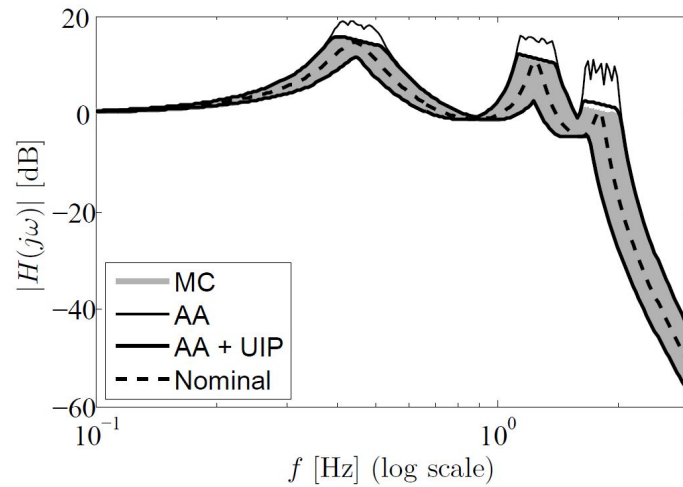
Figure 4.10. Frequency-domain response of a dynamical circuit consisting of an ideal voltage generator driving the cascade connection three lumped RLC block like the one of Fig. 4.8. Dashed line: nominal response obtained with the deterministic values of components; solid thin black lines: upper and lower bounds obtained via AA; solid thick black lines: bounds obtained via the joint application of AA and the UIP technique (a total number of 5 partitions is used); gray lines: MC samples.

4.3 Lumped Circuit Equivalent of Two-Conductor Transmission-Lines

In the last part of this Chapter, we considered the lumped circuit model of two-conductor transmission lines. The basic block of Fig. 4.11 represents an unit of the cable, with per-unit-length parameters:
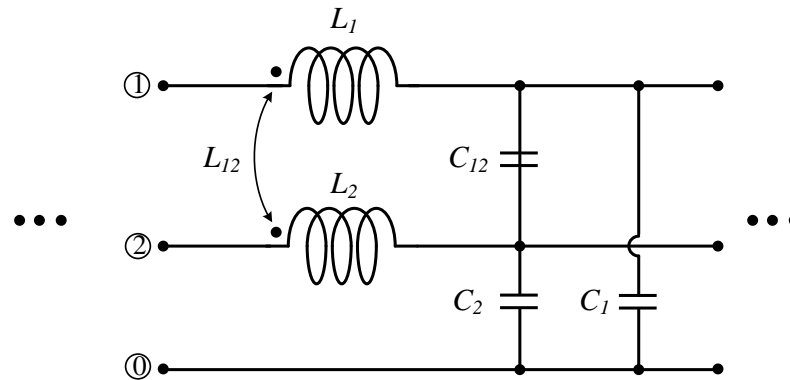

Figure 4.11. One block of the cascade lumped circuit model of transmission line structure.

$$\mathbf{L} = \begin{bmatrix} 670 & 360 \\ 360 & 670 \end{bmatrix} \mathrm{nH/m} \quad \tilde{\mathbf{C}} = \begin{bmatrix} 30 & 26 \\ 26 & 30 \end{bmatrix} (1 + 0.1\epsilon_1)\,\mathrm{pF/m}$$

for a cable with length $\mathcal{L} = 5\,\mathrm{cm}$, we have used 100 such basic blocks. Bode plot (magnitude) of the cross talk transfer function of this model is shown in Fig. 4.12, which again verifies the capability of AA with non-uniform UIP in dealing with a relatively large simulation system. However it becomes less efficient in terms of the simulation time (MC vs. AA+UIP = 1.5:1). Therefore, in the next chapter, we are going to approximate the distributed lines responses with parameter variations by means of modifying the telegrapher's equations to the affine form.
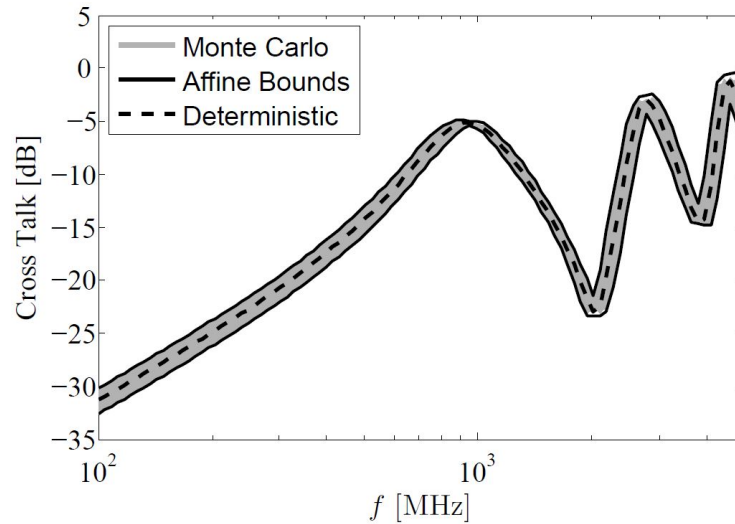

Figure 4.12.   Bode plot (magnitude) of the cross talk transfer function of the lumped circuit model of transmission line (100 cascade connection of blocks like the one in Fig. 4.11). Dashed line: nominal response obtained with the deterministic values of components; solid black lines: upper and lower bounds obtained via AA; gray lines: MC samples.

Chapter 5

Frequency-Domain Analysis of Distributed Lines

The first half of this chapter (Section 5.1-5.2) starts from the governing equations for the signal propagation along a multiconductor transmission line (MTL), which is the basic element for high-speed interconnects, in their deterministic formulation. Then two numerical examples are presented for both single bare wire and coupled lines. Deterministic responses of far-end voltage and cross talk are obtained by means of solving the telegrapher's equations. In the second part, the per-unit-length parameters of the coupled lines are assumed to be affected by a $\pm 10\%$ variation, and a tutorial description of application of AA in the distributed line structures is provided.

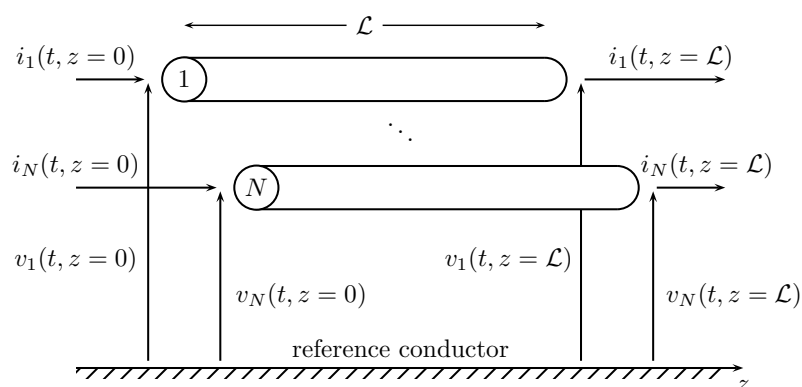Figure 5.1.   Illustration of a uniform multiconductor transmission line with N conductors of length $\mathcal{L}$. The definition of voltages and currents is also shown.

5.1   The Multiconductor Transmission-Line Equations

Under suitable assumptions, the signal propagation along N coupled conductors plus one reference conductor (see Fig. 5.1), all uniform along the direction z, is described by the MTL or

telegrapher's equations [112]:

$$\frac{\partial}{\partial z}\mathbf{v}(z,t) = -\mathbf{R}\mathbf{i}(z,t) - \mathbf{L}\frac{\partial}{\partial t}\mathbf{i}(z,t) \tag{5.1a}$$

$$\frac{\partial}{\partial z}\mathbf{i}(z,t) = -\mathbf{G}\mathbf{v}(z,t) - \mathbf{C}\frac{\partial}{\partial t}\mathbf{v}(z,t) \tag{5.1b}$$

where $\mathbf{v} = [v_1, \ldots, v_N]^T$ and $\mathbf{i} = [i_1, \ldots, i_N]^T$ are vectors of size N, collecting the voltages between each signal conductor and the reference as well as the currents flowing into them, respectively. The $N \times N$ matrices $\mathbf{R}$ (resistance), $\mathbf{L}$ (inductance), $\mathbf{G}$ (conductance), $\mathbf{C}$ (capacitance) are the per-unit-length (p.u.l.) parameters and contain all the information on the electromagnetic field and the coupling among the conductors. The knowledge of such parameters is the key point in the solution of the MTL equations.

5.1.1 The Quasi-TEM Assumption

According to the above transmission-line formulation, the structure is assumed to be distributed along the direction of propagation z but lumped, i.e., electrically small, in its cross-section. As such, the validity of the above equations is restricted to the case of transverse electromagnetic (TEM) field propagation, which means that both the electric and magnetic fields surrounding the conductors are perpendicular to the line axis z. Electrically large cross-sectional dimensions give rise to additional modes of propagation, thus invalidating the TEM assumption. Another circumstance that invalidates the TEM assumption is the presence of lossy conductors and inhomogeneous surrounding media. However, as long as such violations are not extreme, the transmission-line formulation can still be considered as representative, although approximated. This situation is referred to as the *quasi-TEM* assumption. Finally, the transmission-line formulation inherently assumes that all the currents sum to zero at any cross-section. In other words, the reference conductor is the return for all the other N currents. But this might not be true, for instance in presence of nearby metallic structures that are not included in the analysis. In order to obtain a complete solution, also accounting for other modes of propagation, one has to carry-out a *full-wave* solution of Maxwell's equations.

5.1.2 The Per-Unit-Length Parameters

As already remarked, the p.u.l. parameters $\mathbf{R}$, $\mathbf{L}$, $\mathbf{G}$, $\mathbf{C}$ contain all the key information about the propagation along each conductor as well as the coupling among different conductors. Specifically,

- the p.u.l. inductance matrix $\mathbf{L}$ relates the currents flowing into the conductors to the p.u.l. magnetic fluxes penetrating the paths defined between each signal conductor and the reference. It has the following shape:

$$\mathbf{L} = \begin{bmatrix} l_{11} & l_{12} & \cdots & l_{1N} \\ l_{21} & l_{22} & \cdots & l_{2N} \\ \vdots & \vdots & \ddots & \vdots \\ l_{N1} & l_{N2} & \cdots & l_{NN} \end{bmatrix} \tag{5.2}$$

where l_{ii} is the p.u.l. self-inductance of conductor i and l_{ij} is the p.u.l. mutual inductance between conductors i and j.

- The p.u.l. capacitance matrix $\mathbf{C}$ relates the total p.u.l. charges on the conductors to the line voltages producing them. Its entries are defined as:

$$\mathbf{C} = \begin{bmatrix} \sum_{k=1}^{N} c_{1k} & -c_{12} & \cdots & -c_{1N} \\ -c_{21} & \sum_{k=1}^{N} c_{2k} & \cdots & -c_{2N} \\ \vdots & \vdots & \ddots & \vdots \\ -c_{N1} & -c_{N2} & \cdots & \sum_{k=1}^{N} c_{Nk} \end{bmatrix} \tag{5.3}$$

with c_{ii} the p.u.l. capacitance between the ith conductor and the reference and c_{ij} the p.u.l. capacitance between conductors i and j.

- The p.u.l. conductance matrix $\mathbf{G}$ relates the total p.u.l. transverse conduction currents passing between the conductors to the line voltages producing them. Its elements are organized similarly to those of the capacitance matrix:

$$\mathbf{G} = \begin{bmatrix} \sum_{k=1}^{N} g_{1k} & -g_{12} & \cdots & -g_{1N} \\ -g_{21} & \sum_{k=1}^{N} g_{2k} & \cdots & -g_{2N} \\ \vdots & \vdots & \ddots & \vdots \\ -g_{N1} & -g_{N2} & \cdots & \sum_{k=1}^{N} g_{Nk} \end{bmatrix} \tag{5.4}$$

with g_{ii} and g_{ij} the p.u.l. conductances between the different conductors or the reference, respectively.

- The entries of the p.u.l. resistance matrix $\mathbf{R}$ can be related to the p.u.l. resistance of the isolated conductors to a reasonable degree of accuracy, although in general one should account for the fact that the fields exterior and interior to the imperfect conductors interact. It has therefore the following shape:

$$\mathbf{R} = \begin{bmatrix} r_1 + r_0 & r_0 & \cdots & r_0 \\ r_0 & r_2 + r_0 & \cdots & r_0 \\ \vdots & \vdots & \ddots & \vdots \\ r_0 & r_0 & \cdots & r_N + r_0 \end{bmatrix} \tag{5.5}$$

where r_i is the p.u.l. resistance of the ith conductor ($i = 0$ denoting the reference conductor).

One important property of the p.u.l. matrices is that they are symmetric (in presence of reciprocal materials). Under the TEM assumption, the entries of the p.u.l. inductance matrix $\mathbf{L}$, conductance matrix $\mathbf{G}$ and of the capacitance matrix $\mathbf{C}$ are related to the fields external to the conductors and are determined as the *static* field solutions in the transverse plane assuming perfect conductors. The entries of the p.u.l. resistance matrix $\mathbf{R}$ are instead governed by the fields interior to the imperfect conductors.

The ease of determination of the p.u.l. parameters is related to the cross-sectional structure. For cylindrical conductors in a homogeneous medium, closed-form analytical formulas for the entries of the p.u.l. inductance are available. We limit ourselves to mention those for wires above a perfectly-conducting ground plane:

$$l_{ii} = \frac{\mu}{2\pi} \cosh^{-1}\left(\frac{h_i}{r_{w_i}}\right) \tag{5.6a}$$

$$l_{ij} = \frac{\mu}{4\pi} \ln\left(1 + 4\frac{h_i h_j}{d_{ij}^2}\right) \tag{5.6b}$$

where h_i and r_{w_i} are the height and the radius of wire i, respectively, d_{ij} is the distance between wire i and wire j, and μ is the permeability of the embedding medium. The capacitance and inductance matrices can be obtained through the following relations, valid for homogeneous media:

$$\mathbf{C} = \mu\varepsilon\mathbf{L}^{-1} \tag{5.7}$$

and

$$\mathbf{G} = \frac{\sigma_d}{\varepsilon}\mathbf{C} = \sigma_d\mu\mathbf{L}^{-1} \tag{5.8}$$

where μ, ε and σ_d are the permeability, permittivity and conductivity of the embedding material, respectively. When the conductors have different shapes and/or the surrounding medium is inhomogeneous, numerical computations are required [113].

5.1.3   Dispersive Lines

The material properties, as well as the distribution of the currents inside the imperfect conductors, depend on the frequency of the excitation signals. Hence, the p.u.l. parameters are generally *dispersive* (i.e., frequency dependent), and therefore more correctly indicated as $\mathbf{R}(\omega)$, $\mathbf{L}(\omega)$, $\mathbf{G}(\omega)$ and $\mathbf{C}(\omega)$, with $\omega = 2\pi f$ the angular frequency. As we will see, the dispersive behavior is hard to be characterized directly in time domain, but can be readily incorporated by writing the MTL equations in the frequency domain. In particular, because of the *skin effect*, the currents flowing into the imperfect conductors migrate towards the conductor surfaces and, as a result, their p.u.l. resistances increase proportionally to $\sqrt{f}$. Also, these internal currents give rise to internal magnetic fluxes, that in turn yield an additional component to the p.u.l. inductance matrix, with entries decreasing as $1/\sqrt{f}$. The p.u.l. conductance matrix increases with frequency because of the loss due to the incomplete alignment of the bound charges. Finally, the p.u.l. capacitance matrix (mildly) depends on frequency because the relative permittivity of dielectrics is (mildly) frequency dependent.

Approximate relations exist for the total p.u.l. internal impedance of imperfect conductors [112]:

$$z_i(\omega) = r_i(\omega) + j\omega l_i(\omega) = \begin{cases} r_{\mathrm{dc}}(1 + j\omega/\omega_c) & \omega \leq \omega_c \\ r_{\mathrm{dc}}\sqrt{\omega/\omega_c}(1 + j) & \omega \geq \omega_c \end{cases} \tag{5.9}$$

where r_i is the p.u.l. resistance, l_i the p.u.l. internal inductance, and r_{dc} the p.u.l. DC resistance, given by the Ohm's law:

$$r_{\mathrm{dc}} = \frac{1}{\sigma_c S} \tag{5.10}$$

with σ_c the metal conductivity and S the conductor section. Moreover, $\omega_c = 2\pi f_c$ is a transition angular frequency, that for wires corresponds to the frequency at which the wire radius equals two *skin depths*, i.e.

$$f_c = \frac{4}{\pi \sigma_c \mu_0 r_w^2} \tag{5.11}$$

r_w denoting the wire radius. With the above definitions, the total p.u.l. impedance matrix is given by

$$\mathbf{Z}(\omega) = \mathbf{R}(\omega) + j\omega \mathbf{L}(\omega) = \begin{bmatrix} z_1(\omega) + z_0(\omega) & z_0(\omega) & \cdots & z_0(\omega) \\ z_0(\omega) & z_2(\omega) + z_0(\omega) & \cdots & z_0(\omega) \\ \vdots & \vdots & \ddots & \vdots \\ z_0(\omega) & z_0(\omega) & \cdots & z_N(\omega) + z_0(\omega) \end{bmatrix} + j\omega\mathbf{L}_e \tag{5.12}$$

where $\mathbf{L}_e$ is the classical "external" p.u.l. inductance, defined by (5.2).

Sometimes, the lines can be assumed as lossless, i.e. with $\mathbf{R} = \mathbf{G} = \mathbf{0}$, and/or dispersion-free, whereas in the most general case, the accurate computation of the frequency-dependent p.u.l. parameters is highly nontrivial and requires complex numerical calculations.

5.2   Solution of the Multiconductor Transmission-Line Equations

The system (5.1) describes the behavior of the signals in the MTL. Its solution allows the analysis of the signal propagation along the line as well as of the unintentional interaction (crosstalk) due to the electromagnetic coupling among different conductors. The solution of the MTL equations usually follows the following three-step procedure [112]:

1. Determination, either analytically or numerically, of the p.u.l. parameters for the given line geometry.

2. Computation of the general solution of the line, consisting of N forward- and N backward-traveling waves, with $2N$ unknown coefficients.

3. Incorporation of the terminal (boundary) conditions to determine the unknown coefficients.

The final step allows to fully characterize the system and to solve a given line for a given configuration of its terminations (that typically include independent sources, lumped elements, diodes, etc.). Nevertheless, the time-domain computation of the general solution is challenging whenever

the line is lossy and/or the p.u.l. parameters are frequency dependent, as these behaviors are more suitably characterized in the frequency domain. Because of this, we will mainly consider and present first the frequency-domain solution of the MTL equations. However, such a solution can take only linear terminations into account.

5.2.1 Frequency-Domain Equations

When considering the frequency domain, the excitations sources are supposed to be sinusoids which have been applied for a sufficiently long time so that all transients have decayed to zero, i.e. the line is in *steady state*. Therefore, the line voltages and currents are also sinusoids. Using the *phasor* notation, we have:

$$\mathbf{v}(z,t) = \Re\left\{\mathbf{V}(z)e^{j\omega t}\right\} \tag{5.13a}$$

$$\mathbf{i}(z,t) = \Re\left\{\mathbf{I}(z)e^{j\omega t}\right\} \tag{5.13b}$$

where $\Re\left\{\cdot\right\}$ denotes the real part of the enclosed complex quantity. From now on, capital letters will denote frequency-domain voltages and currents, while the corresponding time-domain quantities will be expressed with small letters. According to Fourier theory, the time derivatives are replaced by $j\omega$. Therefore, the frequency-domain MTL equations become:

$$\frac{d}{dz}\mathbf{V}(z,\omega) = -\mathbf{Z}(\omega)\mathbf{I}(z,\omega) \tag{5.14a}$$

$$\frac{d}{dz}\mathbf{I}(z,\omega) = -\mathbf{Y}(\omega)\mathbf{V}(z,\omega) \tag{5.14b}$$

with

$$\mathbf{Z}(\omega) = \mathbf{R}(\omega) + j\omega\mathbf{L}(\omega) \tag{5.15a}$$

$$\mathbf{Y}(\omega) = \mathbf{G}(\omega) + j\omega\mathbf{C}(\omega) \tag{5.15b}$$

As already remarked, in this case there is no limitation about the p.u.l. parameters being frequency dependent.

5.2.2 General Solution

The second step in the solution procedure consists in the computation of the general solution of the MTL for a given frequency and length, the latter denoted with $\mathcal{L}$. This is given by the *chain parameter matrix* (CPM) [112], i.e.

$$\mathbf{\Phi}(\mathcal{L}) = \text{expm}\left(\begin{bmatrix} \mathbf{0} & -\mathbf{Z} \\ -\mathbf{Y} & \mathbf{0} \end{bmatrix}\mathcal{L}\right) \tag{5.16}$$

where `expm` denotes the matrix exponential and the frequency dependence has been dropped for notational convenience. The CPM relates the line voltages and currents at the left ($z = 0$, or near-end) termination to those at the right ($z = \mathcal{L}$, or far-end) termination, i.e.

$$\begin{bmatrix} \mathbf{V}(z=\mathcal{L}) \\ \mathbf{I}(z=\mathcal{L}) \end{bmatrix} = \begin{bmatrix} \mathbf{\Phi}_{11}(\mathcal{L}) & \mathbf{\Phi}_{12}(\mathcal{L}) \\ \mathbf{\Phi}_{21}(\mathcal{L}) & \mathbf{\Phi}_{22}(\mathcal{L}) \end{bmatrix} \begin{bmatrix} \mathbf{V}(z=0) \\ \mathbf{I}(z=0) \end{bmatrix} \tag{5.17}$$

Besides the use of the matrix exponential, the entries of the CPM can be computed as:

$$\mathbf{\Phi}_{11} = \frac{1}{2}\mathbf{Y}^{-1}\mathbf{T}(\mathrm{e}^{\gamma\mathcal{L}} + \mathrm{e}^{-\gamma\mathcal{L}})\mathbf{T}^{-1}\mathbf{Y} \tag{5.18a}$$

$$\mathbf{\Phi}_{12} = -\frac{1}{2}\mathbf{Y}^{-1}\mathbf{T}\gamma(\mathrm{e}^{\gamma\mathcal{L}} - \mathrm{e}^{-\gamma\mathcal{L}})\mathbf{T}^{-1} \tag{5.18b}$$

$$\mathbf{\Phi}_{21} = -\frac{1}{2}\mathbf{T}(\mathrm{e}^{\gamma\mathcal{L}} - \mathrm{e}^{-\gamma\mathcal{L}})\gamma^{-1}\mathbf{T}^{-1}\mathbf{Y} \tag{5.18c}$$

$$\mathbf{\Phi}_{22} = \frac{1}{2}\mathbf{T}(\mathrm{e}^{\gamma\mathcal{L}} + \mathrm{e}^{-\gamma\mathcal{L}})\mathbf{T}^{-1} \tag{5.18d}$$

where $\mathbf{T}$ and γ are such that diagonalize the product $\mathbf{YZ}$, i.e.

$$\mathbf{T}^{-1}\mathbf{YZT} = \gamma^2 \tag{5.19}$$

Clearly, this solution is general in the sense that the information about the specific excitations and terminations is still missing and must be included in order to fully determine the signals along the line.

5.2.3   Incorporation of the Terminal Conditions

The CPM does not explicitly determine the N voltages and N currents at the line terminations. Therefore, we need $2N$ relations to determine such voltages and currents from the CPM relation. We suppose that the terminal constraints are given in terms of Thévenin or Norton equivalents, which for linear networks always exist (at least one of the two) [114].

In the case in which both the near-end (source) and far-end (load) configurations are given as Thévenin equivalents, we have:

$$\mathbf{V}(z = 0) = \mathbf{V}_S - \mathbf{Z}_S\mathbf{I}(z = 0) \tag{5.20a}$$
$$\mathbf{V}(z = \mathcal{L}) = \mathbf{V}_L + \mathbf{Z}_L\mathbf{I}(z = \mathcal{L}) \tag{5.20b}$$

where the $\mathbf{V}_S$ and $\mathbf{V}_L$ are vectors of size N and contain the effects of the independent voltage and current sources in the near- and far-end termination networks, respectively, while the $N \times N$ matrices $\mathbf{Z}_S$ and $\mathbf{Z}_L$ contain the effects of the impedances and controlled sources. Given the CPM and the Thévenin representation, the terminal currents can be computed as follows:

$$\mathbf{I}(z = 0) = [\mathbf{\Phi}_{12} - \mathbf{\Phi}_{11}\mathbf{Z}_S - \mathbf{Z}_L\mathbf{\Phi}_{22} + \mathbf{Z}_L\mathbf{\Phi}_{21}\mathbf{Z}_S]^{-1}[\mathbf{V}_L - (\mathbf{\Phi}_{11} - \mathbf{Z}_L\mathbf{\Phi}_{21})\mathbf{V}_S] \tag{5.21a}$$
$$\mathbf{I}(z = \mathcal{L}) = \mathbf{\Phi}_{21}\mathbf{V}_S + (\mathbf{\Phi}_{22} - \mathbf{\Phi}_{21}\mathbf{Z}_S)\mathbf{I}(z = 0) \tag{5.21b}$$

whereas the terminal voltages are obtained from (5.20).

When Norton representations are used, the terminal conditions are expressed as:

$$\mathbf{I}(z = 0) = \mathbf{I}_S - \mathbf{Y}_S\mathbf{V}(z = 0) \tag{5.22a}$$
$$\mathbf{I}(z = \mathcal{L}) = -\mathbf{I}_L + \mathbf{Y}_L\mathbf{V}(z = \mathcal{L}) \tag{5.22b}$$

where, with respect to (5.20), equivalent current sources $\mathbf{I}_{S,L}$ replace the voltage sources and equivalent admittance matrices $\mathbf{Y}_{S,L}$ replace the impedance matrices. With these new definitions, the terminal voltages are given by:

$$\mathbf{V}(z=0) = [\mathbf{\Phi_{21}} - \mathbf{\Phi_{22}}\mathbf{Y_S} - \mathbf{Y}_L\mathbf{\Phi_{11}} + \mathbf{Y}_L\mathbf{\Phi_{12}}\mathbf{Y}_S]^{-1}[-\mathbf{I}_L - (\mathbf{\Phi_{22}} - \mathbf{Y}_L\mathbf{\Phi_{12}})\mathbf{I}_S] \tag{5.23a}$$

$$\mathbf{V}(z=\mathcal{L}) = \mathbf{\Phi_{12}}\mathbf{I}_S + (\mathbf{\Phi_{11}} - \mathbf{\Phi_{12}}\mathbf{Y}_S)\mathbf{V}(z=0) \tag{5.23b}$$

Other ways can be used to relate voltages and currents at the terminals of a N-port linear network, such as mixed representations. For instance, when the near-end constraint is given in terms of a Thévenin equivalent and the far-end termination is described with a Norton equivalent, we have:

$$\mathbf{V}(z=0) = \mathbf{V}_S - \mathbf{Z}_S\mathbf{I}(z=0) \tag{5.24a}$$

$$\mathbf{I}(z=\mathcal{L}) = -\mathbf{I}_L + \mathbf{Y}_L\mathbf{V}(z=\mathcal{L}) \tag{5.24b}$$

The current at the near-end termination and the voltage at the far-end termination are obtainable as:

$$\mathbf{I}(z=0) = [\mathbf{\Phi_{22}} - \mathbf{\Phi_{21}}\mathbf{Z_S} - \mathbf{Y}_L\mathbf{\Phi_{12}} + \mathbf{Y}_L\mathbf{\Phi_{11}}\mathbf{Z}_S]^{-1}[-\mathbf{I}_L - (\mathbf{\Phi_{21}} - \mathbf{Y}_L\mathbf{\Phi_{11}})\mathbf{V}_S] \tag{5.25a}$$

$$\mathbf{V}(z=\mathcal{L}) = \mathbf{\Phi_{11}}\mathbf{V}_S + (\mathbf{\Phi_{12}} - \mathbf{\Phi_{11}}\mathbf{Z}_S)\mathbf{I}(z=0) \tag{5.25b}$$

This last representation is useful when the source contains voltage generators, possibly with zero internal impedance, whereas the loads are better described in terms of admittances, like in the case of open circuits or capacitors.

Clearly, the solution at each frequency is independent from the others. If the behavior at more than one frequency is desired, one simply needs to repeat the computations outlined in this section for every frequency point, starting from the corresponding values of the p.u.l. parameters. Moreover, numerical solution can be easily carried out by means of, e.g., MATLAB, since it only involves standard matrix operations.

5.2.4 Numerical Examples

We consider a single bare wire of radius $r_w = 0.5$ mm, placed at a height $h = 5$ cm above a perfectly-conducting ground plane, as illustrated in Fig. 5.2. According to (5.6a) and (5.7), the p.u.l. inductance and capacitance are

$$L = \frac{\mu_0}{2\pi}\cosh^{-1}\left(\frac{5\times10^{-2}}{5\times10^{-4}}\right) = 1.1 \ \mu\text{H/m}$$

and

$$C = \frac{2\pi\varepsilon_0}{\cosh^{-1}\left(\frac{5\times10^{-2}}{5\times10^{-4}}\right)} = 10.5 \ \text{pF/m}$$

respectively. The surrounding medium is vacuum, with permeability $\mu_0 = 400\pi$ nH/m and permittivity $\varepsilon_0 = 8.854$ pF/m. Vacuum can be regarded to be lossless, thus the the p.u.l. conductance is $G = 0$ and the p.u.l. capacitance is frequency-independent. Moreover, in contrast to on-board structures, for these wire structures the effect of conductor losses is usually negligible, i.e. it can be assumed $R = 0$ and a frequency-independent L as well. The wire is $\mathcal{L} = 100$-cm long and is
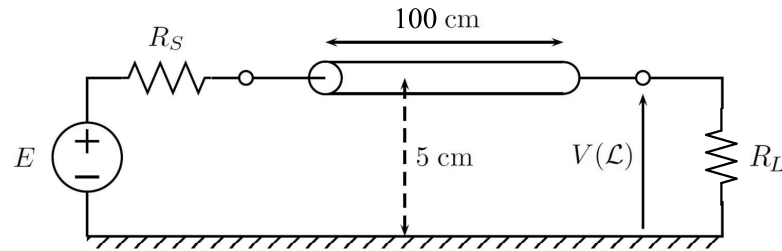

Figure 5.2.   Transmission line consisting of a single wire above a ground plane, driven by a voltage source and terminated by a 1 kΩ resistor.

driven at the near-end side by a voltage source of amplitude $E = 1$ V (constant with frequency) and with an internal impedance of $R_S = 50$ Ω, whereas the far-end side is terminated by a resistor of $R_L = 1$ kΩ. The terminal conditions can be expressed by a mixed representation having the following parameters:

$$V_S = E, \qquad Z_S = R_S$$
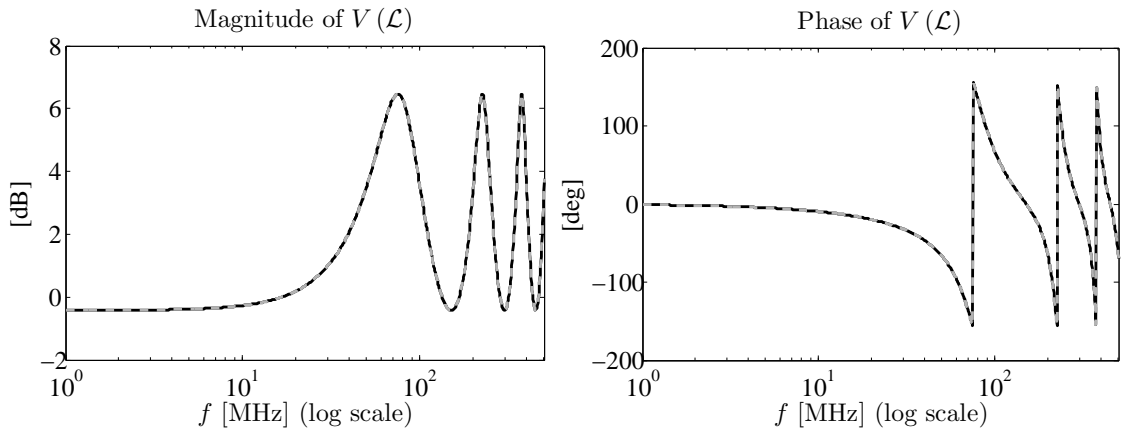$$I_L = 0, \qquad Y_L = 1/R_L$$

(5.26)

Figure 5.3.   Magnitude (left panel) and phase (right panel) of the far-end transmitted voltage.

Figure 5.3 shows the magnitude and phase of the voltage transmitted to the far-end termination, i.e. $V(z = \mathcal{L})$, computed at 1000 frequency points from 1 MHz to 500 MHz. The black line has been computed with the lossless assumption, whereas the dashed gray line is obtained by including

losses according to (5.9) and (5.12), considering a wire conductivity of 58 MS/m (copper). The perfect agreement between the two curves justifies the neglect of losses.
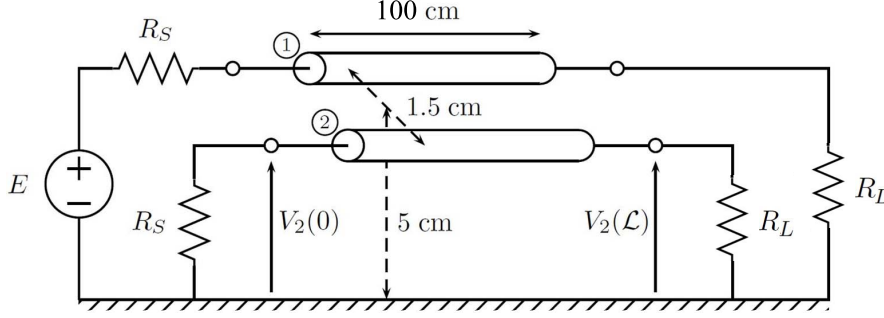

Figure 5.4.   Multiconductor transmission line consisting of two coupled wires above a ground plane. One wire is active and driven by a voltage source.

We consider next the coupled line depicted in Fig. 5.4. The wire radius and height above ground are again $r_{w1} = r_{w2} = 0.5$ mm and $h_1 = h_2 = 5$ cm, respectively, while their separation is $d = 1.5$ cm. We now have the following p.u.l. inductance and capacitance matrices:

$$\mathbf{L} = \begin{bmatrix} 1059.7 & 381.6 \\ 381.6 & 1059.7 \end{bmatrix} \text{nH/m}$$

and

$$\mathbf{C} = \mu_0 \varepsilon_0 \mathbf{L}^{-1} = \begin{bmatrix} 12.06 & -4.35 \\ -4.35 & 12.06 \end{bmatrix} \text{pF/m}$$

The source-line-load configuration is also shown in Fig. 5.4, with one active line fed by a voltage generator having an amplitude of $V_S = E = 1$ V, constant with frequency, and a quiet line terminated by a 50-Ω impedance at its near-end. Both conductors are terminated with 1 kΩ resistors at the far-end side. The Thévenin and Norton equivalents of such terminations are:

$$\mathbf{V}_S = \begin{bmatrix} E \\ 0 \end{bmatrix}, \qquad \mathbf{Z}_S = \begin{bmatrix} R_S & 0 \\ 0 & R_S \end{bmatrix}$$

$$\mathbf{I}_L = \begin{bmatrix} 0 \\ 0 \end{bmatrix}, \qquad \mathbf{Y}_L = \begin{bmatrix} 1/R_L & 0 \\ 0 & 1/R_L \end{bmatrix}$$

respectively. Fig. 5.5 shows the magnitudes of the near- and far-end crosstalk voltages, i.e. $V_2(z = 0)$ and $V_2(z = \mathcal{L})$, respectively, computed by considering again a length of $\mathcal{L} = 100$ cm.

5.3   Affine Based Solution of Transmission-Line Equations With the Inclusion of Parameteric Variations

In the previous sections, we have detailed in the deterministic analysis of transmission line structures via solution to the telegrapher's equations. In this section, we will take into account variations
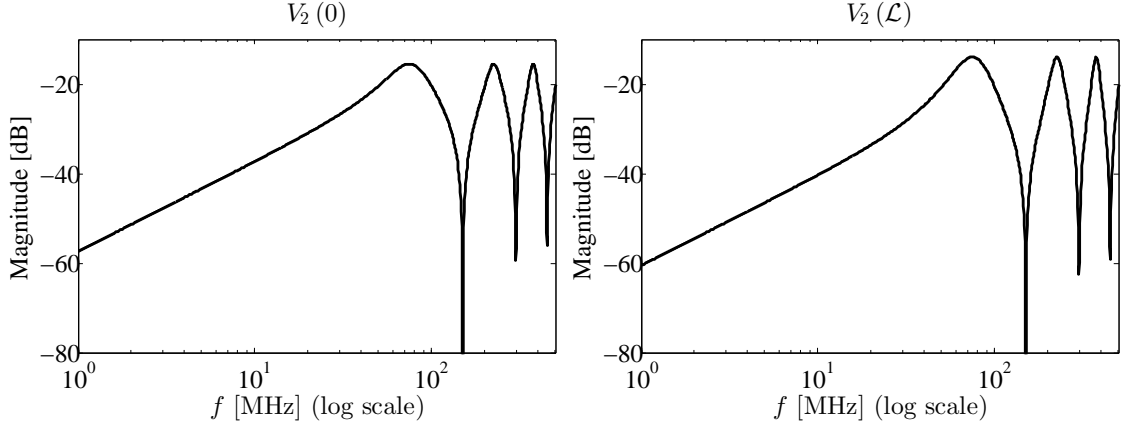
Figure 5.5. Magnitude of the near-end (left panel) and far-end (right panel) crosstalk voltage.

of physical parameters of the lines, and analyze the behavior of frequency-domain responses under effects of variations (bounds of responses), via the proposed affine arithmetic and Monte Carlo (for comparison and validation).

The feasibility and strength of the proposed method will be demonstrated on the worst-case analysis of distributed cables, being its application to the frequency-domain solution of lumped circuits already included in the previous chapters.

5.3.1 Incorporation of Physical Variations in Telegrapher's Equations

We still consider the 2-conductor line structure of Fig. 5.4 that represents a canonical transmission line example with two wires over an ideal ground plane. For simplicity, assume the wires are lossless, and the per-unit-lenght parameters, i.e., the capacitance and inductance matrix, are obtained via numerical calculations and the frequency-domain behavior of the structure is described via the well-known telegrapher's equations:

$$\frac{d}{dz} \left[\begin{array}{c} \mathbf{V}(z,s) \\ \mathbf{I}(z,s) \end{array} \right] = -s \left[\begin{array}{cc} 0 & \mathbf{L} \\ \mathbf{C} & 0 \end{array} \right] \left[\begin{array}{c} \mathbf{V}(z,s) \\ \mathbf{I}(z,s) \end{array} \right] \tag{5.27}$$

where $s = j\omega$ is the Laplace variable, and the vectors collecting the voltage and current variables along the line are $\mathbf{V}(z,s) = [V_1(z,s), V_2(z,s)]^T$ and $\mathbf{I}(z,s) = [I_1(z,s), I_2(z,s)]^T$, and $\mathbf{C}$ and $\mathbf{L}$ are the p.u.l. capacitance and inductance matrices, respectively.

Assume the p.u.l. capacitance and inductance matrices to be interval matrices with $\pm 10\%$ relative variation: $\mathbf{C} = \mathbf{C}_0(1 + 0.1\epsilon_1)$, and $\mathbf{L} = \mathbf{L}_0(1 + 0.1\epsilon_2)$ with $\mathbf{C}_0$ and $\mathbf{L}_0$ being the nominal matrix. The model in (5.27) is then expanded in terms of affine symbols as follows:

$$\frac{d}{dz} \left[\begin{array}{c} \tilde{\mathbf{V}}(z,s) \\ \tilde{\mathbf{I}}(z,s) \end{array} \right] = -s \left(\left[\begin{array}{cc} 0 & \mathbf{L}_0 \\ \mathbf{C}_0 & 0 \end{array} \right] + \left[\begin{array}{cc} 0 & 0 \\ \Delta\mathbf{C} & 0 \end{array} \right] \epsilon_1 + \left[\begin{array}{cc} 0 & \Delta\mathbf{L} \\ 0 & 0 \end{array} \right] \epsilon_2 \right) \left[\begin{array}{c} \tilde{\mathbf{V}}(z,s) \\ \tilde{\mathbf{I}}(z,s) \end{array} \right]$$
$$\tag{5.28}$$

Then we are able to follow the general solution routines introduced in Section 5.2, where all variables inside the equations have become the standard affine form. For instance, the *chain parameter matrix* in (5.16) is reformed as:

$$\tilde{\boldsymbol{\Phi}}(\mathcal{L}) = \text{expm}\left(\begin{bmatrix} \mathbf{0} & -\tilde{\mathbf{Z}} \\ -\tilde{\mathbf{Y}} & \mathbf{0} \end{bmatrix} \mathcal{L} \right) \approx \boldsymbol{\Phi}_0 + \boldsymbol{\Phi}_1 \epsilon_1 + \boldsymbol{\Phi}_2 \epsilon_2 \tag{5.29}$$

where $\tilde{\mathbf{Y}} = j\omega\tilde{\mathbf{C}} = \mathbf{Y}_0 + \mathbf{Y}_1\epsilon_1$, $\tilde{\mathbf{Z}} = j\omega\tilde{\mathbf{L}} = \mathbf{Z}_0 + \mathbf{Z}_1\epsilon_2$, the resulting nominal CPM $\boldsymbol{\Phi}_0$ and coefficient matrices $\boldsymbol{\Phi}_1$, $\boldsymbol{\Phi}_2$ are obtained by means of Pade approximations for interval matrix exponential (See Chapter 2).

In the Fig. 5.4 case, the terminal constraints are given in terms of Thévenin equivalents, thus the terminal currents and voltages are computed as follows in terms of standard affine expression:

$$\tilde{\mathbf{I}}(z = 0) = \left[\tilde{\boldsymbol{\Phi}}_{12} - \tilde{\boldsymbol{\Phi}}_{11}\mathbf{Z}_S - \mathbf{Z}_L\tilde{\boldsymbol{\Phi}}_{22} + \mathbf{Z}_L\tilde{\boldsymbol{\Phi}}_{21}\mathbf{Z}_S \right]^{-1} \left[\mathbf{V}_L - (\tilde{\boldsymbol{\Phi}}_{11} - \mathbf{Z}_L\tilde{\boldsymbol{\Phi}}_{21})\mathbf{V}_S \right]$$
$$\approx \mathbf{I}_0(z = 0) + \mathbf{I}_1(z = 0)\epsilon_1 + \mathbf{I}_2(z = 0)\epsilon_2 \tag{5.30}$$

$$\tilde{\mathbf{I}}(z = \mathcal{L}) = \tilde{\boldsymbol{\Phi}}_{21}\mathbf{V}_S + (\tilde{\boldsymbol{\Phi}}_{22} - \tilde{\boldsymbol{\Phi}}_{21}\mathbf{Z}_S)\tilde{\mathbf{I}}(z = 0)$$
$$\approx \mathbf{I}_0(z = \mathcal{L}) + \mathbf{I}_1(z = \mathcal{L})\epsilon_1 + \mathbf{I}_2(z = \mathcal{L})\epsilon_2 \tag{5.31}$$

$$\tilde{\mathbf{V}}(z = 0) = \mathbf{V}_S - \mathbf{Z}_S\tilde{\mathbf{I}}(z = 0)$$
$$\approx \mathbf{V}_0(z = 0) + \mathbf{V}_1(z = 0)\epsilon_1 + \mathbf{V}_2(z = 0)\epsilon_2 \tag{5.32}$$

$$\tilde{\mathbf{V}}(z = \mathcal{L}) = \mathbf{V}_L + \mathbf{Z}_L\tilde{\mathbf{I}}(z = \mathcal{L})$$
$$\approx \mathbf{V}_0(z = \mathcal{L}) + \mathbf{V}_1(z = \mathcal{L})\epsilon_1 + \mathbf{V}_2(z = \mathcal{L})\epsilon_2 \tag{5.33}$$

It is worth noticing that the internal matrices operations inside (5.30)–(5.33) are based on the "error-spreading" approach of non-affine operations (See Chapter 2 - (2.30)), thus generating no extra noise symbols in this computation chain. The upper and lower bounds of magnitude of terminal currents and voltages can be furthur calculated according to the rules in (2.36) and (2.37).

5.3.2 Numerical Example

In this section, we consider a validation test strucutre, where the location of each wire depicted in Fig. 5.4 is defined by a pair of independent random variables (the wire heights $h_{1,2}$ above the ground plane and the wire radius $r_{1,2}$), thus leading to a problem that involves a total of four random variables (See Fig. 5.6 for the cross-section geometry of the 2-conductor line structure in this validation test).

The wire length is $\mathcal{L} = 1\,\text{m}$ and the source and load impedances are $Z_s = R_s = 50\,\Omega$ and $Z_L = R_L = 1\,\text{k}\Omega$. Line #1 is energized by the voltage source with magnitude of 1 V and line #2
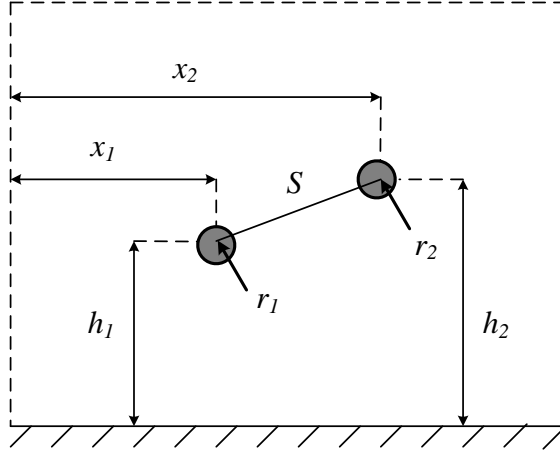
Figure 5.6.   Cross-section of the coupled lines setup. The heights above ground and radius of wires are selected as uncertain parameters

is kept quiet. The nominal values of physical parameters of each line are: $h_1 = 2\,\text{cm}$, $h_2 = 3\,\text{cm}$. $r_{w1} = 0.5\,\text{mm}$, $r_{w2} = 0.4\,\text{mm}$, and distance $d = x_2 - x_1 = 1.5\,\text{cm}$. The variability is given by the height and radius of each cable pair, that are all defined by a set of independent uncertain intervals with $10\,\%$ relative variation.

Then we adopted an approximated formula in [112] to the calculation of p.u.l. inductance matrix $\mathbf{L}$:

$$
\begin{aligned}
l_{ii} &= \frac{\mu_0}{2\pi} \ln\left(2h_i/r_i\right) \quad i = 1,2 \\
l_{12} &= \frac{\mu_0}{4\pi} \ln\left(1 + 4\frac{h_1 h_2}{S^2}\right)
\end{aligned}
$$
(5.34)

where S is the separation between the wires, given by

$$
S = \sqrt{(h_1 - h_2)^2 + d^2}
$$

Take into account the variations of all the physical parameters, the affine form of each entry of the p.u.l. matrix $\mathbf{L}$ can be readily obtained as follows (The logarithm operation of affine form intervals are referred to in Section 2.2.2):

$$
l_{11} = \frac{\mu_0}{2\pi} \ln\left(2\frac{h_1(1 + 0.1\epsilon_1)}{r_1(1 + 0.1\epsilon_2)}\right) \approx 0.9 + 0.02\epsilon_1 - 0.02\epsilon_2 \ \mu\text{H/m}
$$

$$
l_{22} = \frac{\mu_0}{2\pi} \ln\left(2\frac{h_2(1 + 0.1\epsilon_3)}{r_2(1 + 0.1\epsilon_4)}\right) \approx 1.1 + 0.02\epsilon_3 - 0.02\epsilon_4 \ \mu\text{H/m}
$$

$$
l_{12} = \frac{\mu_0}{4\pi} \ln\left(1 + 4\frac{h_1(1 + 0.1\epsilon_1)h_2(1 + 0.1\epsilon_3)}{S^2}\right) \approx 0.2 + 0.03\epsilon_1 - 0.015\epsilon_3 \ \mu\text{H/m}
$$

As a result, the affine form values of the p.u.l. matrix $\mathbf{L}$ are as follows:

$$\tilde{\mathbf{L}} = \begin{bmatrix} 0.87 & 0.22 \\ 0.22 & 1.01 \end{bmatrix} + \begin{bmatrix} 0.02 & 0.03 \\ 0.03 & 0 \end{bmatrix} \epsilon_1 + \begin{bmatrix} -0.02 & 0 \\ 0 & 0 \end{bmatrix} \epsilon_2$$
$$+ \begin{bmatrix} 0 & -0.015 \\ -0.015 & 0.02 \end{bmatrix} \epsilon_3 + \begin{bmatrix} 0 & 0 \\ 0 & -0.02 \end{bmatrix} \epsilon_4$$

Then the p.u.l. capacitance matrix is determined by $\tilde{\mathbf{C}} = \mu_0 \epsilon_0 \tilde{\mathbf{L}}^{-1} \approx \mathbf{C}_0 + \mathbf{C}_1 \epsilon_1 + \mathbf{C}_2 \epsilon_2 + \mathbf{C}_3 \epsilon_3 + \mathbf{C}_4 \epsilon_4$, where $\mathbf{C}_i (i = 1, 2, 3, 4)$ are coefficient matrices of noise symbols $\epsilon_{1,2,3,4}$ and can be readily calculated by means of Sherman formula or Talyor expansions for affine form matrix inversion (See Section 2.2.5).

The frequency-domain solution of (5.28) is then carried out following the routines described in (5.29)–(5.33).

Figure 5.7 shows the frequency-domain response of the far-end crosstalk transfer function $H_1(j\omega) = V_2(z = \mathcal{L}, j\omega)/V_1(z = 0, j\omega)$ and near-end crosstalk transfer function $H_2(j\omega) = V_2(z = 0, j\omega)/V_1(z = 0, j\omega)$ up to 500 MHz, computed via the advocated AA and determined by means of 10,000 MC simulations. The solid black lines correspond to the upper and lower bounds obtained from the proposed affine method (with combination of non-uniform partitioning), while the gray lines are samples of MC results. The accuracy and tightness of the bounds predicted by the AA tool confirm the potential of the proposed method, along with a remarkable speed up of $10\times$ (the CPU time for AA and MC are 3 vs. 30 minutes, respectively).

It is also necessary to mention that, in this numerical example, we have used a non-uniform UIP technique with a maximum number of partitions of 16. As has been illustrated before, for complex circuits and for a richer frequency-domain dynamical behavior, improvements like the partitioning technique are in general needed for suitable adjustment. Since in this validation test example, we found some over-estimation when frequency goes up above 100 MHz, the UIP technique is combined in the AA-based computation for frequency ranging from 100 MHz to 500 MHz.

5.3.3 Parametric Shrinking

From the above numerical example, it is not difficult to notice that, some of the physical parameters show up only once in the per-unit-length matrices, but have been involved in the whole computation chain. For instance, the wire radius r_{w1} is only related to the entry l_{11} and has been assigned with this independent random variable ϵ_2, However, the term of ϵ_2 is not correlated with any other entries, of which all entries of coefficient matrix are zero but l_{11}. Hence, we propose to compress the term r_{w1} with h_1, and replace their noise symbols with one new symbol.

This is somehow like a combination of the AA technique with other complementary tools i.e., IA. We first find the interval range of r_{w1} and h_1, which is $r_{w1}^- = [4.5, 5.5] \times 10^{-4}$, and $\bar{h}_1 = [1.8, 2.2] \times 10^{-2}$. The basic operations of IA in (2.7) give that:

$$\bar{l}_{11} = \frac{\mu_0}{2\pi} \ln\left(\bar{h}_1/r_{w1}^-\right) = \frac{\mu_0}{2\pi} \ln\left(\frac{2 \times [1.8, 2.2] \times 10^{-2}}{[4.5, 5.5] \times 10^{-4}}\right) = [0.83, 0.91]$$
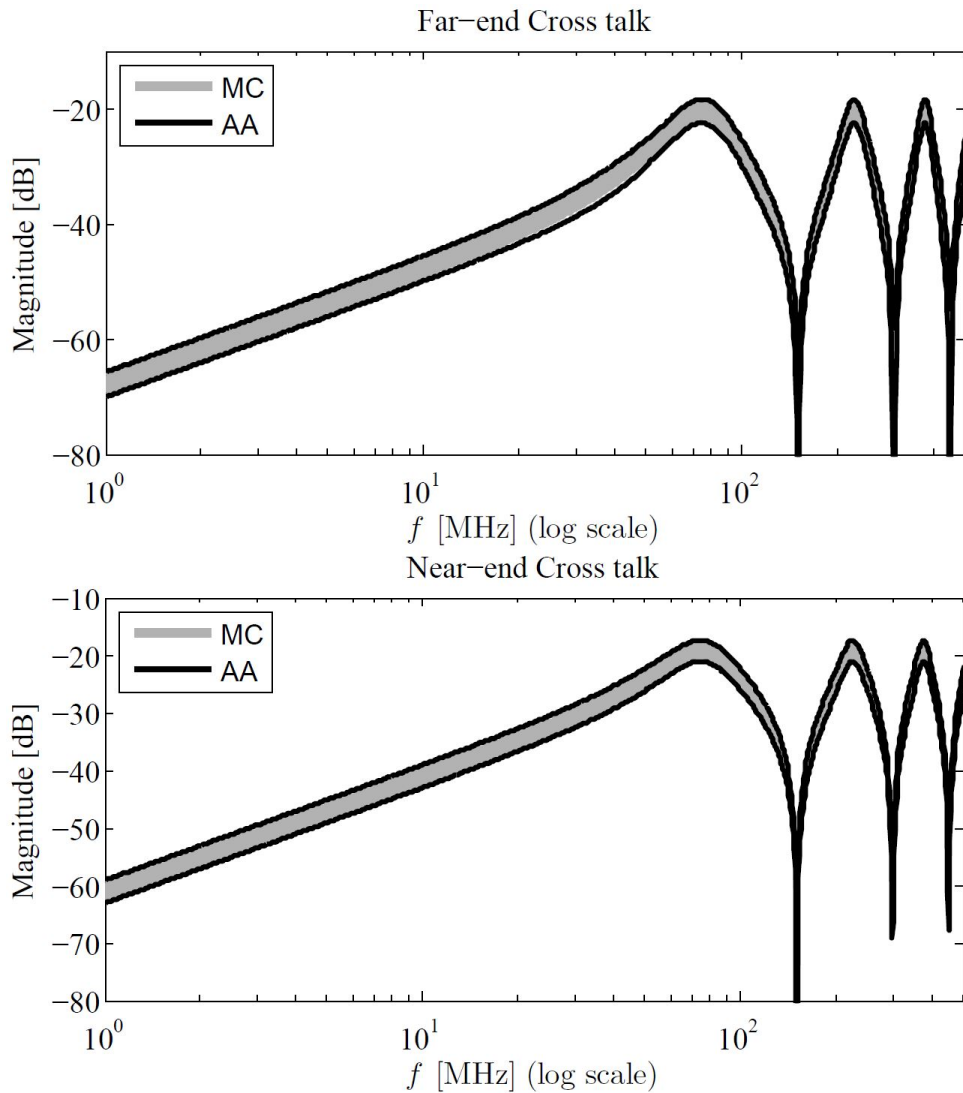
Figure 5.7. Bode plot (magnitude) of the far-end and near-end crosstalk transfer function of the scheme of Fig. 5.6 lines. Gray: MC simulations (10,000 runs), black: AA.

Then the interval of l_{11} can be transformed into the affine form of $\tilde{l}_{11} = 0.87 + 0.04\epsilon_1$. repeat this procedure for all the other entries, and the p.u.l. inductance matrix is represented by two noise symbols only, as follows:

$$\tilde{\mathbf{L}} = \begin{bmatrix} 0.87 & 0.22 \\ 0.22 & 1.01 \end{bmatrix} + \begin{bmatrix} 0.04 & 0.03 \\ 0.03 & 0 \end{bmatrix}\epsilon_1 + \begin{bmatrix} 0 & -0.015 \\ -0.015 & 0.04 \end{bmatrix}\epsilon_2$$

Refer to the same routines for the frequency-domain solution of (5.28), the shrank parameter simulation leads to a speed up of $2\times$. Also, less partitions (4) are required in the high frequency

ranges, leading to more efficient computations.

Figure 5.8 shows the frequency-domain response of the far-end crosstalk transfer function computed via the "shrank parameters" AA and determined by means of 10,000 MC simulations. The solid black lines correspond to the upper and lower bounds obtained from the proposed affine method (with shrank parameters), while the gray lines are samples of MC results. Still, the closeness between the inner (via MC) and outer (via AA) bounds verifies the accuracy of the proposed method and corresponding improvements. Even if we compare the results in Fig. 5.8 with those in Fig. 5.7, and a small over-estimation is observed for the approximation of the lower bound, it is fairly acceptable and worth the sacrifice, especially when considering the speed up.

For complex circuits and systems where there may exist a huge number of independent random variables, this parametric shrinking methodology can be helpful in reducing the system dimension and improving efficiency. However, this tentative idea is just a preliminary step and its use in practical applications should be optimized with corresponding automation algorithms.
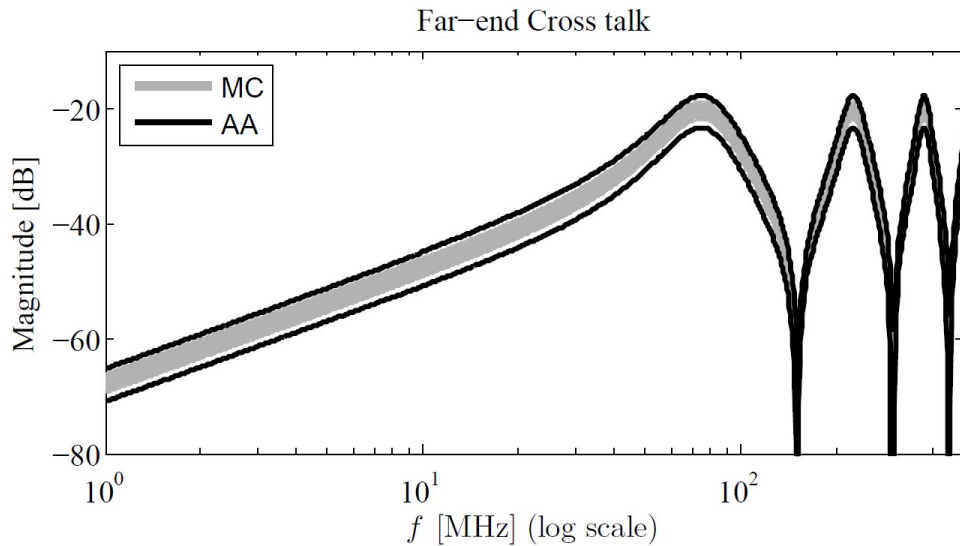

Figure 5.8. Bode plot (magnitude) of the far-end crosstalk transfer function of the scheme of Fig. 5.6 lines with shrank parameters. Gray: MC simulations (10,000 runs), black: AA.

Chapter 6

Applications

In the previous chapters, we have detailed in the fundamental theory of affine arithmetic, along with some basic and tutorial examples of the application of AA to the worst-case analysis of lumped circuits and MTLs in both time-domain and frequency-domain. In this chapter, more realistic and meaningful application examples are provided, in which the proposed method is applied to the analysis of microstrip line, as well as switching power converter. Also, time-domain computations are presented, based on Fourier analysis.

6.1 Example #1 — Flex Cable

As a proof of the capabilities of the proposed technique in dealing with multi-random parameters, the analysis of the more realistic test structure depicted in Fig. 6.1 is presented.
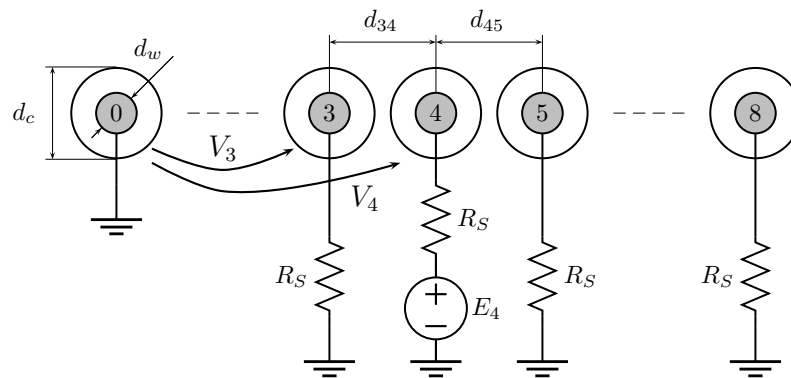

Figure 6.1.   Application test structure: $1\,\mathrm{m}$ long commercial flex cable (9-wire configuration), $R_S = 50\,\Omega$.

The structure represents a Flex Life Cable in a standard 9-wire configuration. Fig. 6.1 collects both the key parameters defining the geometry of the wires as well as the information on the two-terminal circuit elements connected at the near-end of the cable. The cable length is $1\,\mathrm{m}$ and the

far-end terminations are defined by identical resistive elements ($R_L = 1\,\mathrm{k}\Omega$) connecting the wires #1,…,#8 to the reference wire #0.

In this example, the goal is to estimate the response variability of the far-end crosstalk between two adjacent wires in a bundle of many wires. As highlighted in Fig. 6.1, line #4 is energized by the voltage source E_4 and the other lines are quiet and kept in the low state via the R_S resistors. The nominal values of the remaining parameters are: $h_1 = h_3 = h_4 = 2\,\mathrm{cm}$, $h_2 = h_5 = 3\,\mathrm{cm}$. $d_{w1} = d_{w3} = d_{w4} = 1\,\mathrm{mm}$, $d_{w2} = d_{w5} = 0.8\,\mathrm{mm}$, and distance $d = 1.5\,\mathrm{cm}$. The variability is given by the height, radius, and distances between each cable pair, that are all defined by a set of independent uncertain intervals with $10\,\%$ relative variation. The total number of uncertain parameters is 24.
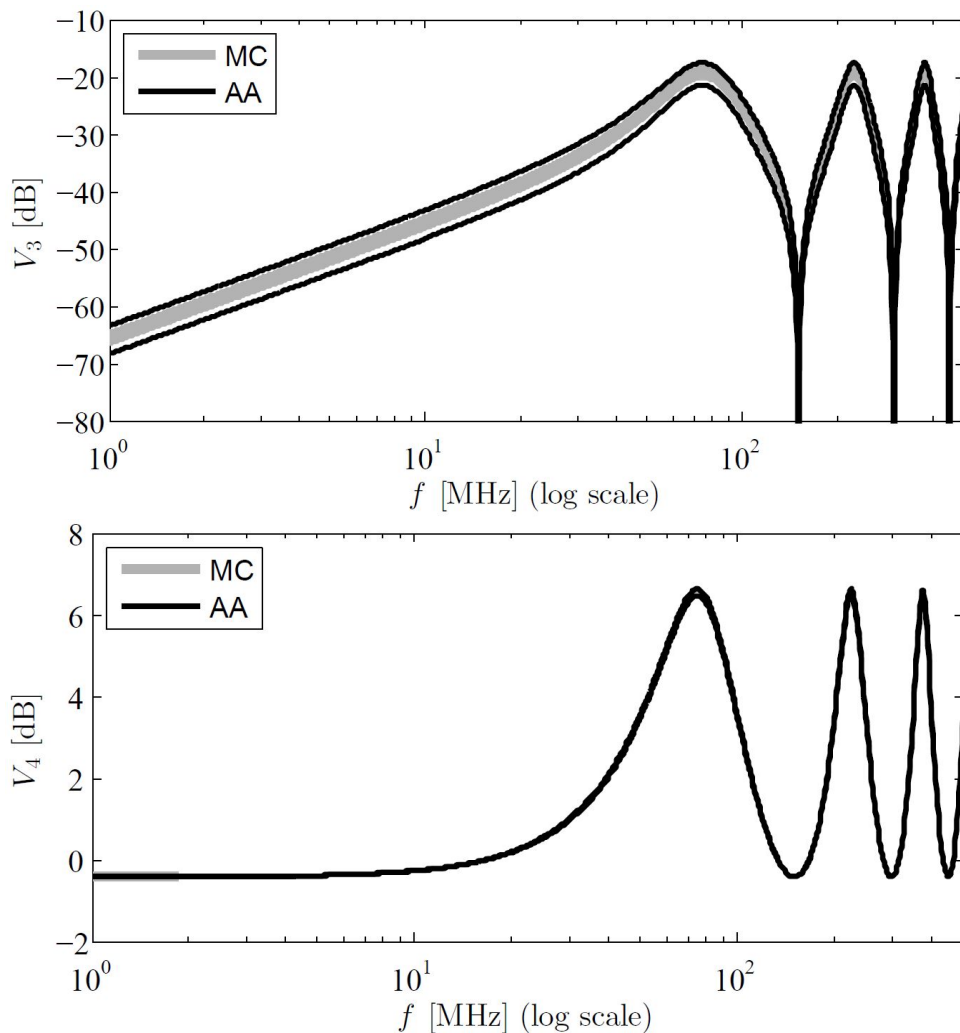

Figure 6.2.   Bode plot (magnitude) of the far-end crosstalk voltage (top panel) and transmitted voltage (bottom panel) of the scheme of Fig. 6.1 lines with shrank parameters. Gray: MC simulations (10,000 runs), black: AA.

Figure 6.2 shows the bounds of the magnitude of the far-end crosstalk transfer function at line #2 and #3, and the far-end voltage of line #4, predicted by means of the AA and via a large number of MC simulations, thus highlighting also for this validation example the effectiveness of the proposed approach. What is more important, even if the total number of parameters is much larger than in the previous case, AA is still 10 times faster than MC (4 min vs. 46 min).

6.2   Example #2 — Microstrip Line

In this section, the proposed technique is applied to the analysis of the coupled microstrip strucuture of Fig. 6.3.
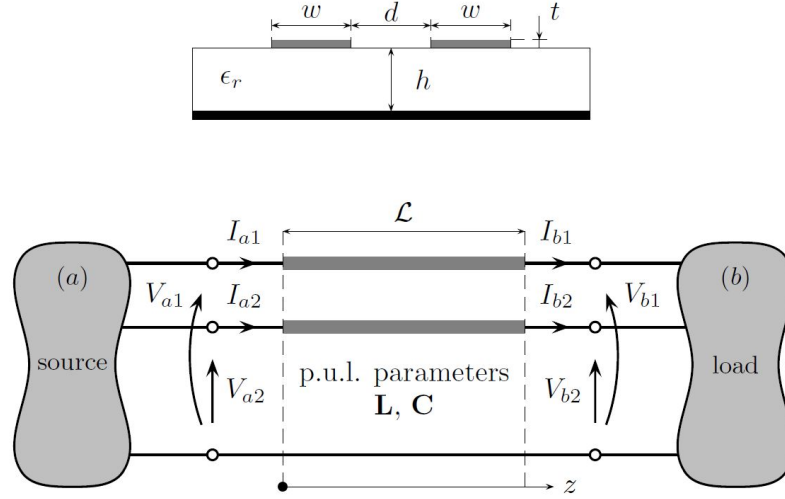

Figure 6.3.   Microstrip structure. Top panel: cross-section; bottom panel: simulation test case.

The top panel shows the cross-section of a microstrip line with two coupled traces. This is a common configuration for on-board lines, and the physical parameters take the following values: $w = 100\,\mu\mathrm{m}$, $h = 500\,\mu\mathrm{m}$, $d = 80\,\mu\mathrm{m}$, $t = 35\,\mu\mathrm{m}$, and the length of conductor $\mathcal{L} = 5\,\mathrm{cm}$. The source and load elements are both defined as resistors with the following values:

$$\mathbf{Z}_S = \left[\begin{array}{cc} R_S & 0 \\ 0 & R_S \end{array} \right], \qquad \mathbf{Z}_L = \left[\begin{array}{cc} R_L & 0 \\ 0 & R_L \end{array} \right]$$

being $R_S = 50\,\Omega$, $R_L = 1\,\mathrm{k}\Omega$.

Also, one line is active and the other is quiet and kept in the low state by R_S. The nominal values of the per-unit-length parameters, i.e., the capacitance and inductance matrix, are calculated via numerical approaches as:

$$\mathbf{L}_0 = \left[\begin{array}{cc} 670 & 360 \\ 360 & 670 \end{array} \right] \mathrm{nH/m}, \quad \mathbf{C}_0 = \left[\begin{array}{cc} 56 & -26 \\ -26 & 56 \end{array} \right] \mathrm{pF/m}$$

The variability is provided by the relative permittivity ϵ_r and the trace separation d. For the sake of simplicity, the discussion is based on a lossless multiconductor line, and the physical variabilities of ϵ_r and d eventually lead to a $\pm 10\,\%$ relative variation of the $\mathbf{C}$ matrix: $\mathbf{C} = \mathbf{C}_0(1 + 0.1\epsilon_1)$.

Figure 6.4 collects the results of a worst-case simulation of this structure, in which one conductor is excited by 1-V source. Cross-talk transfer function at the far-end of the neighboring line via AA and MC is given. Again, the statistical information obtained via MC simulations (gray lines) is compared with the approximations given by the AA technique. Like in the previous examples, the speed up of the proposed method is still $10\times$.
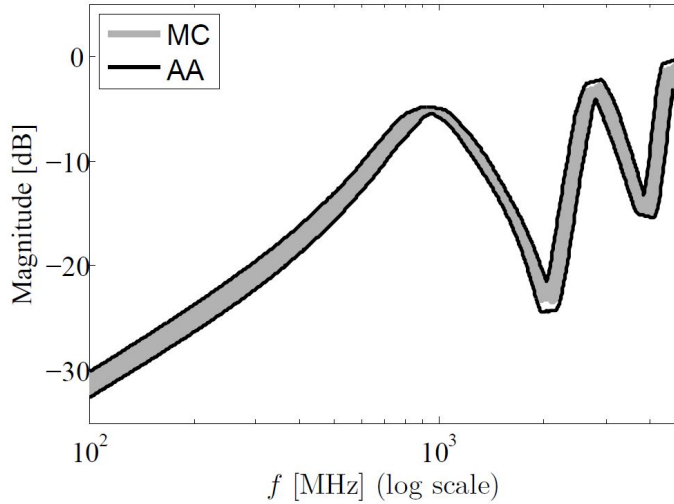

Figure 6.4.   Bode plot (magnitude) of the far-end cross talk transfer function $H(j\omega)$ of the microstrip structure with the inclusion of uncertainties for the p.u.l. capacitance matrix $\mathbf{C}$. Gray: MC simulations (10,000 runs), black: AA.

We next include more realistic variations into the microstrip line structure of Section 6.2, where the load and source impedance are referred to a temperature of $T_{ref} = 25°\text{C}$. In order to analyze the effects of possible fluctuations in the operating temperature, we consider an uniform temperature variation, and assume the load or source impedance are affected by $\pm 5\,\%$ relative variation.

We conducted then, three simulation setups to observe the effects of variations on behavior of frequency responses (See Table 6.1).

Table 6.1.   Simulation setup.

	Variabilities	Partitions (1 kΩ load)	CPU time	Partitions (50 Ω load)	CPU time
#1	$\mathbf{C}$, R_L	8	7 min	4	3 min
#2	$\mathbf{C}$, R_L	4	3 min	4	3 min
#3	$\mathbf{C}$, R_L, R_S	16	10 min	8	5 min

In the first test group, suppose load impedance R_L is affected by the temperature variations and has a $\pm 5\,\%$ relative variation. In case a, the nominal value of the load is $R_{L0} = 1\,\mathrm{k}\Omega$, while in case b, suppose $R_{L0} = 50\,\Omega$. Fig. 6.5 shows magnitude of the far-end cross talk transfer function $H(j\omega)$ for simulation setup case a and b, via 10,000 MC simulations and AA combining non-uniform partitions, while Fig. 6.6 illustrates similar responses for the setup case c and d, where the variability is provided by $\mathbf{C}$ and R_S. At last, in case e and f, we have assumed both source and load terminals R_S, R_L as interval values, and the magnitude of cross talk voltages are plotted in Fig. 6.7, where the frequency-domain behavior exhibits a larger variation range.
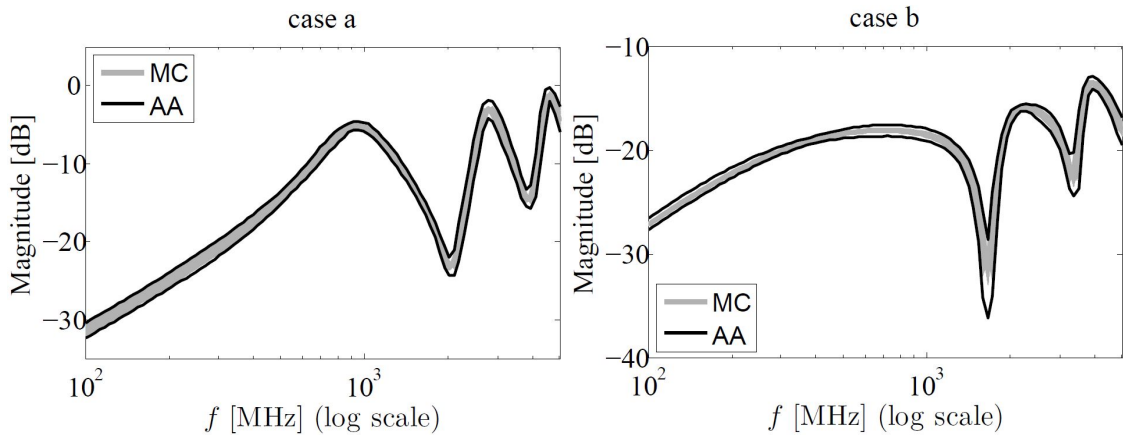

Figure 6.5.   Bode plot (magnitude) of the far-end cross talk transfer function $H(j\omega)$ of the microstrip structure with the inclusion of uncertainties for both $\mathbf{C}$ and R_L. case a: the nominal value of R_L is $R_{L0} = 1\,\mathrm{k}\Omega$; case b: $R_{L0} = 50\,\Omega$. Gray: MC simulations (10,000 runs), black: AA.

Figure 6.6.   Bode plot (magnitude) of the far-end cross talk transfer function $H(j\omega)$ of the microstrip structure with the inclusion of uncertainties for both $\mathbf{C}$ and R_S. case c: the conductors are terminated by $R_L = 1\,\mathrm{k}\Omega$ resistors; case d: $R_L = 50\,\Omega$. Gray: MC simulations (10,000 runs), black: AA.
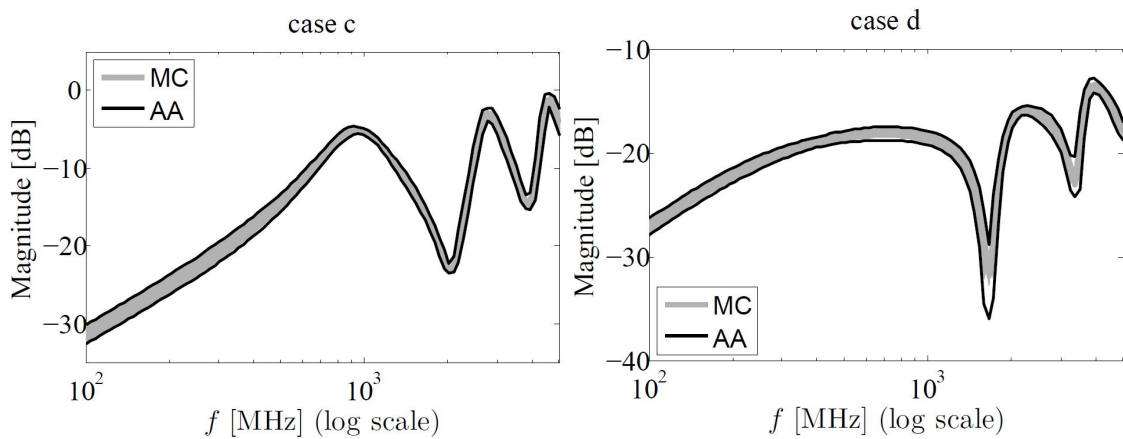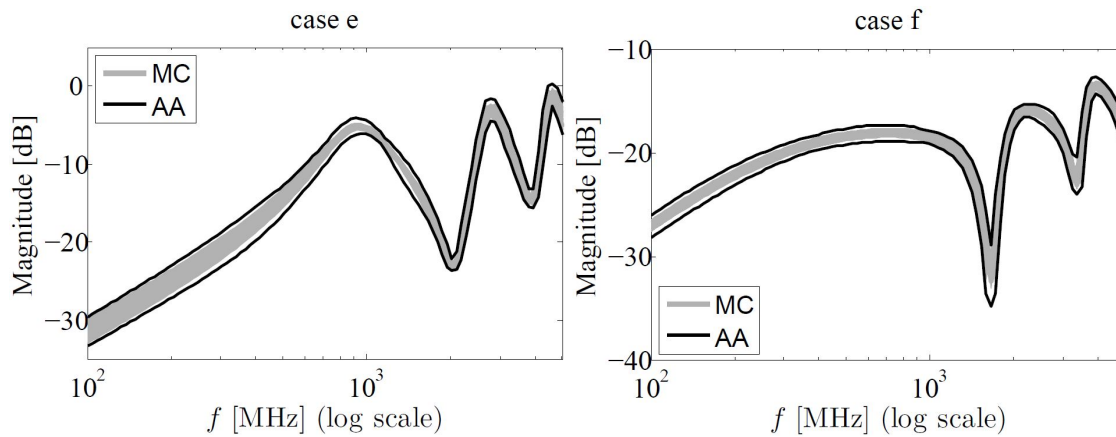
Figure 6.7.   Bode plot (magnitude) of the far-end cross talk transfer function $H(j\omega)$ of the microstrip structure with the inclusion of uncertainties for both C, Z_S and Z_L. case e: the nominal value of R_L is $R_{L0} = 1\,\text{k}\Omega$; case f: $R_{L0} = 50\,\Omega$. Gray: MC simulations (10,000 runs), black: AA.

It is also necessary to mention that, non-uniform partitions are required for the accuracy of AA approximations, especially when the frequency is over $1\,\text{GHz}$. The maximum number of partitions required is 16, as in the setup case e. Apparently, the simulation group #3 takes up more CPU time, especially when the coupled conductors are terminated by $1\,\text{k}\Omega$ resistors. This is because the absolute variation is relatively large and more partitioning work needs to be fulfilled. However, the AA method still realized a speed up of at least $5\times$ compared with MC (of which the least simulation time needed for 10,000 runs is 40 min).

6.3   Example #3 — Switching Power Converter

The last application example collected in this paper is shown in Fig. 6.8. It is a standard dc-dc switching converter in the boost configuration, where design parameters such as L, C and R are assumed varying with a large $\pm 50\,\%$ relative variation and are defined by means of three independent interval values.
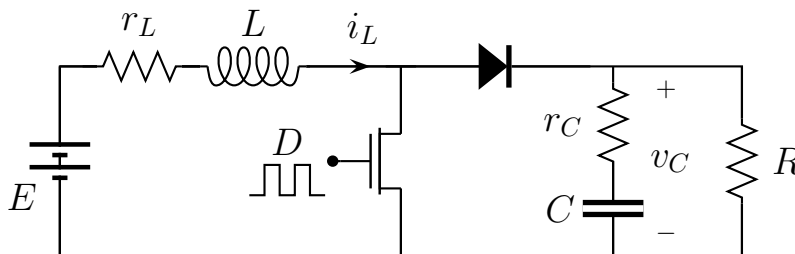

Figure 6.8.   DC-DC boost converter with its relevant electrical variables. The circuit elements take the following values: $E = 20\,\text{V}$, $r_L = 1\,\text{m}\Omega$, $L = 5\,\text{mH}$, $r_C = 5\,\text{m}\Omega$, $C = 10\,\mu\text{F}$ and $R = 20\,\Omega$. The switching frequency is $f_c = 10\,\text{kHz}$.

The circuit of Fig. 6.8 is simulated in the frequency-domain via the solution of an equivalent augmented circuit generated from circuit inspection and topological rules as suggested in [115] and [116]. The coefficients of the Fourier transform of the steady-state circuit responses (such as the inductor current $i_L(t)$) are obtained via the solution of the aforementioned augmented circuit via standard tools (as the MNA) and matrix inversion.

For instance, the current in Fig. 6.8 is expanded as suggested in [115]:

$$I_L(\omega) = \sum_{n=-N}^{+N} I_{L,n}\delta(\omega - n\omega_c - \omega_0) \tag{6.1}$$

where $\omega_c = 2\pi f_c$ is the switching angular frequency and $I_{L,n}$ are the Fourier coefficients of the n-th harmonic of the current $I_L(\omega)$.

Approximate all the other voltage and current variables in the same way, we obtain an augmented MNA equation which is linear and $2N+1$ times of the original one. For more information on the augmented MNA equation, refer to (8) and (10) in [115].

We now assume the switching frequency f to be varying with a $\pm 50\,\%$ relative variation, and solve the affine-form augmented MNA equation according to the affine operations already discussed in Chapter 2. Fig. 6.9 shows the the upper and the lower bounds of the different harmonics of $i_L(t)$ computed via AA and MC methods, and Fig. 6.10 shows the AA and MC bounds under the condition that both f and R are random parameters.
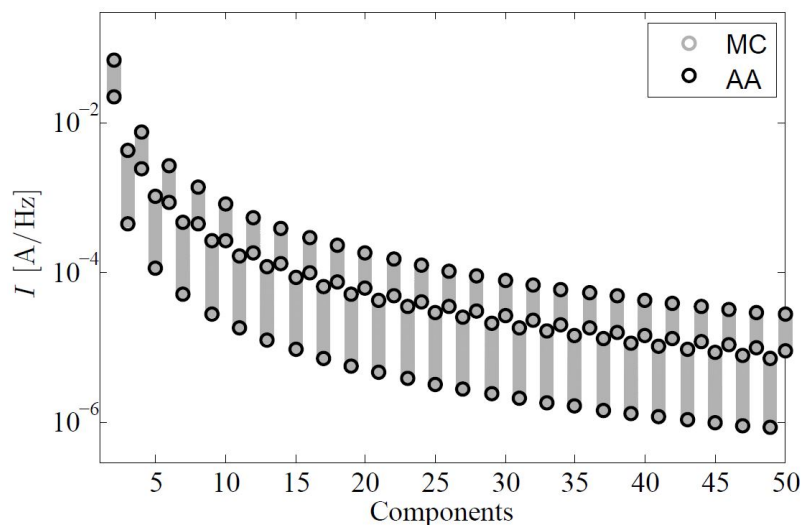

Figure 6.9.   Magnitude of harmonics of the current $i_L(t)$. The variability is given by the switching frequency f. Solid black circles: AA bound; gray: MC method with 10,000 simulations.

In this example, we have considered a sufficiently large number of Fourier expansions ($N = 100$), and the dimension of the augmented matrix is 800. In both situations of Fig. 6.9 and Fig. 6.10, AA has been able to provide a tight upper and lower bound rapidly.

We next consider only the variations of L, C, and R in the augmented MNA equations. The solution to the upper and lower bounds of Fourier coefficients of all current harmonics can be
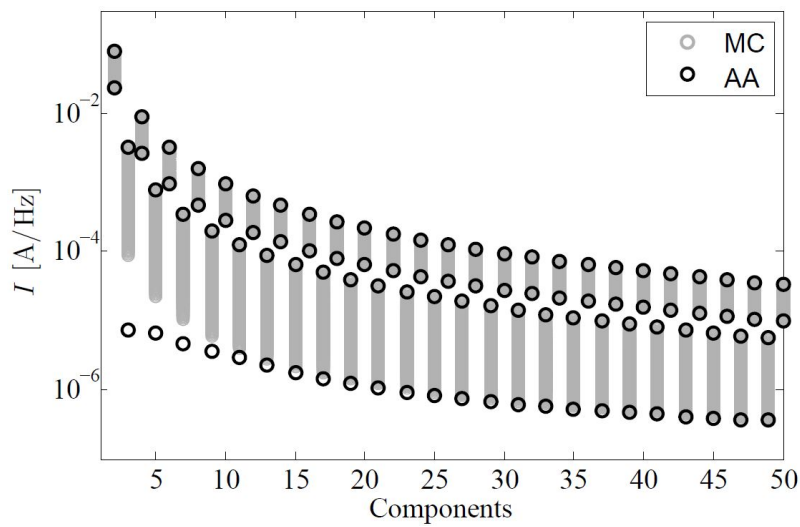
Figure 6.10.   Magnitude of harmonics of the current $i_L(t)$. The variability is given by the switching frequency f and resistor R. Solid black circles: AA bound; gray: MC method with 10,000 simulations.

readily obtained. Fig. 6.11 shows the the upper and the lower bounds of the different harmonics of $i_L(t)$ computed via AA and MC methods. From this comparison, the accuracy of AA is also verified. As far as the efficiency is concerned, AA is 10 times faster than 10,000 MC (4 min vs. 50 min).
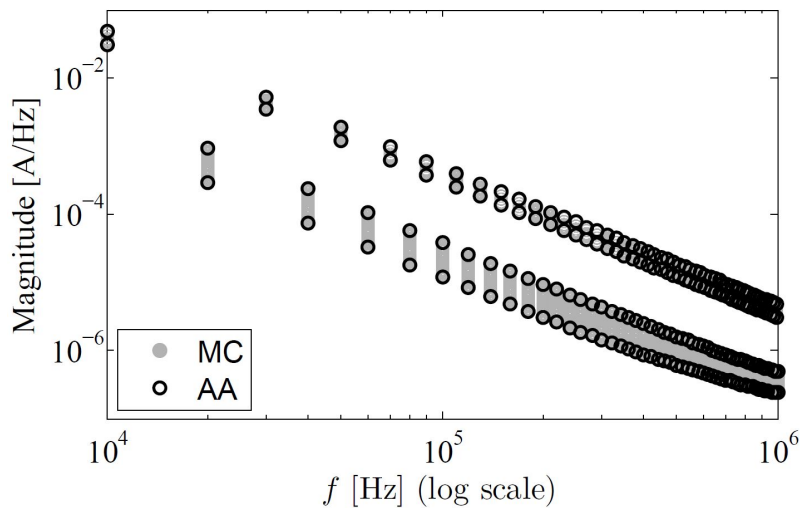

Figure 6.11.   Frequency spectrum of the current $i_L(t)$. Solid black circles: AA bound; gray: MC method with 10,000 simulations.

Since we have detailed in application of AA to frequency-domain analysis in this paper, we are

going one step further, to obtain time-domain (worst-case) response from the frequency-domain computation.

It is relevant to remark that the steady-state time-domain current response of the inductor current (and of all the other variables) can be obtained via post processing of the corresponding frequency-domain spectra. For this very example, where we have obtained the bounds of Fourier coefficients of all current harmonics, deonte $I_{L,n}^{max}$ and $I_{L,n}^{min}$ as the upper and lower bounds of magnitude of n-th harmonic of $I_L(\omega)$, respectively, then the bounds of current response in time domain can be obtained as follows:

$$I_L^*(t) = \sum_{n=-N}^{+N} I_{L,n}^* e^{j(n\omega_c + \omega_0)t} \tag{6.2}$$

where $*$ denotes max or min. It is obvious that we need only two computations to get the time-domain bounds, while with MC, the number of runs is at least 10,000 (See Fig. 6.12), namely, this AA computation can be $10000 \div 2 = 5000$ times faster.
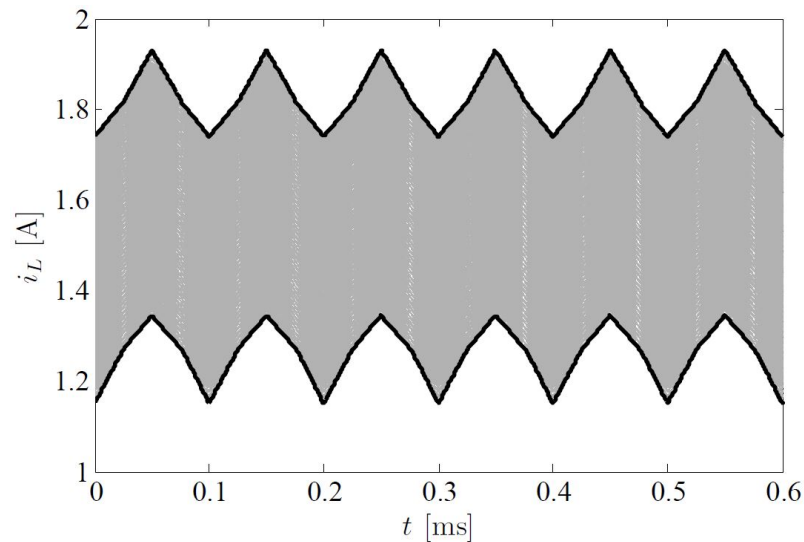

Figure 6.12.   Time-domain responses of the current $i_L(t)$. Solid black lines: AA bound; gray lines: MC method with 10,000 simulations.

Conclusions

Motivated by ever-increasing impact of uncertainties in electrical and electronic products, this thesis presents an efficient interval-valued modeling strategy for circuit and high-speed links. The high-speed links are typically affected by variability in their physical parameters. The objective of this thesis is to estimate the response fluctuation and set realistic design margins.

The technique is based on the so-called affine arithmetic. In order to improving the accuracy of interval operations, the affine arithmetic represents random variable by a center-radius formed interval number consisting of a central value and several noise symbols (the coefficient of which represents magnitude of the "radius"), and correlates relevant quantities by assigning them with the same noise symbol. A main limitation with the technique is the computational complexity, especially when an application has numerous uncertain quantities or involves many steps of computations. The affine-based range analysis can generate a vast number of noise symbols, and becomes a large computational burden to be carried around. This problem can be solved by spreading the effect of the new generated noise symbols among all other uncertainty terms, thus avoiding the growth of complexities of the computation algorithm. This idea has been fulfilled within a modified simulation framework which we developed for the true worst-case circuit analysis.

Classical tools for circuit analysis, such as modified nodal analysis (MNA), are utilized within this affine framework accounting for both real and complex algebra. The original contribution of this work is the extension of the existing affine arithmetic-based techniques to distributed interconnects in both time- and frequency-domain using transmission-line elements described by telegraphers equations. The arithmetic-based techniques had been previously applied to the time-domain analysis of lumped circuits. Numerical approximation techniques such as the Sherman-Morrison method have been combined within the affine framework for accurate and fast matrix operations. To further improve the accuracy, we have leveraged on the partitioning technique, where the tolerance intervals of parameters are divided in subintervals and the union of the objective function range are computed over all the combinations.

As far as the computational time is concerned, the proposed methodology provides a more efficient alternative as compared with the traditional sampling-based methods such as Monte Carlo, with excellent agreement on the accuracy. A large number of application examples are presented, showing the feasibility, flexibility and strength of the advocated approach.

Finally, a different application scenario, where the variability of a power converter is induced by the periodically switched frequency, is successfully addressed via the AA approach and the augmented MNA technique [115]. In this case, the transient solution of a super large variational matrix (obtained from augmentation of Fourier expansions of parameters) via the proposed method outperforms Monte Carlo significantly.

We suggest two future directions based on this work. Firstly, we will model distributed interconnects illuminated by random fields, which is still in its infancy, and random cables, for which, there has been a growing demand for models accounting for random wrapping and twisting of cable bundles. Secondly, we will further optimize the simulation framework in terms of both efficiency and accuracy. Although Ma et al. [99] and Zou et al. [104] proposed the spreading rules for avoiding the generation of extra noise symbols, it is still necessary for us to find a best way, also for complex interval values, to further improve the accuracy of subsequent computations.

Bibliography

[1] A. Ajayi, P. Ingrey, P. Sewell, and C. Christopoulos, "Direct computation of statistical variations in electromagnetic problems," *IEEE Trans. EMC*, vol. 50, no. 2, pp. 325–332, May 2008.

[2] C. Chiang and J. Kawa, *Design for Manufacturability and Yield for Nano-Scale CMOS*. New York: Springer-Verlag, 2007.

[3] M. Orshansky, S. Nassif, and D. Boning, *Design for Manufacturability and Statistical Design: A Constructive Approach*. New York: Springer-Verlag, 2010.

[4] S. Natarajan, M. A. Breuer, and S. K. Gupta, "Process variations and their impact on circuit operation," in *Proceedings of the 1998 IEEE International Symposium on Defect and Fault Tolerance in VLSI Systems*, Nov. 1998, pp. 73–81.

[5] S. Nassif, "Design for variability in DSM technologies," in *Proceedings of the 1st IEEE International Symposium on Quality Electronic Design*, San Jose, CA, Mar. 2000, pp. 451–454.

[6] D. Boning and S. Nassif, "Models of process variations in device and interconnect," in *Design of High Performance Microprocessor Circuits*, A. Chandrakasan, W. J. Bowhill, and F. Fox, Eds. New York: Wiley, 2001.

[7] T. Kang, Y. Chung, S. Won, and H. Kim, "On the uncertainty in the current waveform measurement of an ESD generator", *IEEE Transactions on Electromagnetic Compatibility*, vol. 42, no. 4, pp. 405–413, Nov. 2000.

[8] E. Garcia, "Electromagnetic compatibility uncertainty, risk, and margin management," *IEEE Transactions on Electromagnetic Compatibility*, vol. 52, no. 1, pp. 3–10, Feb. 2010.

[9] J. L. Ramos and J. A. M. Saldana, "Uncertainty models for switch-mode dc-dc converters", *IEEE Transactions on Circuits and Systems–Part I: Fundamental Theory and Applications*, vol. 47, no. 2, pp.200–203, Feb. 2000.

[10] D. V. Ginste, D. D. Zutter, D. Deschrijver, T. Dhaene, P. Manfredi, and F. Canavero, "Stochastic modeling-based variability analysis of on-chip interconnects", *IEEE Transactions on Components, Packaging and Manufacturing Technology*, vol. 2, no. 7, pp.1182–1192, Jul. 2012.

[11] P. Manfredi, *High-speed interconnect models with stochastic parameter variability*, PhD thesis, Politecnico di Torino, May, 2013.

[12] V. Mehrotra, *Modeling the effects of systematic process variation on circuit performance*, PhD thesis, Massachusetts institute of technology, May 2001.

[13] V. Venkatraman and W. Burleson, "Impact of process variations on multi-level signaling for on-chip interconnects," in *Proceedings of the 18th IEEE International Conference on VLSI Design*, 2005, pp. 362–367.

[14] S. Borkar, T. Karnik, S. Narendra, J. Tschanz, A. Keshavarzi, and V. De, "Parameter variations and impact on circuits and microarchitecture," in *Proceedings of the 40th Annual Design Automation Conference*, New York, NY, 2003, pp. 338–342.

[15] Y. Massoud and A. Nieuwoudt, "Modeling and design challenges and solutions for carbon nanotube-based interconnect in future high performance integrated circuits," *ACM Journal on Emerging Technologies in Computing Systems*, vol. 2, no. 3, pp. 155–196, Jul. 2006.

[16] A. Nieuwoudt and Y. Massoud, "On the impact of process variations for carbon nanotube bundles for VLSI interconnect," *IEEE Transactions on Electron Devices*, vol. 54, no. 3, pp. 446–455, Mar. 2007.

[17] A. Nieuwoudt and Y. Massoud, "On the optimal design, performance, and reliability of future carbon nanotube-based interconnect solutions," *IEEE Transactions on Electron Devices*, vol. 55, no. 8, pp. 2097–2110, Aug. 2008.

[18] U.S. Department of Transportation, Federal Aviation Administration, *Aircraft Wiring Degradation Study*, Jan. 2008.

[19] J. Gu, and M. Pecht, "Prognostics and health management using physics-of-failure," *Reliability and Maintainability Symposium*, 2008. RAMS 2008, pp. 481–487.

[20] Flight Safety Foundation Editorial Staff, *Aircraft Wiring Incidents Persist In Aging Systems*, *Avionics News*, Mar. 2005.

[21] C. Furse and R. Haupt, "Down to the wire," *IEEE Spectrum*, pp. 35–39, Feb. 2001.

[22] C. Furse, "Finding fault: locating hidden hazards on aircraft wiring," Utah: University of Utah, Feb. 2004.

[23] A. Dasgupta, and M. Pecht, "Material failure mechanisms and damage models," *IEEE Transactions on Reliability*, vol. 40, no. 5, pp. 531–536, Dec. 1991.

[24] M. Dhakshnamoorthy, S. Vikram and R. Vasanthakumari, "Development of flexible low dielectric constant polyimide films based on iso-propylidene, aryl-ether linked dianhydride/diamine," *International Journal of Scientific & Engineering Research*, vol. 3, no. 8, Aug. 2012.

[25] F. J. Campbell, "Temperature dependence of hydrolysis of polyimide wire insulation," *IEEE Transactions on Electrical Insulation*, vol. EI-20, no. 1, pp. 111–116, Feb. 1985.

[26] L. Li, N. Bowler, M. R. Kessler, and S. H. Yoon, "Dielectric response of PTFE and ETFE wiring insulation to thermal exposure," *IEEE Transactions on Dielectrics and Electrical Insulation*, vol. 17, no. 4, pp. 1234–1241, Aug. 2010.

[27] S. Mamedov, V. Alekperov, N. Can, F. Aras, and G. Yilmaz, "Effects of mechanical and thermal stresses on electric degradation of polyolefins and related materials," *Macromol. Symp. 2004*, pp. 293–298.

[28] S. Diaham, M. L. Locatelli, and T. Lebey, "Improvement of polyimide electrical properties during short-term of thermal aging," *2008 Annual Report Conference on Electrical Insulation Dielectric Phenomena*, pp. 79–83, 2008.

[29] R. Khazaka, M. L. Locatelli, S. Diaham, and P. Bidan, "Endurance of thin insulation polyimide films for high-temperature power module applications," *IEEE Transactions on Components, Packaging and Manufacturing Technology*, vol. 3, no. 5, pp. 811–817, May 2013.

[30] L. Li, *Dielectric properties of aged polymers and nanocomposites*, PhD thesis, Iowa State University, 2011.

[31] E. R. Abram and N. Bowler, "Effect of relative humidity on the curing and dielectric properties of polyurethane-based composites," *2005 Annual Report Conference on Electrical Insulation and Dielectric Phenomena*, pp. 457–460, 2005.

[32] N. Bowler and E. R. Abram, "Monitoring the effect of relative humidity during curing on dielectric properties of composites at microwave frequencies," *Review of Quantitative Nondestructive Evaluation*, vol. 25, pp. 469–476, 2006.

[33] E. McGibney, J. Barrett, J. Barton, L. Floyd, and P. Tassie, "The high frequency electrical properties of interconnects on a flexible polyimide substrate including the effects of humidity," *IEEE Transactions On Components And Packaging Technologies*, vol. 1, no. 1, pp. 4–15, 2011.

[34] I. Radu, M. Acedo, and J. Filippini, "The effect of water treeing on the electric field distribution of XLPE consequences for the dielectric strength," *IEEE Transactions on Dielectrics and Electrical Insulation*, vol. 7 no. 6, pp. 860–868, Dec. 2000.

[35] S. Shiran, B. Reiser, and H. Cory, "A probabilistic model for the evaluation of coupling between transmission lines," *IEEE Transactions on Electromagnetic Compatibility*, vol. 35, no. 3, pp. 387–393, Aug. 1993.

[36] D. Bellan, S. A. Pignari, and G. Spadacini, "Characterisation of crosstalk in terms of mean value and standard deviation," *IEE Proceedings of Science, Measurement and Technology*, vol. 150, no. 6, pp. 289–295, Nov. 2003.

[37] D. Bellan and S. Pignari, "A probabilistic model for the response of an electrically short two-conductor transmission line driven by a random plane wave field," *IEEE Transactions on Electromagnetic Compatibility*, vol. 43, no. 2, pp. 130–139, May 2001.

[38] W. Tian, X. T. Ling, and R. W. Liu, "Novel methods for circuit worst-case tolerance analysis", *IEEE Transactions on Circuits and Systems–I: Fundamental Theory and Application*, vol. 43, no. 4, pp.272–278, Apr. 1996.

[39] S. R. Nassif, A. J. Strojwas, and S. W. Director, "A methodology for worst-case analysis of integrated circuits", *IEEE Transactions on Computer-Aided Design*, vol. CAD-5, no. 1, pp. 104–113, Jan. 1986.

[40] P. Y. Kuo, S. Saibua, G. Huang, and D. Zhou, "An efficient method for evaluating analog circuit performance bounds under process variations", *IEEE Transactions on Circuits and Systems–II: Express Briefs*, vol. 59, no. 6, pp. 351–335, Jun. 2012.

[41] M. Wu, D. G. Beetner, T. H. Hubing, H. Ke, and S. Sun, "Statistical prediction of reasonable worst-case crosstalk in cable bundles," *IEEE Trans. EMC*, vol. 51, no. 3, pp. 842–851, Aug. 2009.

[42] D. G. Beetner, H. Weng, M. Wu, and T. Hubing, "Validation of worst-case and statistical models for an automotive EMC expert system," *in Proc. 2007 IEEE int. Symp. Electromagn. Compat.*, pp. 1–5, Jul. 2007.

[43] M. Tian, and C. J. R. Shi, "Worst case tolerance analysis of linear analog circuits using sensitivity bands," *IEEE Trans. Circuits and Systems I: Fundamental Theory and Applications*, vol. 47, no. 8, pp. 1138–1145, Aug. 2000.

[44] A. Abderrahman, E. Cerny, and B. Kaminska, "Worst case tolerance analysis and clp-based multifrequency test generation for analog circuits", *IEEE Transactions on Computer-Aided Design of Integrated Circuits and Systems*, vol. 18, no. 3, pp. 332–345, Mar. 1999.

[45] W. M. Smith, "Worst case circuit analysis – an overview (electronic parts/circuits tolerance analysis)," in *Proceedings of the Annual Reliability and Maintainability Symposium*, Jan. 1996, pp. 326–334.

[46] C. F. Fang, *Probabilistic interval-valued computation: representing and reasoning about uncertainty in DSP and VLSI design*, PhD thesis, Carnegie Mellon University, April, 2005.

[47] I. A. Starkov, S. E. Tyaginov, O. Triebl, J. Cervenka, C. Jungemann, S. Carniello, J. M. Park, H. Enichlmair, M. Karner, C. Kernstock, E. Seebacher, R. Minixhofer, H. Ceric, and T. Grasser, "Analysis of worst-case hot-carrier conditions for high voltage transistors based on full-band monte-carlo simulations," *17th IEEE International Symposium on the Physical and Failure Analysis of Integrated Circuits (IPFA)*, pp. 1–6, Jul. 2010.

[48] A. H. C. Smith, A. Monti, and F. Ponci, "Uncertainty and worst-case analysis in electrical measurements using polynomial chaos theory," *IEEE Trans. Instrumentation and Measurement*, vol. 58, no. 1, pp. 58–67, Jan. 2009.

[49] B. Mutnury, M. Cases, N. Pham, D. N. Araujo, and E. Matoghi, "Genetic algorithms with scalable IO macromodels to find the worst case corner in high-speed server electrical analysis," *2006 IEEE Electrical Performance of Electronic Packaging*, pp. 73–76, Oct. 2006.

[50] N. Femia, and G. Spagnuolo, "True worst-case circuit tolerance analysis using genetic algorithms and affine arithmetic," *IEEE Trans. Circuits and Systems*, vol. 47, no. 9, pp. 1285–1296, Sep. 2000.

[51] T. Kato, K. Inoue, and K. Nishimae, "Worst-case tolerance analysis for a power electronic system by modified genetic algorithms", *Power Electronics and Motion Control Conference, IPEMC 2006*, pp. 1–5, Aug. 2006.

[52] N. Femia, and G. Spagnuolo, "Genetic optimization of interval arithmetic based worst case circuit tolerance analysis," *IEEE Trans. Circuits and Systems*, vol. 46, no. 12, pp. 1441–1456, Dec. 1999.

[53] S. Skelboe, "True worst-case analysis of linear electrical circuits by interval arithmetic", *IEEE Transactions on Circuits and Systems*, vol. CAS-26, pp. 874–879, Oct. 1979.

[54] L. Kolev, "Worst-case tolerance analysis of linear DC and AC electric circuits," *IEEE Trans. Circuits and Systems I: Fundamental Theory and Applications*, vol. 49, no. 12, pp. 1693–1701, Dec. 2002.

[55] G. S. Fishman, *Monte Carlo: Concepts, Algorithms, and Applications.* New York: Springer-Verlag, 1996.

[56] H. Niederreiter, P. Hellekalek, G. Larcher, and P. Zinterhof, *Monte Carlo and Quasi-Monte Carlo Methods*. New-York: Springer-Verlag, 1998.

[57] H. Kettani, and B. Barmish, "A new monte carlo circuit simulation paradigm with specific results for resistive networks," *IEEE Trans. Circuits and Systems*, vol. 53, no. 6, pp. 1289–1299, Jun. 2006.

[58] Q. J. Zhang and M. Nakhla, "Yield analysis and optimization of VLSI interconnects in multichip modules," in *Proceedings of the IEEE Multi-Chip Module Conference*, 1993, pp. 160–163.

[59] T. Mikazuki and N. Matsui, "Statistical design techniques for high-speed circuit boards with correlated structure distributions," *IEEE Transactions on Components, Packaging and Manufacturing Technology – Part A*, vol. 17, no. 1, pp. 159–165, Mar. 1994.

[60] A. Ciccolella and F. G. Canavero, "Stochastic prediction of wire coupling interference," in *Proceedings of the 1995 IEEE International Symposium on Electromagnetic Compatibility*, Atlanta, GA, Aug. 1995, pp. 51–56.

[61] Y. Cao, P. Gupta, A. B. Kahng, D. Sylvester, and J. Yang, "Design sensitivities to variability: extrapolations and assessments in nanometer VLSI," in *Proceedings of the 15th Annual IEEE International ASIC/SOC Conference*, Rochester, NY, Sep. 2002, pp. 411–415.

[62] P. Manfredi, I. S. Stievano, and F. G. Canavero, "Transient analysis of PCB lines with the inclusion of parameters uncertainties," *2011 IEEE International Symposium on Electromagnetic Compatibility (EMC)*, pp. 146–149, Aug. 2011.

[63] I. S. Stievano, P. Manfredi, and F. G. Canavero, "Impact of parameters variability on the electrical performance of carbon nanotube interconnects," *15th IEEE Workshop on Signal Propagation on Interconnects (SPI)*, pp. 83–86, 2011.

[64] I. S. Stievano, P. Manfredi, and F. G. Canavero, "Parameters variability effects on multiconductor interconnects via Hermite Polynomial Chaos," *IEEE Trans. Components, Packaging and Manufacturing Technology*, vol. 1, no. 8, pp. 1234–1239, Aug. 2011.

[65] I. S. Stievano, P. Manfredi, and F. G. Canavero, "Stochastic analysis of multiconductor cables and interconnects," *IEEE Trans. EMC*, vol. 53, no. 2, pp. 501–507, May 2011.

[66] R. G. Ghanem and P. D. Spanos, *Stochastic Finite Elements. A Spectral Approach*. New York: Springer-Verlag, 1991.

[67] D. Xiu and G. E. Karniadakis, "The Wiener-Askey polynomial chaos for stochastic differential equations," *SIAM Journal on Scientific Computing*, vol. 24, no. 2, pp. 619–644, 2002.

[68] B. J. Debusschere, H. N. Najm, P. P. Pébay, O. M. Knio, R. G. Ghanem, and O. P. Le Maître, "Numerical challenges in the use of polynomial chaos representations for stochastic processes," *SIAM Journal on Scientific Computing*, vol. 26, no. 2, pp. 698–719, 2005.

[69] R. Ghanem, "A stochastic Galerkin expansion for nonlinear random vibration analysis," *Probabilistic Engineering Mechanics*, vol. 8, no. 3-4, pp. 255–264, 1993.

[70] R. Ghanem and W. Brzakala, "Stochastic finite-element analysis of soil layers with random interface," *Journal of Engineering Mechanics*, vol. 122, no. 4, pp. 361–369, Apr. 1996.

[71] D. Xiu and G. E. Karniadakis, "Modeling uncertainty in steady state diffusion problems via generalized polynomial chaos," *Computer Methods in Applied Mechanics and Engineering*, vol. 191, no. 43, pp. 4927–4948, Sep. 2002.

[72] F. S. Hover and M. S. Triantafyllou, "Application of polynomial chaos in stability and control," *Automatica*, vol. 42, no. 5, pp. 789–795, May 2006.

[73] J. Silly-Carette, D. Lautru, M.-F. Wong, A. Gati, J. Wiart, and V. Fouad Hanna, "Variability on the propagation of a plane wave using stochastic collocation methods in a bio electromagnetic application," *IEEE Microwave and Wireless Components Letters*, vol. 19, no. 4, pp. 185–187, Apr. 2009.

[74] O. Aiouaz, D. Lautru, M.-F. Wong, E. Conil, A. Gati, J. Wiart, and V. Fouad Hanna, "Uncertainty analysis of the specific absorption rate induced in a phantom using a stochastic spectral collocation method," *Annals of Telecommunications*, vol. 66, no. 7-8, pp. 409–418, Aug. 2011.

[75] C. Chauvière, J. S. Hesthaven, and L. Lurati, "Computational modeling of uncertainty in time-domain electromagnetics," *SIAM Journal on Scientific Computing*, vol. 28, no. 2, pp. 751–775, 2006.

[76] F. Gong, H. Yu, L. Wang, and L. He, "A parallel and incremental extraction of variational capacitance with stochastic geometric moments," *IEEE Transactions on Very Large Scale Integration (VLSI) Systems*, vol. 20, no. 9, pp. 1729–1737, Sep. 2012.

[77] Q. Su and K. Strunz, "Stochastic circuit modelling with Hermite polynomial chaos," *IET Electronics Letters*, vol. 41, no. 21, pp. 1163–1165, Oct. 2005.

[78] P. Manfredi and F. G. Canavero, "Polynomial Chaos for Random Field Coupling to Transmission Lines," *IEEE Transactions on Electromagnetic Compatibility*, vol. 54, no. 3, pp. 677–680, Jun. 2012.

[79] W. Schoutens, *Stochastic Processes and Orthogonal Polynomials*. New York: Springer-Verlag, 2000.

[80] R. E. Moore, *Interval Analysis*. Englewood Cliffs, NJ: Prentice-Hall, 1966.

[81] R. E. Moore, R. B. Kearfott, and M. J. Cloud, *Introduction to Interval Analysis*. Cambridge University Press, 2009.

[82] F. Korn and Ch. Ullrich, "Verified solution of linear systems based on common software libraries," *Interval Computations*, 3:116–132, 1993.

[83] A. Neumaier, *Interval Methods for Systems of Equations*. Cambridge University Press, 1990.

[84] H. Schwandt, "An interval arithmetic approach for an almost globally convergent method for the solution of the nonlinear Poisson equation," *SIAM Journal on Scientific and Statistical Computing*, 5(2):427–452, 1984.

[85] H. Schwandt, "An interval arithmetic method for the solution of nonlinear systems of equations on a vector computer," *Parallel Computing*, 4(3):323–337, 1987.

[86] E. R. Hansen, *Global Optimization Using Interval Analysis*, Marcel Dekker, Inc., 1992.

[87] H. Ratschek and J. Rokne, *New Computer Methods for Global Optimization*, Wiley, 1988.

[88] C. L. Harkness, *An Approach to Uncertainty in VLSI Design*. PhD thesis, Brown University, May 1991.

[89] C. L. Harkness and D. P. Lopresti, "Interval methods for modeling uncertainty in RC timing analysis", *IEEE Transactions on Computer-Aided Design*, 11(11), Nov. 1992.

[90] J. Stolfi, and L. H. de Figueiredo, "Self-validated reduced numerical methods and applications," *in Brazilian Mathematics Colloquium Monograph. Rio De Janeiro*, Brazil: IMPA, 1997.

[91] J. D. Ma, and R. A. Rutenbar, "Fast interval valued statistical interconnect modeling and reduction", *Proc. ISPD*, pp. 159–166, 2005.

[92] L. H. de Figueiredo, R. Van Iwaarden, and J. Stolfi, "Fast interval branch-and-bound methods for unconstrained global optimization with affine arithmetic," *Technical Report IC-97-08, Institute of Computing, Univ. of Campinas*, Jun. 1997.

[93] F. Messine and A. Mahfoudi, "Use of affine arithmetic in interval optimization algorithms to solve multidimensional scaling problems," *Proceedings of SCAN'98-IMACS/GAMM International Symposium on Scientific Computing, Computer Arithmetic and Validated Numerics*, pp. 22–25, Sep. 1998.

[94] J. L. D. Comba and J. Stolfi, "Affine arithmetic and its applications to computer graphics," *Proc. VI Brazilian Symposium on Computer Graphics and Image Processing*, Oct. 1993.

[95] L. H. de Figueiredo, "Surface intersection using affine arithmetic," *Proceedings of Graphics Interface*, May 1996.

[96] H. H. Shou, R. Martin, I. Voiculescu, and G. Wang, "Affine arithmetic in matrix form for polynomial evaluation and algebraic curve drawing," *Progress in Natural Science*, 12(1):77–81, Jan. 2002.

[97] S. Goldenstein, C. Vogler, and D. Metaxas, "Affine arithmetic based estimation of cue distributions in deformable model tracking," *Proceedings of 2001 Conference on Computer Vision and Pattern Recognition*, Dec. 2001.

[98] A. Lemke, L. Hedrich, and E. Barke, "Analog circuit sizing based on formal methods using affine arithmetic," *Proc. Int. Conf. Computer Aided Design*, pp. 486–489, Nov. 2002.

[99] J. D. Ma, and R. A. Rutenbar, "Fast interval-valued statistical modeling of interconnect and effective capacitance," *IEEE Trans. Computer-Aided Design of Integrated Circuits and Systems*, vol. 25, no. 4, pp. 710–724, Apr. 2006.

[100] J. D. Ma and R. A. Rutenbar, "Interval-valued reduced-order statistical interconnect modeling," *IEEE Trans. Computer-Aided Design of Integrated Circuits and Systems*, vol. 26, no. 9, pp. 1602–1613, Sep. 2007.

[101] A. Vaccardo, C. A. Canizares, and D. Villacci, "An affine arithmetic-based methodology for reliable power flow analysis in the presence of data uncertainty," *IEEE Trans. Power Systems*, vol. 25, no. 2, pp. 624–632, May 2010.

[102] J. Munoz, C. Canizares, K. Bhattacharya, and A. Vaccardo, "Affine arithmetic based methods for voltage and transient stability assessment of power systems with intermittent generation sources," *2013 IREP Symposium*, Rethymnon, Greece, Aug. 25-30, 2013.

[103] A. Piccolo, A. Vaccardo, and D. Villacci, "An affine arithmetic based methodology for the thermal rating assessment of overhead lines in the presence of data uncertainty," *2003 IEEE Bologna PowerTech Conference*, Bologna, Italy, Jun. 23-26, 2003.

[104] Y. Zou, M. Zhang, Y. Cai, Q. Zhou, and X. Hong, "Minimum error based affine arithmetic for variational timing analysis," *in 6th International Conference on ASIC*, Shanghai, China, pp. 978–981, Oct. 24-27, 2005.

[105] H. E. Owny and A. E. Ahmed, "New extension of affine arithmetic: Complex form," *Journal of Communications and Computer Engineering*, vol. 3, no. 1, pp. 11–14, 2013.

[106] D. Poljak, *Advanced Modeling in Computational Electromagnetic Compatibility*. Hoboken, NJ: Wiley, 2007.

[107] L. S. Shieh, J. Gu, and J. W. Sunkel, "Model conversion of uncertain linear systems using the bilinear and inverse-bilinear approximation method," *Proceedings of the 36th Midwest Symposium on Circuits and Systems*, pp. 514–517, Aug. 1993.

[108] L. S. Shieh, J. Gu, and J. S. H. Tsai, "Model conversions of uncertain linear systems via the interval pade approximation method," *Circuits, Systems and Signal Processing*, vol. 15, no. 1, pp. 1–22, 1996.

[109] L. S. Shieh, X. Zou, and J. S. H. Tsai, "Model conversion of continuous-time uncertain systems via the interval geometric-series method," *IEEE. Trans. Circuits and Systems*, vol. 43, no. 10, pp. 851–854, Aug. 2002.

[110] A. Cirillo, N. Femia, and G. Spagnuolo, "An interval mathematics approach to tolerance analysis of switching converters," *27th Annual IEEE Power Electronics Specialists Conference*, Baveno, Italy, pp. 1349–1355, Jun. 23-27, 1996.

[111] C. R. Paul, *Introduction to Electromagnetic Compatibility*. 2nd edition, Hoboken, NJ: Wiley, 2006.

[112] C. R. Paul, *Analysis of Multiconductor Transmission Lines,* Wiley, 1994.

[113] W. Delbare and D. De Zutter, "Space-domain Green's function approach to the capacitance calculation of multiconductor lines in multilayered dielectrics with improved surface charge modeling," *IEEE Transactions on Microwave Theory and Techniques*, vol. 37, no. 10, pp. 1562–1568, Oct. 1989.

[114] C. A. Desoer and E. S. Kuh, *Basic Circuit Theory*. Auckland: McGraw-Hill, 1969.

[115] R. Trinchero, I. S. Stievano, and F. G. Canavero, "Steady-state analysis of switching power converters via augmented time-invariant equivalents," *IEEE Trans. Power Electronics*, vol. 29, no. 11, pp. 5657–5661, Nov. 2014.

[116] R. Trinchero, I. S. Stievano, and F. G. Canavero, "Steady-state response of periodically switched linear circuits via augmented time-invariant nodal analysis," *Journal of Electrical and Computer Engineering*, vol. 2014.